Optical imaging and immunohistological biomarkers to overcome obstacles in nanomedicine drug delivery to tumors and to the brain

Von der Medizinischen Fakultät
der Rheinisch-Westfälischen Technischen Hochschule Aachen
zur Erlangung des akademischen Grades
eines Doktors der Theoretischen Medizin
genehmigte Dissertation

vorgelegt von

Jan-Niklas May, M. SC. RWTH
aus
Recklinghausen

Berichter: Univ.-Prof. Dr. sc. hum. Twan Lammers
PD Dr. rer. nat. Jochen Maurer

Tag der mündlichen Prüfung: 01.12.2025

The one who deserves life and freedom is only the one who has to fight for it daily.

Johann Wolfgang von Goethe

Dedicated to my grandparents.

I. List of publications

Part of this thesis have been published in:

Jan-Niklas May*, Susanne K. Golombek*, Maike Baues, Anshuman Dasgupta, Natascha Drude, Anne Rix, Dirk Rommel, Saskia von Stillfried, Lia Appold, Robert Pola, Michal Pechar, Louis van Bloois, Gert Storm, Alexander Kuehne, Felix Gremse, Benjamin Theek, Fabian Kiessling, Twan Lammers; Multimodal and multiscale optical imaging of nanomedicine delivery across the blood-brain barrier upon sonopermeation; **Theranostics**; 2020; 10(4); 1948-1959; *** shared first authors**

Jan-Niklas May*, Jennifer I. Moss*, Florian Mueller, Susanne K. Golombek, Ilaria Biancacci, Larissa Rizzo, Asmaa Said Elshafei, Felix Gremse, Robert Pola, Michal Pechar, Tomas Etrych, Svea Becker, Christian Trautwein, Roman D. Bülow, Peter Boor, Ruth Knuechel, Saskia von Stillfried, Gert Storm, Sanyogitta Puri, Simon T. Barry, Volkmar Schulz, Fabian Kiessling, Marianne B. Ashford, Twan Lammers; Histopathological biomarkers for predicting the tumour accumulation of nanomedicines; **Nature Biomedical Engineering;** 2024; 8; 1366-1378; *** shared first authors**

Additional publications:

Susanne K. Golombek, **Jan-Niklas May**, Benjamin Theek, Lia Appold, Natascha Drude, Fabian Kiessling, Twan Lammers; Tumor targeting via EPR: Strategies to enhance patient responses; **Advanced Drug Delivery Reviews**; 2018; 130; 17-38

Jasmin Baier, Anne Rix, Natascha Drude, Milita Darguzyte, Maike Baues, **Jan-Niklas May**, Sandra Schipper, Diana Möckel, Rupert Palme, René Tolba, Fabian Kiessling; Influence of MRI Examinations on Animal Welfare and Study Results; **Investigative Radiology**; 2020; 55(8); 507-514

Anne Rix, Marion Piepenbrock, Barbara Flege, Saskia von Stillfried, Patrick Koczera, Tatjana Opacic, Nina Simons, Peter Boor, Sven Thoröe-Boveleth, Roel Deckers, **Jan-Niklas May**, Twan Lammers, Georg Schmitz, Elmar Stickeler, Fabian Kiessling; Effects of

contrast-enhanced ultrasound treatment on neoadjuvant chemotherapy in breast cancer; **Theranostics**; 2021; 11(19); 9557-9570

Ilaria Biancacci, Federica De Lorenzi, Benjamin Theek, Xiangyang Bai, **Jan-Niklas May**, Lorena Consolino, Maike Baues, Diana Moeckel, Felix Gremse, Saskia von Stillfried, Asmaa El Shafei, Karina Benderski, Armin Azadkhah Shalmani, Alec Wang, Jeffrey Momoh, Quim Peña, Eva Miriam Buhl, Johannes Buyel, Wim Hennink, Fabian Kiessling, Josbert Metselaar, Yang Shi, Twan Lammers; Monitoring EPR Effect Dynamics during Nanotaxane Treatment with Theranostic Polymeric Micelles; **Advanced Science**; 2022; 9(10); 2103745

Jasmin Baier, Anne Rix, Milita Darguzyte, Renée Michèle Girbig, **Jan-Niklas May**, Rupert Palme, René Tolba, Fabian Kiessling; Repeated contrast-enhanced micro-CT examinations decrease animal welfare and influence tumor physiology; **Investigative Radiology**; 2022; 58(5); 327-336

Elisa F. Brandt, Maike Baues, Theresa H. Wirtz, **Jan-Niklas May**, Petra Fischer, Anika Beckers, Björn-Carsten Schüre, Hacer Sahin, Christian Trautwein, Twan Lammers, Marie-Luise Berres; Chemokine CXCL10 Modulates the Tumor Microenvironment of Fibrosis-Associated Hepatocellular Carcinoma; **International Journal of Molecular Sciences**; 2022; 23(15); 8112

Svea Becker, Jeffrey Momoh, Ilaria Biancacci, Diana Möckel, Qingbi Wang, **Jan-Niklas May**, Huan Su, Lena Susanne Candels, Marie-Luise Berres, Fabian Kiessling, Maximilian Hatting, Twan Lammers, Christian Trautwein; Intermittent Fasting Primes the Tumor Microenvironment And Improves Nanomedicine Delivery In Hepatocellular Carcinoma; **Small;** 2023; 19(43); 2208042

Sonia Vicente-Ruiz, Ana Arminan, Katia Maso, Elena Gallon, Oleksandr Zagorodko, Julie Movellan, Fernanda Rodriguez-Otormin, Maike Baues, **Jan-Niklas May**, Federica De Lorenzi, Twan Lammers, María Vicent; Poly-L-Glutamic acid modification modulates the bio-nano interface of a therapeutic anti-IGF-1R antibody in prostate cancer; **Biomaterials;** 2023; 301; 122280

Christopher Hark, Junlin Chen, Julia Blöck, Eva Miriam Buhl, Harald Radermacher, Robert Pola, Michal Pechar, Tomáš Etrych, Quim Peña, Anne Rix, Natascha Ingrid Drude, Fabian Kiessling, Twan Lammers[#], **Jan-Niklas May[#]**; RGD-coated polymeric microbubbles promote ultrasound-mediated drug delivery in an inflamed endothelium-pericyte co-culture model of the blood-brain barrier; **Drug Delivery and Translational Research;** 2024; 14; 2629-2641; **[#] corresponding authors**

Rahaf Mihyar, Armin Azadkhah Shalmani, Viktor Wildt, Maryam Sheybanifard, Alec Wang, **Jan-Niklas May**, Saba Shahzad, Eva Miriam Buhl, Stephan Rütten, Diana Behrens, Wolfgang Walther, Mattia Tiboni, Luca Casettari, Johannes F. Buyel, Cristianne J.F. Rijcken, Wim E. Hennink, Saskia von Stillfried, Fabian Kiessling, Yang Shi, Josbert M. Metselaar, Twan Lammers, Quim Peña; Microfluidic formulation, cryoprotection and long-term stability of paclitaxel-loaded π electron-stabilized polymeric micelles; **Journal of Controlled Release;** 2024; 375; 614-626

Anshuman Dasgupta, **Jan-Niklas May**, Geir Klinkenberg, Helena C. Besse, Eva Miriam Buhl, Diana Möckel, Rahaf Mihyar, Quim Peña, Armin Azadkhah Shalmani, Christopher Hark, Anne Rix, Susanne Koletnik, Josbert Metselaar, Yang Shi, Wim E. Hennink, Gert Storm, Dannis van Vuurden, Chrit Moonen, Mario Ries, Ruth Schmid, Fabian Kiessling, Twan Lammers; Multidrug Micelles and Sonopermeation for Chemotherapy Co-Delivery to Brain Tumors; **Journal of Controlled Release;** 2025; 380; 818-828

Natascha Drude, Camila Baselly, Malgorzata Anna Gazda, **Jan-Niklas May**, Lena Tienken, Parya Abbasi, Tracey Weissgerber, Steven Burgess; Reporting quality of quantitative polymerase chain reaction (qPCR) methods in scientific publications; submitted

II. Table of contents

III. List of abbreviations

°C *degrees celsius*

µl *microliter*

µm *micrometer*

A431 *human epidermoid cancer cell line A431*

ALS *amyotrophic lateral sclerosis*

AUC *area under the curve*

BBB blood-brain barrier

BxPC3 *human pancreatic cancer cell line BxPC3*

C26 *murine colon adenocarcinoma 26*

CNS *central nervous system*

Col I *collagen I*

Col IV *collagen IV*

CT *computed tomography, computed tomography*

CT26 *murine colon carcinoma cell line CT26*

CT-FLT *hybrid computed tomography-fluorescence tomography*

DAB *3, 3'-diaminobenzidine*

DMSO *dimethyl sulfoxide*

ECM *extracellular matrix*

EPR *enhanced permeability and retention, enhanced permeability and retention*

FRI *fluorescence reflectance imaging*

h *hours*

H&E *hematoxylin and eosin*

HER2 *human epidermal growth factor receptor 2*

HPMA *N-(2-hydroxypropyl) methacrylamide*

HRP *horseradish peroxidase*

i.v. *intravenous*

IgG *immunoglobulin G*

kDa *kilodalton*

LANUV *Landesamt für Natur-, Umwelt- und Verbraucherschutz*

Ma-GG-TT *3-(N-methacryloyl glycylglycyl)thiazolidine-2-thione*

MHz *megahertz*

min *minutes*

MLS *human ovarian carcinoma cell line MLS*

mm *millimeter*

mM *millimolar*

MMP-9 *matrix metalloproteinase-9*

MPa *megapascal*

MRI *magnetic resonance imaging, magnetic resonance imaging*

nm *nanometer*

PBCA *poly(butyl cyanoacrylate)*

PDI *polydispersity index*

PEG *poly(ethylene glycol)*

pH *potential of hydrogen*

PHPMA *poly(N-(2-hydroxypropyl)) methacrylamide*

PSMA *prostate specific membrane antigen*

RNA *ribonucleic acid*

rpm *rounds per minute*

RT *room temperature*

STED *stimulated emission depletion*

αSMA *alpha-smooth muscle actin*

1 Introduction

1.1 Nano-sized drug delivery systems

Nanomedicines are a diverse group of drug delivery systems mainly defined by their size between 1 to 1000 nm (Doane and Burda, 2012). Their composition is as many-faceted as the encapsulated drugs, ranging from nanomedicines made out of proteins, lipids, polymers, metals, and combinations thereof, to applications in almost all diseases with a major focus on cancer and inflammation (Peer et al., 2007). Thus, the research community working on nanomedicines is highly interdisciplinary, with chemists, material scientists, pharmacists, biologists, and physicians specializing on the synthesis of new formulations, potential therapeutic applications, and the cumbersome translation into the clinic (Anselmo and Mitragotri, 2021). The content of this thesis will focus on well-established nanomedicines, i.e. polymers and liposomes, with a dedicated effort in overcoming common obstacles of the field, mainly the clinical translation in general and the blood-brain barrier in particular, both with the overarching aim to improve (nano)chemotherapy-based antitumor treatment.

The combination of chemotherapeutic drugs and nano-sized drug delivery systems is based on the relatively short blood half-life of traditional chemotherapeutic drugs and the noticeable accumulation in healthy organs (Shi et al., 2017). With a low molecular weight of usually below 1 kDa, most drugs (e.g. doxorubicin, paclitaxel) are cleared within minutes to hours from the blood, minimizing the time period to substantially reach the tumor while still distributing to healthy organs, causing dose-limiting side effects (Figure 1) (Arcamone et al., 1969, Wall and Wani, 1995, Golombek et al., 2018). Loading these drugs into or attaching them to drug delivery systems results in larger constructs with a size above the renal threshold of ±40 kDa, extending blood half-life from hours to days (Gabizon et al., 1994, Hamilton et al., 2002, Girish et al., 2012, Doi et al., 2017). Furthermore, the biodistribution is altered compared to drug molecules as healthy blood vessels usually do not allow the extravasation of compounds with a size of 10-1000 nm, avoiding the accumulation of toxic drugs in healthy organs (O'Brien et al., 2004, Golombek et al., 2018). Blood vessel walls in tumors tend to be leakier, allowing the passage of drug delivery systems and enabling their penetration into the tumor (Dvorak et al., 1988, Hashizume et al., 2000).

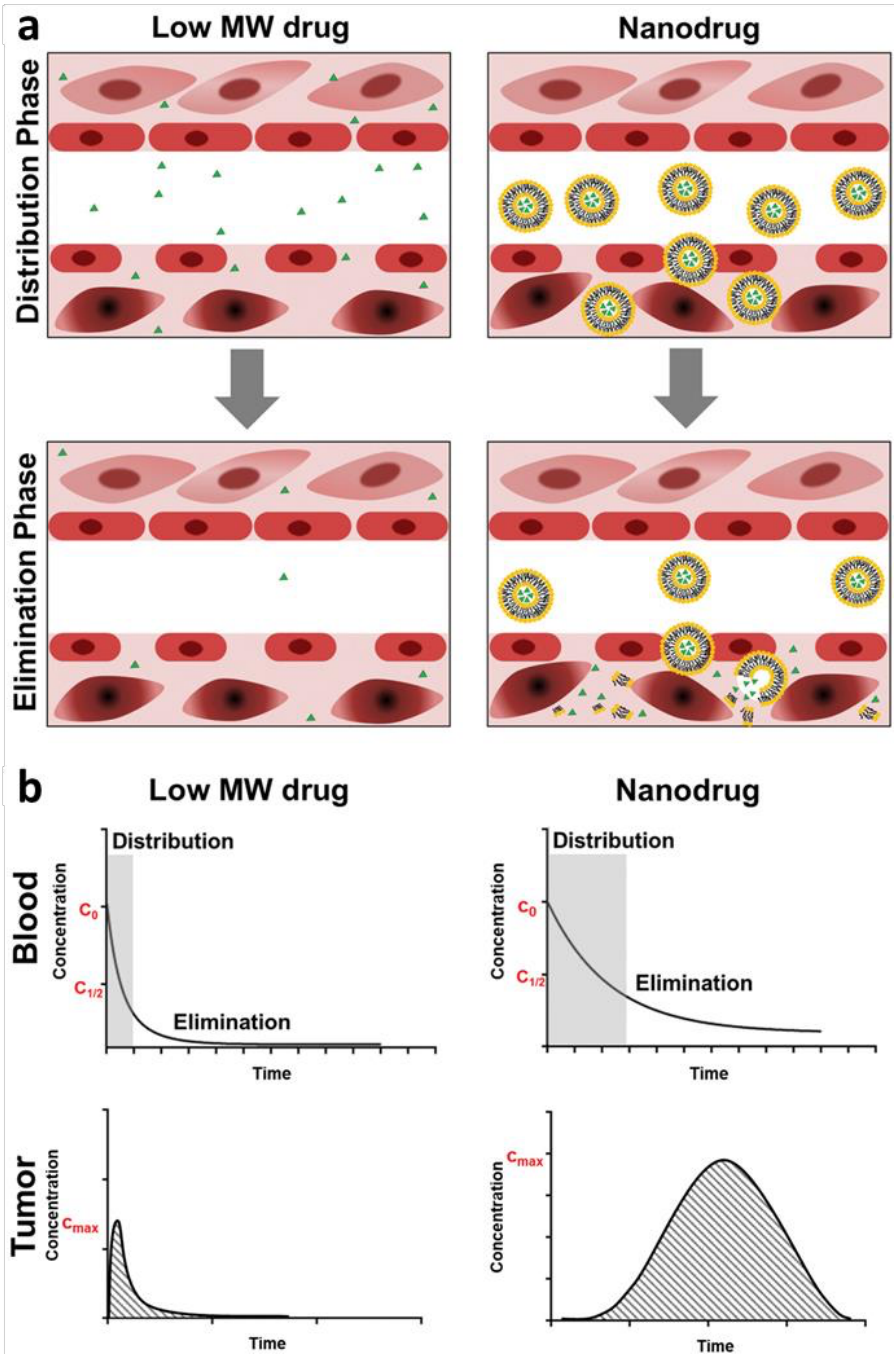

Figure 1: Comparison of the distribution and elimination of low molecular weight drugs and nanomedicines. Low molecular drugs (chemotherapies) distribute in the tumor as well as in healthy tissues, while nanomedicines mainly accumulate in the tumor. Furthermore, drug molecules are cleared way faster from the bloodstream **(a)**. Compared to low molecular weight drugs, nanomedicines present with extended circulation properties, leading to lengthened accumulation in the tumor and a higher total accumulation **(b)**. Adapted from Golombek et al. (Golombek et al., 2018).

However, the larger size of nanomedicines presents them more prominently to the immune system, potentially leading to the activation of the complement system or the binding of IgG antibodies, resulting in a process named opsonization and an uptake of nanomedicines by the reticuloendothelial system, mainly by monocytes and

macrophages of lymph nodes, the spleen and the liver. To escape opsonization, strategies to stealth nanoparticles are heavily investigated, leading e.g. to the modification of the surface of nanoparticles with poly(ethylene glycol) (PEG) (Owens III and Peppas, 2006). This contributes to the common notion, that on the one hand, the body has to be protected from the drug (e.g. by encapsulation to avoid the accumulation in healthy organs and reduce side effects), while on the other hand, also the drug (delivery system) has to be protected from the body (e.g. to avoid the rapid degradation of RNA before reaching the therapeutic site or reducing the accumulation in liver and spleen) - which can both be tackled by using nanomedicines.

1.2 Tumor accumulation and retention of nanomedicines

The tumor targeting of nanomedicines was detected by Yasuhiro Matsumura and Hiroshi Maeda in 1986 who reported an improved accumulation of the chemotherapeutic drug neocarzinostatin in tumors upon conjugation to a polymer (Matsumura and Maeda, 1986). Following Ehrlich's famous concept of the "magic bullet", a selective tumor-targeted drug delivery concept was thought to be identified that can discriminate between healthy and tumorous tissues (Ehrlich, 1907, Williams, 2009, Nichols and Bae, 2014). Considered to be based on more and leakier blood vessels within a tumor and the lack of lymphatic clearance, this phenomenon was named the Enhanced Permeability and Retention (EPR) effect (Maeda et al., 2000). Due to the diffusion limit of oxygen and nutrients, growing tumors induce the formation of new blood vessels to meet their metabolic needs (Folkman, 1971, Carmeliet and Jain, 2000). "Sustained angiogenesis" is therefore also defined as one of the first six hallmarks of cancer (Hanahan and Weinberg, 2000), and its inhibition was a valid therapeutic target in attempts to starve tumors (Hurwitz et al., 2004). With respect to drug delivery, functional vessels are essential in enabling the effective transport of drugs and drug delivery systems of almost all administration routes to a tumor. The concept of "vessel normalization" underlines the need for functional (=perfused) vessels as the aim of this co-treatment is a shift from a highly immaturely vascularized tumor microenvironment towards a more mature, better perfused vasculature with an improved penetration of drugs into the tumor (Tong et al., 2004, Jain, 2005). Due to the extended blood half-life

of nanomedicines, multiple passages of an individual nanoparticle through a tumor are possible, enhancing the chance of its extravasation out of the blood vessel into the tumor tissue and leading to an increase in tumor accumulation hours and days post injection (Miedema et al., 2022).

Once extravasated out of the blood vessel, most nanomedicines are taken up by phagocytes, mainly tumor-associated macrophages, which have been found to release the encapsulated drug enabling the diffusion of drug molecules through the tumor and the uptake by tumor cells (Miller et al., 2015b, Cuccarese et al., 2017, Lin et al., 2022). Neutrophils and tumor cells are also known for the uptake of nanomedicines, such as Doxil®, and are therefore also most heavily affected by the drug and eventually killed (Ngai et al., 2023). Enhancing the retention of nanomedicines is needed to prolong the time they stay inside the tumor and are able to release their payload before being cleared via the lymphatic system (or glymphatic system, for the CNS specifically) (Gu et al., 2020, Nguyen et al., 2023, Tang et al., 2024). A non-functional lymphatic system on the other hand contributes also to a high interstitial fluid pressure, which inhibits the extravasation of drug delivery systems and the perfusion of tumors due to collapsing vessels, indicating a bifaceted role of the lymphatic drainage (Boucher et al., 1990, Griffon-Etienne et al., 1999, Padera et al., 2004). Comparably, also components of the extracellular matrix (ECM) can support and stabilize blood vessels (e.g. collagen IV (Col IV) or alpha-smooth muscle actin (αSMA)) or hinder the penetration and distribution of nanomedicines through the tumor (e.g. collagen I (Col I) or stromal αSMA) (Yokoi et al., 2014a). Tumor penetration was found to depend both on the size of the nanocarrier, but also on the vasculature and its permeability with small micelles distributing more homogeneous than large micelles in a low perfused and permeable tumor (BxPC3) model while no difference for the same micelles was detectable in a well perfused and highly permeable tumor model (C26) (Cabral et al., 2011).

In addition to traditional nanomedicines such as Doxil®, numerous targeting approaches have been developed functionalizing a nanoparticle with e.g. antibodies, nanobodies or peptides to target specific receptors or proteins of cells or the ECM - with the most prominent and profitable examples from the field of antibodies and antibody-drug conjugates (Byrne et al., 2008, Drago et al., 2021). Blocking a receptor due to the

targeting can already have a therapeutic effect, which is e.g. known for HER2 (human epidermal growth factor receptor 2) (Slamon et al., 2011), which can be further extended by adding drugs to the antibody (Lewis Phillips et al., 2008). The most well-known examples of targeted nanomedicines are BIND-014 (Hrkach et al., 2012, Von Hoff et al., 2016), which was a docetaxel-loaded polymeric nanoparticle targeted to PSMA (prostate specific membrane antigen), and MM-302, which was a doxorubicin-loaded liposome targeted to HER2 (Miller et al., 2016, Espelin et al., 2016). The usage of the past tense indicates that both products did not make it into clinical practice due to missing endpoints in phase II clinical trials. Furthermore, and against common claims of enhancing the tumor accumulation by active targeting, it should be noted that targeting typically improves the retention inside a tumor, but not the overall accumulation (Wilhelm et al., 2016b, Tsvetkova et al., 2017).

Accumulation in general was considered a passive process, based on diffusion and leaky blood vessels, as introduced above (Dvorak et al., 1988, Hashizume et al., 2000). Matsumoto et al. imaged the extravasation of polymeric nanoparticles of varied sizes and were able to detect eruptions of nanoparticles, leaving the vessels in a spotted, heterogeneous, and dynamic matter (Matsumoto et al., 2016), and not in a rather homogenous way over larger parts of vessels that are leaky (Hashizume et al., 2000). Bursts of nanoparticles, which were found to be induced by macrophages, have already been described by Miller et al. upon radiotherapy (Miller et al., 2017), which was already known to enhance tumor accumulation of nanomedicines (Lammers et al., 2007). Recently, the group of Warren Chan has challenged the principle of the EPR effect and its passive targeting as the main contributing factor to the accumulation of nanomedicines in tumors (Sindhwani et al., 2020). Extending the findings of rarer than estimated gaps in blood vessels, they could also show the accumulation of gold as well as fluorescently-labeled nanoparticles in live animals but not in dead and still perfused "zombie" animals, claiming that this difference points toward the contribution of active transport mechanisms through endothelial cells while using kidney and liver as controls for passive accumulation (Figure 2) (Sindhwani et al., 2020).

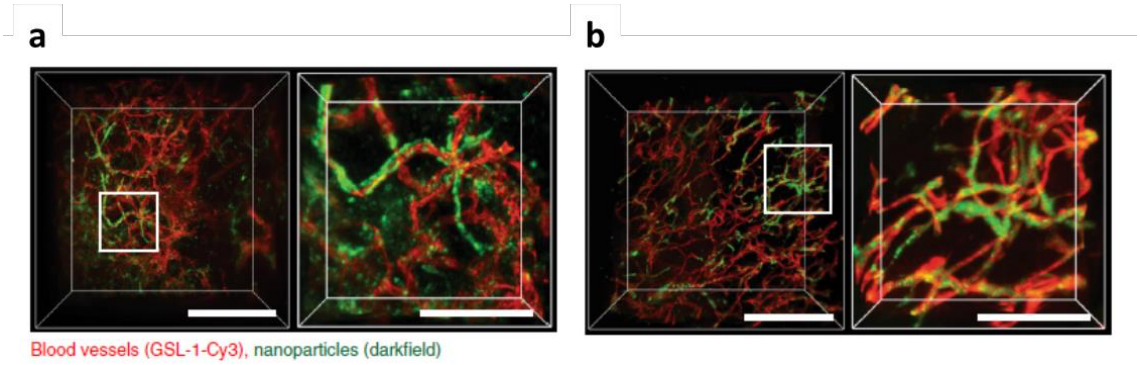

Figure 2: Three-dimensional microscopy of fluorescently-labeled nanoparticles in zombie and control animals pointing towards an active transport mechanism. Nanoparticles (in green) were barely found to extravasate in zombie animals **(a)** in contrast to control animals, most likely due to active transport pathways **(b).** Scale bars depict 500 µm, and 200 µm for zoom-ins. Adapted from Sindhwani et al. (Sindhwani et al., 2020).

In a follow-up study, a subset of endothelial cells named nanoparticle transport endothelial cells was found to be the main extravasation-contributing cell population, with an upregulated expression of genes linked to vessel permeability or transcytosis (Kingston et al., 2021). Taken together, these findings pinpoint the need for further (pre)clinical research, which will be ethically challenging to get approved for patients as studies comparable to the ones in the field of organ transplantation, where braindead patients receive e.g. a xenotransplanted porcine kidney (Porrett et al., 2022), can be conducted in tumor patients more often than once in 20 years (Arap et al., 2002, Pentz et al., 2003) to improve the understanding of nanomedicine interactions with the body, blood vessels, and tumors.

1.3 Clinical translation of nanomedicines

Tumor-targeted nanomedicines are the topic of thousands of publications each year (see e.g. common scientific databases or libraries such as pubmed). However, the list of successfully translated drug products into the clinic is comparably short indicating a discrepancy between fruitful preclinical research and clinical reality (Venditto and Szoka Jr, 2013). The lack of clinical translation is on the one hand based on the potentially challenging reproducible production, its upscaling, the purification of the nanomedicine as well as long-term storage and shipment conditions and on the other hand based on clinical trials not meeting the efficacy endpoints (He et al., 2019, Mihyar et al., 2024).

Wilhelm et al. postulated in a heavily discussed meta-analysis, that only 0.7% of injected nanomedicines reach the tumor (Wilhelm et al., 2016b, McNeil, 2016, Wilhelm et al., 2016a). While McNeil questions in a response, if tumor accumulation is the correct parameter to evaluate the efficacy of nanomedicines, he suggests to assess the maximum drug concentration in a tumor or the blood half-life, also reminding that the tumor accumulation of traditional chemotherapeutic drugs is not higher than the calculated 0.7% ID/kg for nanomedicines (McNeil, 2016). Price et al. (Price et al., 2020) point towards using classical pharmacokinetic measures such as the ratio of the AUCs of blood and tumor. In the case of doxorubicin and Doxil®, it is indeed reported that drug accumulation in a tumor is higher for the nanomedicine formulation than for the traditionally administered drug molecule (Gabizon et al., 1997, Safra et al., 2000). Wilhelm et al. on the other hand mention in their response to McNeil's reply to their meta-analysis that one has to decide if the drug molecule accumulation or the drug delivery system accumulation should be analyzed as it makes quite a difference, if e.g. the blood concentration is evaluated without differentiating between the free, released drug molecule and the still encapsulated drug molecule, which holds also true for the blood and tumor AUCs (Wilhelm et al., 2016a). With the lack of a uniform, standardized reporting of preclinical nanomedicine studies, it is very challenging to draw comprehensive conclusions, as mostly only the tumor accumulation of nanomedicines is reported, lacking detailed pharmacokinetic values (Wilhelm et al., 2016a).

Other scientists question the EPR effect and its occurrence in human tumors, also criticizing rodent tumor models (Danhier, 2016, Golombek et al., 2018). While there is a valid point in the need for more accurate animal models to improve preclinical research, the tumor accumulation of nanomedicines is very well proven for several types of nanoparticles in vastly different solid human primary tumors as well as metastases (Harrington et al., 2001, Miedema et al., 2022), showing that a lack of tumor accumulation is not the primary obstacle inhibiting a successful translation. As introduced above, nanomedicines are not only massively taken up by phagocytic cells inside the tumor microenvironment, but they also prominently and rapidly accumulate in liver and spleen. Strategies to avoid the accumulation in the reticuloendothelial system are studied, however, a straightforward and easily applicable solution could yet not be identified. Tackling the problem from a different angle, the group of Warren Chan

considered the liver as a definite organ, which should not have indefinite nanoparticle uptake capabilities, and found a threshold based on the number of injected nanoparticles, that saturates the uptake by the liver (Ouyang et al., 2020). Interestingly, when they adapted their threshold from mice to humans, it was found that all clinically successful nanomedicines are above the calculated threshold (1 trillion for mice, 1.5 quadrillion for humans), while the "failed" ones are usually below (Ouyang et al., 2020).

Just injecting higher numbers of nanoparticles is not the final solution in improving clinical translation but rather a key prerequisite that should be considered in designing nanomedicines - e.g. it might be smarter to reduce the drug loading per individual nanoparticle or add unloaded nanoparticles to overcome the liver uptake and improve tumor accumulation. As seen in micelles or liposomes, that are above the 1.5 quadrillion threshold established by Ouyang et al., tumor accumulation varies between patients and even between different tumors and metastases in individual patients (Harrington et al., 2001, Miedema et al., 2022), exemplifying the need for additional patient stratification methods to enable personalized nanochemotherapies. Assessing the tumor accumulation in mice and patients via the direct imaging of the (radio-)labeled nanomedicine formulation or via indirect imaging using companion diagnostics enables preclinical research using non-invasive and longitudinal imaging, that is well tolerated and supports the implementation of the 3R principles (Baier et al., 2020, Baier et al., 2023). Furthermore, imaging can guide therapy decisions, as a good correlation between tumor accumulation and therapeutic response could be observed on a preclinical and a clinical level (Golombek et al., 2018) and also assess changes in tumor accumulation over the course of the therapy (Biancacci et al., 2022). For example, using ferumoxytol as a companion diagnostic, the tumor accumulation of a PLGA-PEG therapeutic nanoparticle loaded with docetaxel was predicted in several tumor models (HT1080, A2780CP, 4T1, and KP1.9) as both compounds were found to have very comparable distribution profiles using confocal multiphoton microscopy, and also MRI (Miller et al., 2015a). Supported by Merrimack Pharmaceuticals, a comparable study was performed in breast, cervical, head & neck, ovarian, pancreatic, and mixed (solid) tumor patients who were treated with liposomes containing irinotecan (Figure 3 e, f) (Ramanathan et al., 2017). In both studies, high levels of ferumoxytol indicated not only high nanoparticle accumulation but also an increased therapy response, mainly an enhanced tumor shrinkage (Miller et

al., 2015a, Ramanathan et al., 2017). Also using an indirect imaging approach, Pérez-Medina et al. co-injected ^{89}Zr-labeled liposomes and Doxil®, but also Cy7-PLGA, DiR-NE, and Cy5.5-albumin@Abraxane, in 4T1-tumor bearing mice (Pérez-Medina et al., 2016). Especially for PEGylated, long-circulating nanomedicines, the ^{89}Zr-labeled liposomes were useful for discriminating between lower and higher nanomedicine accumulating tumors and were also able to predict tumor growth and survival (Figure 3 a, b) (Pérez-Medina et al., 2016). Evaluating the impact of untargeted, ^{64}Cu-labebeld liposomes for the prediction of the tumor accumulation of several liposomal formulations (doxorubicin-loaded liposomes, irinotecan-loaded liposomes and HER2-targeted and doxorubicin-loaded liposomes), Lee et al. discovered a good correlation between the PET-captured tumor accumulation of radiolabeled liposomes and all liposomal drug formulations (Lee et al., 2018). Tumors, that presented with a strong accumulation of radiolabeled liposomes, responded better to targeted as well as untargeted liposomal formulations while this correlation could not be found in doxorubicin treated animals (Figure 3 c, d). Studying the accumulation of Her2-targeted, ^{64}Cu-labeled, PEGylated, doxorubicin-containing liposomes in metastatic breast cancer patients, Lee et al. were able to show a link between higher tumor uptake and an improved therapeutic response (Figure 3 g, h) (Lee et al., 2017). Although the patient number (n=19) is not too large, the best overall response was in 43% of patients with low accumulating tumors a stable disease, while 75% of the patients with high accumulating tumors had either a partial response or stable disease (Lee et al., 2017). Unfortunately, the two patients with the shortest progression-free survival were both patients with high accumulating tumors, with one of them even showing the highest accumulation of the theranostic liposome at all - consequently indicating that a decent tumor accumulation of a nanomedicine is required but not a guarantee to induce a therapeutic response (Lee et al., 2017). In contrast, a single not responding metastatic site might result in an unavoidable death of a patient with otherwise well-responding primary and secondary tumors (Dillekås et al., 2019, Boire et al., 2024). Imaging can enable the detection of the distribution of nanomedicines on a whole-body level, showing the inter- and intra-patient heterogeneity in the accumulation of e.g. radio-labeled micelles in the primary tumor but also in “cold” and “hot” metastases (Miedema et al., 2022).

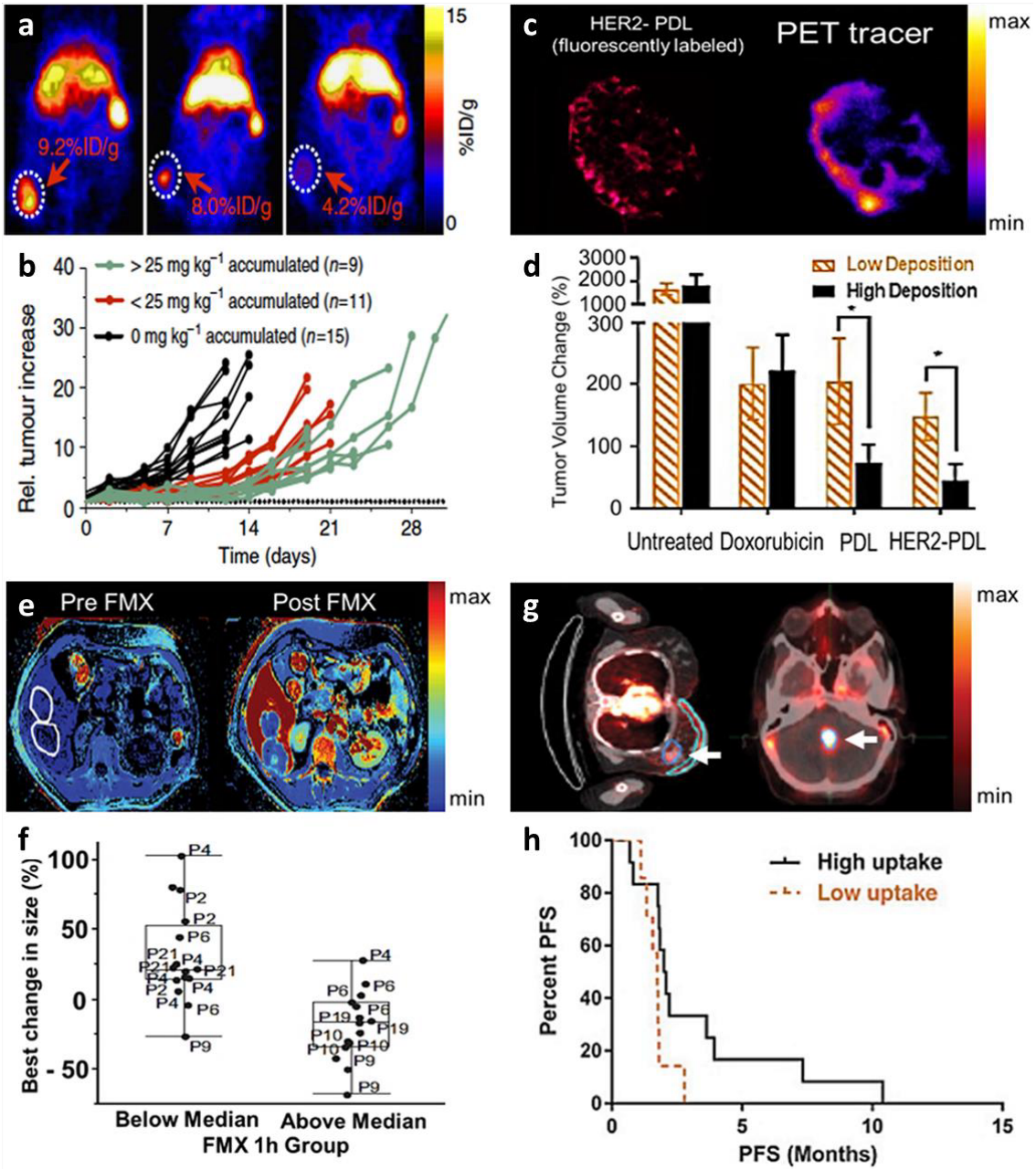

Figure 3: Direct and indirect imaging of nanomedicines and a companion diagnostic to predict tumor accumulation and therapeutic response. The tumor accumulation of a ^{89}Zr-labeled liposome was assessed in 4T1-tumor-bearing mice using PET imaging, displaying the variability between individual mice **(a)**. Based on the tumor accumulation ranging from zero to low to high, there was a noticeable delay in the relative tumor growth detectable **(b)**. Adapted from Pérez-Medina et al. (Pérez-Medina et al., 2016). PEGylated and HER2-targeted liposomes were labeled both with a fluorophore and ^{64}Cu and injected in BT474-M3 tumor-bearing mice to multimodally image the tumor accumulation using fluorescence microscopy and PET **(c)**. A high tumor accumulation of liposomes correlated with the strongest tumor response based on the change in tumor volume **(d)**. Adapted from Lee et al. (Lee et al., 2018). Ferumoxytol was used as a companion diagnostic to predict the therapeutic response to irinotecan-loaded liposomes **(e)**. Dividing tumors in below and above the median of the accumulation of ferumoxytol was found to be connected to the therapeutic response indicated by the change in tumor growth **(f)**. Adapted from Ramanathan et al. (Ramanathan et al., 2017). PEGylated and HER2-targeted liposomes, which were labeled with ^{64}Cu and loaded with doxorubicin, were used to image the tumor accumulation in breast (left) and brain (right) tumors **(g)**. Patients, whose tumors showed higher tumor accumulation experienced also a longer progression-free survival **(h)**. Adapted from Lee et al. (Lee et al., 2017).Whole figure adapted from Golombek et al. (Golombek et al., 2018).

Miedema et al., who imaged polymeric, docetaxel-loaded, and ^{89}Zr-labeled micelles, discriminated between accumulating tumor sites and non-accumulating ones using PET imaging. They detected an expected high variability between accumulating primary tumors and metastases, even in the metastases of the same patient - and interestingly also reported a decrease in size of metastases which did not present accumulated micelles on PET-CT scans.

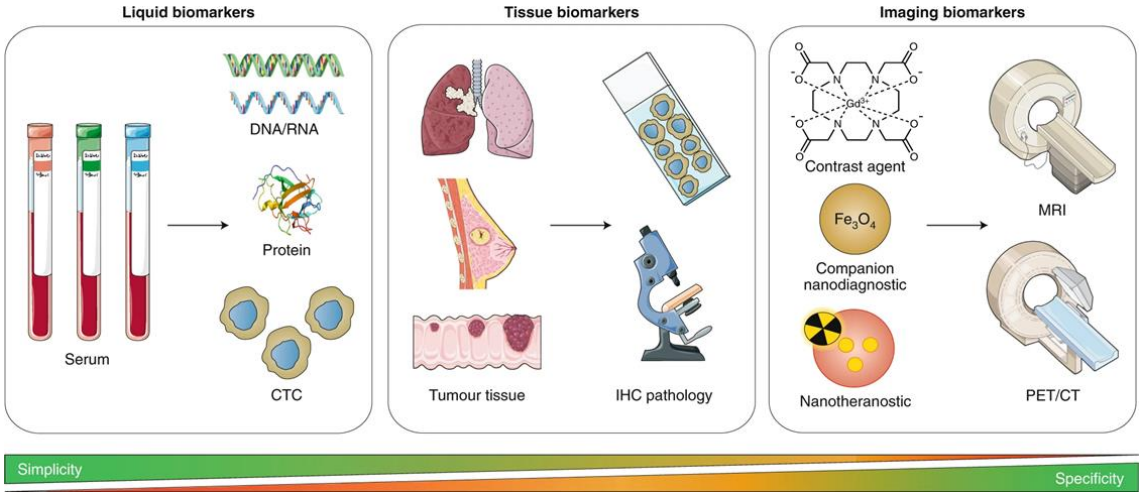

Figure 4: Biomarker classes to stratify patients in cancer trials. Biomarkers can be for example liquid biomarkers, tissue biomarkers or imaging biomarkers with different levels of simplicity and specificity. Adapted from van der Meel et al. (van der Meel et al., 2019).

These imaging approaches are highly specific and very accurate, but they require the accessibility of radiochemistry labs and nuclear medicine imaging devices, can come with additional hurdles (e.g. does every single particle contain the chelating agent to enable labeling or does one add an extra, radiolabeled formulation), and they massively increase the workload and costs per patient (Figure 4) (van der Meel et al., 2019). As briefly mentioned above, just the tumor accumulation of a nanomedicine detected by nuclear imaging does not guarantee the success of the therapy. On the other hand, and as almost every cancer diagnosis is based on the evaluation of a biopsy by a pathologist, histopathological biomarkers are very straightforward to implement in clinical routine. Within the antibody field, the nowadays billion-dollar drug Herceptin® was only approved upon stratifying patients based on their HER2 status using HER2 stainings (Jacobs et al., 1999). Ignoring the above discussed passive or active transport of nanomedicines into tumors, it is deemed logical, that the buildup of a tumor's microenvironment will have an impact on the delivery of nanomedicines. Previous, rather small preclinical studies revealed that e.g. blood vessels correlate with tumor

accumulation (Sulheim et al., 2018), collagen next to capillary walls indicates the permeability and extravasation of nanomedicines (Yokoi et al., 2014a), or blood vessels and even MMP-9 as a serum biomarker (Yokoi et al., 2014b) were correlated with the accumulation of nanomedicines. However, none of these biopsy-based approaches was further tested on additional preclinical tumor models or on human tumor samples or even translated into the clinic, and the highly specific imaging tools are barely used in clinical trials or in personalized therapy decisions.

1.4 Co-treatments to enhance the tumor accumulation of nanomedicines

Based on the previously discussed heterogeneity of the tumor accumulation of nanomedicines, several pharmacological, behavioral, and physical co-treatments have been tested to improve the delivery of nano-sized drug carriers but also of traditional chemotherapeutic drug molecules (Golombek et al., 2018, Becker et al., 2023). Here, I will only focus on the combination of ultrasound and microbubbles which is also named sonopermeation (Snipstad et al., 2018, Snipstad et al., 2021). Microbubbles are an ultrasound contrast agent and are made out of a shell (polymers, lipids, or proteins) with a gas-filled core (Ferrara et al., 2007, Kiessling et al., 2012). Due to their size of 1-5 µm, they do not extravasate out of blood vessels and can therefore be used to image tissue perfusion and investigate pathological processes such as inflammation or cancer due to an altered vasculature (Kiessling et al., 2012). Depending on the power of the applied ultrasound (frequency, pressure), microbubbles can not only be used as contrast agents but upon inducing oscillation or bursts, also for therapeutic interventions, based on the created mechanical forces (Kooiman et al., 2014, Roovers et al., 2019, Deprez et al., 2021). The result can be the blocking of blood vessels, allowing the diffusion of entrapped drug molecules or an increase in perfusion by widening vessels and pressuring the tumor stroma as well as an enhanced permeability of the blood vessel wall (Kiessling et al., 2012, Rix et al., 2021). The latter can be either due to a disruption of tight junction proteins, an induced enhanced transcytosis, or a combination of both. Using the in the meantime sonopermeation named process, Dimcevski et al. could enhance the delivery of gemcitabine into pancreatic tumors, enabling resections in two so far inoperable tumor patients, and enhancing patient survival compared to a

historical control group (Dimcevski et al., 2016). However, a similar study by Rix et al. in breast cancer patients did not result in an improved therapeutic response (Rix et al., 2021), reflecting the preclinical landscape quite well and pointing to a very sophisticated balance of tumor entity, tissue characteristics, applied ultrasound parameters, used microbubble type, and the injected drug, that has to be timely adjusted to enhance the anticancer effect.

Table 1: Opening the BBB using ultrasound and microbubbles – an overview of tunable parameters. Adapted from Aryal et al. (Aryal et al., 2014).

Parameter	Effect on BBB disruption
Pressure amplitude	Increase in BBB disruption magnitude as pressure amplitude increases; saturation at some point [82], [83], [84]; vascular damage produced at high pressure amplitudes.
Ultrasound frequency	Decrease in BBB disruption threshold as frequency decreases; some evidence of improved safety for lower frequencies [85].
Burst length	For burst lengths less than 10ms, BBB disruption threshold increases and BBB disruption magnitude decreases as burst length is reduced [86], [90], [91], [92]; little or no increase in disruption magnitude for longer bursts [77], [81], [90].
Pulse repetition frequency	BBB disruption magnitude increases as repetition frequency increases up to a point [90]. Other works have observed no effect on BBB disruption magnitude [86].
Ultrasound contrast agent dose	Magnitude of BBB disruption increases with dose [83], [90], [94], [188]; other experiments have reported no effect [86].
Sonication duration	Longer durations [84] or repeated sonication [96], [97] increase magnitude of BBB disruption; damage reported with excessive sonication [84], [97].
Microbubble diameter	Threshold for BBB disruption lower for larger microbubbles; disruption magnitude increased with larger microbubbles [87], [88], [89].
Ultrasound contrast agent	Similar outcomes reported for Optison® and Definity® microbubbles [189]. Sonovue® microbubbles and research agents are also commonly used.

In contrast to the application in solid tumors, (focused) ultrasound in combination with microbubbles to open the BBB is quite well understood on a preclinical level, with many identified adaptable parameters (Table 1) (Aryal et al., 2014, Hynynen et al., 2001, Sheikov et al., 2004, Vykhodtseva et al., 1995). Over the last years, proof-of-concept phase I clinical trials have been conducted in several CNS diseases such as tremor,

neurodegenerative disorders (Alzheimer, Parkinson, ALS), and brain tumors (Abrahao et al., 2019, Gasca-Salas et al., 2021, Lipsman et al., 2018, Mainprize et al., 2019, Rezai et al., 2022). As the vast majority of drug molecules can not overcome an intact BBB, interventions to enable the delivery are heavily investigated (Pardridge, 2007, Pardridge, 2012). In the brain, the ultrasound is either applied intracranially using implanted transducers (Carpentier et al., 2016) or extracranially using helmet-like devices including a thousand of transducers (Mainprize et al., 2019). Guided by MRI, the focus of the transducers is targeted to the pathological sites, with the option of an adjustment between different sessions for extracranially devices (Mainprize et al., 2019). By doing so, a precise spatial control of the treated tissue can be guaranteed, which limits potential side effects, and is extended by feed-back loop systems, controlling the power of the ultrasound, to ensure a stable cavitation of the microbubbles and avoiding a too weak or too powerful treatment (Hynynen et al., 2001). As already mentioned above, especially researchers in Toronto lead by Hynynen, the late Mainprize, and Lipsman showed a well-tolerated opening of the BBB in glioblastoma, ALS, Alzheimer, and Parkinson patients, with a slight increase in delivered drugs to tumor tissue (Mainprize et al., 2019) as well as reduced tau levels in Alzheimer patients (Lipsman et al., 2018). On-going trials investigate an effect on the therapeutic response (e.g. NCT04440358, NCT01620359, NCT04417088, NCT05630209, NCT05615623, NCT05317858, NCT05879120, NCT05902169, NCT04528680), which still has to be proven. In the future, it will be interesting to see if more advanced therapeutic approaches e.g. based on inflammation-targeted microbubbles, which worked well in vitro (Hark et al., 2024), can enable an even more specific treatment of neurodegenerative diseases or brain tumors.

In the here presented work, the combination of ultrasound and microbubbles created a window for the delivery of nanomedicines, to potentially increase the accumulation, retention, and release of drug molecules upon overcoming the BBB. By using multiscale optical imaging, the extravasation of differently sized nanomedicines (PHPMA, 10-20 nm, and liposomes, 120 nm) in healthy brains of mice was imaged to investigate the ideal drug carrier for therapeutic follow-up studies.

2 Objectives

Since the identification of the EPR effect in 1986, nanomedicines have been developed to deliver chemotherapeutic drugs to tumors, potentially leading to improved tumor accumulation profiles and reduced side effects. Only nine years later, the first formulation was approved for clinical use - the doxorubicin-loaded PEGylated liposome Doxil®. In clinical applications, however, nanomedicines do not always reach their full potential.

One of the main reasons for the suboptimal clinical translation of nanomedicines is a lack of patient stratification, leading to the inclusion of cancer patients which tumors that are unlikely to accumulate nanomedicines in sufficient amounts and to eventually respond to the therapy. In chapter 4.1 of this thesis, histopathological biomarkers were screened with the aim of predicting the tumor accumulation of nanomedicines using a supportive machine learning algorithm. The identified biomarkers had to be validated in preclinical tumor models as well as on clinical samples to broadly verify their potential in discriminating between lower and higher accumulating tumors, highlighting the potential of histopathological stainings to predict the tumor accumulation of nanomedicines.

Drug delivery to and into the brain is highly challenging due to the blood-brain barrier, for drug molecules as well as for drug delivery systems. In chapter 4.2, it is investigated if there is a size-dependent effect on the extravasation of fluorophore-labeled nanomedicines upon opening the blood-brain barrier using the combination of ultrasound and microbubbles. Polymers (10 nm) and liposomes (100 nm) were monitored in vivo via hybrid computed and fluorescent tomography and imaged ex vivo via fluorescence reflectance imaging, fluorescent and confocal microscopy and stimulated emission depletion nanoscopy to evaluate if the smaller-sized polymers accumulated more and penetrated deeper into the brain upon sonopermeation than the larger-sized liposomes.

Taken together, within this thesis, two main obstacles for clinical translation of nanomedicines are assessed: patient stratification via histopathological biomarkers and ultrasound-supported drug delivery into the brain.

3 Materials and methods

3.1 Synthesis of microbubbles, polymers, and liposomes

3.1.1 Microbubbles

Microbubbles were synthesized as described previously (Fokong et al., 2011). In short, poly(butyl cyanoacrylate) (PBCA) was the basis of hard-shelled microbubbles. The n-butyl cyanoacrylate monomer was added dropwise to an aqueous solution containing 1% (w/v) tritonX-100 at pH 2.5 during constant mixing using an ultra-turrax. The stirring was extended for 60 min at 10,000 rpm. Upon washing and purification, PBCA microbubbles with a size of 1.5-3 µm were obtained.

3.1.2 Polymeric nanocarriers

Polymers (poly(*N*-(2-hydroxypropyl)) methacrylamide (PHPMA)) were synthesized as described previously (Rihova et al., 2000, Etrych et al., 2007, Theek et al., 2018). The copolymer precursor poly(HPMA-co-Ma-GG-TT) was synthesized via radical copolymerization of *N*-(2-hydroxypropyl) methacrylamide (HPMA) and 3-(*N*-methacryloyl glycylglycyl)thiazolidine-2-thione (Ma-GG-TT) in a 81:15 mol % ratio in DMSO at 50°C for 6 h. To enable optical imaging, the fluorophores Atto 488-NH_2 and Dy750-NH_2 were added to the polymer precursor solution (10 %w/w) in *N,N*-dimethylacetamide and *N,N'*-diisopropylethylamine was added in an equimolar amount related to the fluorophores. The remaining reactive TT groups were aminolyzed with 1-aminopropan-2-ol and precipitated with diethylether after 30 min. PD-10 desalting columns containing Sephadex G-25 resins in water were used to purify the crude product via gel filtration. Using UV/Vis spectrophotometry, the dye contents per polymer were measured (2.1 %w/w for Atto488 and 1.6 %w/w for Dy750). Size-exclusion chromatography revealed a hydrodynamic radius of 4.1 nm and a polydispersity index of 1.7 for the PHPMA polymer using a size-exclusion chromatography equipped with a refractive index and multi-angle light scattering detectors (Wyatt Technology). The molecular weight was determined to be 67 kDa. Fluorescence spectroscopy revealed a size of 10-20 of coiled-coil PHPMA polymers (Theek et al., 2018).

3.1.3 Liposomes

Liposomes were synthesized as described previously (Ergen et al., 2017, Ergen et al., 2019). PEG-PE micelles are based on PEG(2000)-DSPE-NH_2 and PEG(2000)-DSPE and were covalently labeled with NHS esters of Alexa-488 and Alexa-750. The resulting double-labeled PEG-PE micelles were added via a post-insertion method to pre-prepared liposomes. Upon mixing liposomes with double-labeled micelles, the solution was heated up to 60°C for 5 min and kept at room temperature for 10 min which was repeated three times. Fluorophore-labeled liposomes were obtained upon lipid film hydration and extrusion with a diameter of 100 nm and a PDI below 0.1 (analyzed via dynamic light scattering on an ALV CGS-3 (Malvern Instruments)). The zeta potential was measured via a Zetasizer Nano Z (Malvern Instruments).

Doxorubicin was loaded into 100 nm (95-120 nm) HSPC/CHOL/mPEG2000-DSPE (50:45:5 mol%) liposomes containing a 250 mM ammonium sulfate gradient, purchased from FormuMax. Over 1 h incubation, doxorubicin was encapsulated into the liposomes making use of the ammonium sulfate gradient, while unloaded drugs were removed via a Sephadex G-50 column. Eventually, a doxorubicin concentration of ~1.3 mg/mL was achieved, which was measured using the absorbance of doxorubicin at 480 nm. Prior the injection, doxorubicin-loaded liposomes were diluted in saline. This set of experiments was performed at AstraZeneca, mainly by Jennifer I. Moss. Further details are described in (May et al., 2024).

3.2 In vivo experiments

3.2.1 General remarks

All animal experiments were approved by the responsible authorities (governmental review committees on animal care). Experiments were approved by the LANUV. The described experiments performed by collaboration partners at AstraZeneca (United Kingdom) adhered to the Animal Scientific Procedures Act 1986 and complied with the Global Bioethics Policy. Animals were housed with controlled light cycles and had access to water and food ad libitum.

3.2.2 Detecting nanomedicines in vivo in tumors and brains via optical imaging

Using three different tumor models (A431, human epidermoid carcinoma; MLS, human ovarian carcinoma; CT26, murine colon carcinoma), the biodistribution and tumor accumulation of fluorophore-labeled PHPMA polymers was studied via optical imaging. Therefore, tumor cells were inoculated in the right flank (A431: 4 x 10^6 cells, MLS: 5 x 10^6 cells, CT26: 1 x 10^6 cells; in 100 µl medium) of anesthetized CD1 nude mice (2% vol/vol isoflurane). Food was changed to a chlorophyll-free diet (sniff Spezialdiäten) to reduce background signal three days in advance of the start of the injection of PHPMA polymers (normalized to dye amounts; 2 nmol) and when tumors reached a size of 7 mm. Upon injection of PHPMA polymers, mice were scanned using hybrid computed tomography-fluorescence molecular tomography (CT-FLT) 0.25, 4, 24 and 72 h post-injection. Mice were anesthetized and placed on a custom-made bed, CT-FLT imaging and image reconstruction were performed as described previously (Gremse et al., 2015, Gremse et al., 2016). Before mice were killed, they received an intravenous (i.v.) injection of rhodamine lectin to mark functional blood vessels. Excised organs and tumors were further scanned using fluorescence reflectance imaging (FRI) and tumors were eventually embedded in TissueTek O.C.T. (Sakura Finetek Europe).

The imaging of the accumulation of fluorophore-labeled PHPMA polymers and liposomes in the brain was slightly different. First, 2 sub-scans of the head were acquired using CT followed by FLT scans (two in total, one down- and one upwards). Image reconstruction was done as mentioned above. Upon receiving an i.v. rhodamine lectin injection, the mice were killed, and the brains were excised, scanned using FRI, and embedded in TissueTek. Several organs (e.g. brain, liver, kidneys, spleen, tumor) were scanned using FRI (FMT 2500 LC, Perkin Elmer) to additionally measure the fluorescence per organ ex vivo. Therefore, organs were placed on black cardboard inside the custom-made bed.

3.2.3 Tumor accumulation of doxorubicin-loaded and fluorophore-labeled liposomes

This set of experiments was performed at AstraZeneca, mainly led by Jennifer I. Moss. The experiments involving the tumor models OVFX899, LXFE1297, an RXF423 were conducted at Oncotest, which was in the meantime acquired by Charles River. The mice

received one i.v. slow bolus injection of liposomes upon an average tumor volume of 500 mm^3. Doxorubicin-loaded liposomes were injected in 5 mice per timepoint (2 or 6, 24, 72, and 120 hours) and upon killing, tumors were excised and immediately snap-frozen to allow the analysis of the doxorubicin concentration in tumors via liquid chromatography-mass spectrometry. Additional tumor-bearing mice were used to resect tumors for immunohistological analysis. Using comparably dosed, DiI-labeled DOPC/CHOL/mPEG2000-DSPE liposomes, the tumor accumulation of liposomes was visualized ex vivo using fluorescence microscopy. Further details are described in (May et al., 2024).

3.2.4 Sonopermeation to induce BBB opening allowing nanomedicine extravasation

Healthy CD-1 nude mice were randomly split into the following treatment groups: i) i.v. injection of PHPMA polymers, no sonopermeation; ii) i.v. injection of PHPMA polymers, with sonopermeation; iii) i.v. injection of liposomes, no sonopermeation; iv) i.v. injection of liposomes, with sonopermeation. One hour before the sonopermeation treatment, animals received 4 nmol of the respective nanomedicine formulation, i.e. either PHPMA polymers or liposomes, based on dye content. Animals of the sonopermeation groups were infused with 5 x 10^7 PBCA-MB over 5 min while ultrasound (16 MHz, MS250 transducer, Power Doppler ultrasound, 50% power, peak negative pressure of 1.8 MPa, mechanical index of 0.45, Vevo 2100 FUJIFILM VisualSonics) was applied for 5 minutes on the skull of anesthetized mice. Using optical imaging (CT-FLT), the accumulation of PHPMA and liposomes in the brain was evaluated 0.25 h before sonopermeation and 2, 4, and 24 h post sonopermeation treatment. Before mice were killed, rhodamine-labeled lectin was i.v. injected to mark functional blood vessels. Sonopermeation, imaging, and killing were performed under constant isoflurane (2%) induced anesthesia. Brains were resected, imaged via FRI, and embedded in TissueTek (Sakura Finetek).

3.3 Immunohistological stainings

3.3.1 Stainings of murine tumors to identify biomarkers for nanomedicine accumulation

Tumor samples of A431, MLS, and CT26 tumors were cut into sections with a thickness of 8 µm. A methanol-acetone-fixation was used (80 %v/v methanol for 5 min followed by 20 min of -20°C acetone). Primary antibodies were either incubated for 1 h at RT or overnight at 4°C, secondary antibodies were incubated for 1 h at RT. The applied antibodies are listed in Table 2. Microscopic images were acquired using an Axio Imager M2 microscope and four images of three sections per tumor were analyzed via the software FiJi (Schindelin et al., 2012).

Table 2: List of primary and secondary antibodies.

Antigens of primary antibodies	Host	Dilution	Catalogue number
Mouse CD31 (PECAM-1)	Rat	1:100	BD Biosciences # 553370
Mouse VEGFR2	Goat	1:20	R&D Systems # AF644
Mouse F4/80	Rat	1:50	Bio-Rad # MCA497GA
Murine & human Collagen Type I	Rabbit	1:100	Novus Biologicals (NB600-408)
Mouse Collagen IV	Rabbit	1:100	Novotec # 20451 0.5ml
Mouse Smooth Muscle Actin	Biotin	1:100	Progen # BK61501-1mg
Mouse LYVE-1	Rabbit	1:50	abcam # ab14917
Mouse CD68	Rabbit	1:100	abcam # 125212
Human CD31 Clone JC70A	Mouse	ready to use	DAKO Code IR610
Human CD68 Clone PG-M1	Mouse	ready to use	DAKO Code GA613
Antigens of secondary antibodies	**Conjugate**	**Dilution**	**Catalogue number**
Rat IgG (H+L)	Alexa Fl. 488	1:350	Dianova # 712-546-153
Rat IgG (H+L)	AMCA	1:50	Dianova # 712-155-153
Rabbit IgG (H+L)	Alexa Fl. 488	1:500	Dianova # 711-546-152

Rabbit IgG (H+L)	AMCA	1:50	Dianova # 111-155-003
Goat IgG (H+L)	AMCA	1:50	Dianova # 705-155-147
Biotin	Cy2	1:200	Dianova # 016-220-084
Mouse IgG (H+L)	HRP	1:200	Vector Laboratories #PI-2000
Rabbit/Mouse	HRP	ready to use	DAKO Code K8000

3.3.2 Stainings of human tumor microarrays

The stainings of human tumor sections and biopsies were performed at the Institute of Pathology by Saskia von Stillfried. The patient samples were picked to match the tumor entity and stage of the patients of the paper by Harrington et al. (Harrington et al., 2001), and are summarized in Table 3. The experiments were ethically approved by the ethics committee as well as registered at the Clinical Trial Center of Uniklinik RWTH Aachen (EK No. 22-294; CTC-A No. 21-359). Further details are described in (May et al., 2024). Image analysis was performed using QuPath (manual counting of blood vessels and automated positive cell detection of macrophages) (Bankhead et al., 2017).

Table 3: Overview of patient tumor samples used in tumor microarray and biopsy stainings.

Sample ID	Sex	Cohort	ICD-O code	Topography	TNM stage
BC1	Female	Breast	8500/3	C50	pT3pN1
BC2	Female	Breast	8500/3	C50	pT4pN3
BC3	Female	Breast	8500/3	C50	pT4pN2
BC4	Female	Breast	8500/3	C50	pT3pN2
BC5	Female	Breast	8500/3	C50	pT3pN0
BC6	Female	Breast	8500/3	C50	pT4pN3
BC7	Female	Breast	8500/3	C50	pT4pN2
BC8	Female	Breast	8500/3	C50	pT3pN3
BC9	Female	Breast	8500/3	C50	pT4pNX
BC10	Female	Breast	8500/3	C50	pT3pN1

HN1	Male	Head & neck	8070/3	C30	pT3pN0
HN2	Female	Head & neck	8070/3	C02	pT3pN1
HN3	Male	Head & neck	8070/3	C02	pT3pN2
HN4	Female	Head & neck	8070/3	C07	pT3pN1
HN5	Male	Head & neck	8070/3	C09	pT3pN1
HN6	Male	Head & neck	8070/3	C13	pT4pN0
HN7	Male	Head & neck	8070/3	C32	pT3pN0
HN8	Male	Head & neck	8070/3	C09	pT3pN1
HN9	Male	Head & neck	8070/3	C44	pT3pN1
HN10	Male	Head & neck	8070/3	C32	pT3pN0
LC1	Male	Lung	8070/3	C34	pT4pN1cM1
LC2	Male	Lung	8070/3	C34	pT3pN0
LC3	Male	Lung	8070/3	C34	pT3pN0
LC4	Male	Lung	8070/3	C34	pT3pN1
LC5	Female	Lung	8070/3	C34	pT3pN0
LC6	Male	Lung	8070/3	C34	pT3pN0
LC7	Female	Lung	8070/3	C34	pT3pN0
LC8	Male	Lung	8070/3	C34	pT3pN0
LC9	Male	Lung	8070/3	C34	pT3pN1
LC10	Male	Lung	8070/3	C34	pT3pN1

3.3.3 Stainings of murine brains

H&E stainings were performed at the Institute of Pathology using the routinely used, automated system (TissueTek Prisma, Sakura Finetek). Therefore, brain slices of 4 µm were used. IgG was stained as an endogenous marker for BBB opening using the horse anti-mouse IgG HRP -labeled (Vector Laboratories) and visualized with a Cy5.5 TSA dye (Perkin Elmer) following the standard TSA staining protocol for frozen samples.

3.4 Microscopy

3.4.1 Fluorescent and confocal microscopy as well as STED nanoscopy of nanomedicines in brain tissue

The distribution, extravasation, and penetration of fluorophore-labeled polymers and liposomes was assessed via fluorescence microscopy (using an Axio Imager M2 fluorescence microscopy, Carl Zeiss). Therefore, 8 µm sections of murine brains (3 slices per animal, cut using a Cryostat CM3050 S, Leica) were directly imaged with the 20x objective using the DsRed, GFP, and Cy7 channel. The acquired images were analyzed using FiJi (Schindelin et al., 2012) and the extravasation of polymers and liposomes was analyzed using Definiens Developer XD Software (Definiens AG).

For confocal and STED microscopy, 25-40 µm thick sections of murine brains were imaged using a Leica TCS SP8 (Leica). Therefore, the brain slices were placed on a high-precision cover glass (170 µm, No. 1.5H, Marienfeld) and embedded in Mowiol. Using the 93X/1.30 glycerol objective with glycerol immersion liquid type G with a refractive index of 1.45 and a white laser source, polymers, liposomes, and rhodamine lectin-marked vessels were imaged (rhodamine lectin was excited at a wavelength of 550 nm and emissions were detected between 560 and 650 nm, Atto-488 and Alexa-488 were excited at a wavelength of 498 nm and emissions were detected between 509 and 542 nm). Using a step size of 500 nm, three-dimensional images were acquired. Parts of the 3D stack were further imaged using STED microscopy, where Atto-488 and Alexa-488 were irradiated by the STED laser at a wavelength of 592 nm and rhodamine lectin was irradiated by the STED laser at a wavelength of 775 nm. The images were processed using Huygens Professional (Scientific Volume Imaging) and analyzed using Imaris Software (Imaris 7.4, Bitplane). The extravasation of polymers and liposomes was analyzed using an adapted MATLAB script based on the “Dilate Surface” Xtension in Imaris (as described in (Theek et al., 2016)).

3.5 Gradient tree boosting and Statistics

3.5.1 Gradient tree boosting

Gradient tree boosting was run using Python's Conda environment and XGBoost library version 1.4.2 on a computer using an Intel processor and Windows 10. First, the available data set was split into training, validation, and test data sets with specified ratio (70:15:15). The hyperparameters maximum depths, number of decision trees, and learning rate were investigated within the following boundaries, with all other hyperparameters being unchanged:

- Maximum depth: {3, 5, 7, 8, 9, 10}
- Number of decision trees: {10, 30, 50, 100}
- Learning rate: {0.1, 0.3}

A maximum depth of 8, 10 decision trees and a learning rate of 0.1 were chosen as the best set of hyperparameters due to the R2 values. Using these hyperparameters, the impact of individual biomarkers (parameters) on the prediction of polymer accumulation was investigated. Training and testing of the model were done using the leave-one-out approach, resulting in multiple repetitions to guarantee a split between training and testing. The importance of every individual biomarker on the prediction was sorted based on the average feature importance over all repetitions.

3.5.2 Statistics

The statistical analysis was performed using GraphPad Prism 5 and 9. Student's *t* test was used when two groups were compared, and one- or two-way ANOVA was used when multiple groups were compared. To analyze the GTB results, the Python environment was used. The specifically applied test and an explanation of p values are mentioned in each figure legend.

4 Results

4.1 Prediction of the tumor accumulation of nanomedicines using histopathological biomarkers

To investigate histopathological biomarkers for the prediction of the tumor accumulation of nanomedicines, an evaluation of the tumor accumulation of a prototypic polymeric drug carrier (PHPMA) was performed in three preclinical tumor models first.[1] The tumor sections of the three tumor models were stained for several biomarkers related to the tumor microenvironment and, supported by machine learning, a duo of predictive biomarkers was identified. Second, the biomarker set consisting of blood vessels and macrophages was validated in 10 additional tumor models, predicting the accumulation of liposomal doxorubicin. By using 3 additional tumor models in immunocompetent mice, a potential impact of the immune system was investigated, and still, blood vessels and macrophages were found to be predictive for tumor nanomedicine accumulation. Third, by combining historical tumor accumulation values of Doxil® and patient samples of comparable tumor entities and stages, a proof of concept on human tumors could be conducted, both on samples from tumor resection surgeries as well as the relative biopsies.

4.1.1 Optical imaging to assess PHPMA tumor accumulation

To enable the screening of biomarkers, the tumor accumulation of PHPMA was measured using hybrid computed tomography-fluorescence tomography (CT-FLT) imaging, followed by histopathological stainings (Figure 5 a). The biodistribution and tumor accumulation of fluorophore-labeled PHPMA was studied in mice using three different tumor models (A431, a human squamous cell carcinoma; MLS, a human ovarian carcinoma; CT26, a murine colon carcinoma).

[1] The results described in subchapter 4.1 are published in (May et al., 2024). Figures of the publication are presented upon adaption within this thesis, which is covered by the Creative Commons Attribution 4.0 International License (http://creativecommons.org/licenses/by/4.0/).

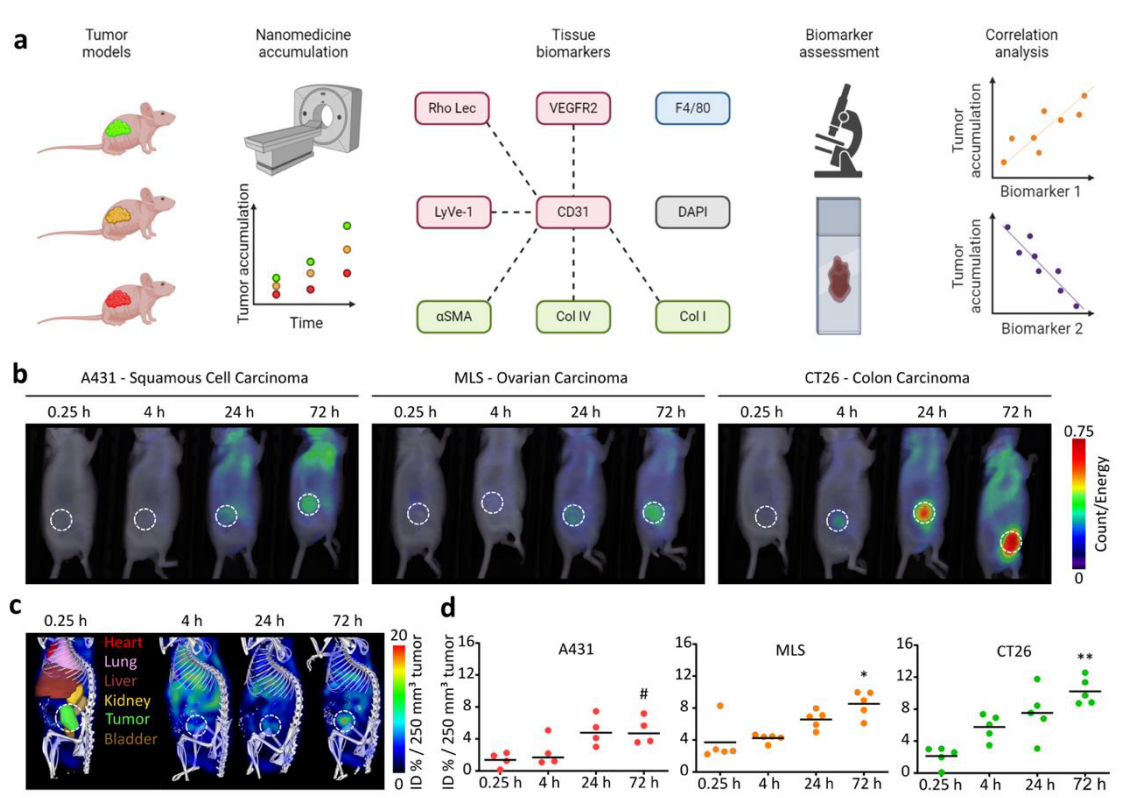

Figure 5: Optical imaging to measure and screening for histopathological biomarkers correlating with tumor accumulation of nanomedicines. Summarizing schematic describing the workflow. First, fluorophore-labeled PHPMA (10-20 nm in size) were injected i.v. into tumor-bearing mice (A431, MLS, or CT26) and the biodistribution and tumor accumulation was measured using CT-FLT. Second, the tumors were harvested and stained for 23 features of the tumor microenvironment to screen for possible biomarkers, that are connected to the vasculature (red), stroma (green), macrophages (blue), and cellular density (grey). Schematic created with BioRender.com **(a)**. Representative FRI scans of A431, MLS, or CT26 tumor-bearing mice 0.25, 4, 24, and 72 h post injection of fluorophore-labeled PHPMA. Tumors are indicated by white dashed circles **(b)**. Hybrid CT-FLT imaging allowed a segmentation of organs and tumor **(c)**. Furthermore, tumor accumulation of PHPMA is plotted over time, normalized to 250 mm^3 tumor volume. Each data point represents one animal, and the statistical significance was tested using Student's *t*-test (between two models) or one-way ANOVA (between all models). A431 versus MLS, $*P = 0.0168$; A431 versus CT26, $**P = 0.0025$; all models, $^{\#}P = 0.0024$ **(d)**. Adapted from (May et al., 2024).

Both the prototypic drug carrier as well as the tumor models were well established in the institute and known for a good tumor accumulation on the one hand as well as for different tumor microenvironments on the other hand. Upon tumors reached a sufficient size and days before the injection of the DY750-labeled PHPMA, the food was changed to a chlorophyll-free diet minimizing the background signal in the digestive tract. Mice were scanned via hybrid CT-FLT before the injection of PHPMA and immediately (0.25 h), 4, 24, and 72 h after the i.v. injection to longitudinally monitor the biodistribution and the tumor accumulation of PHPMA.

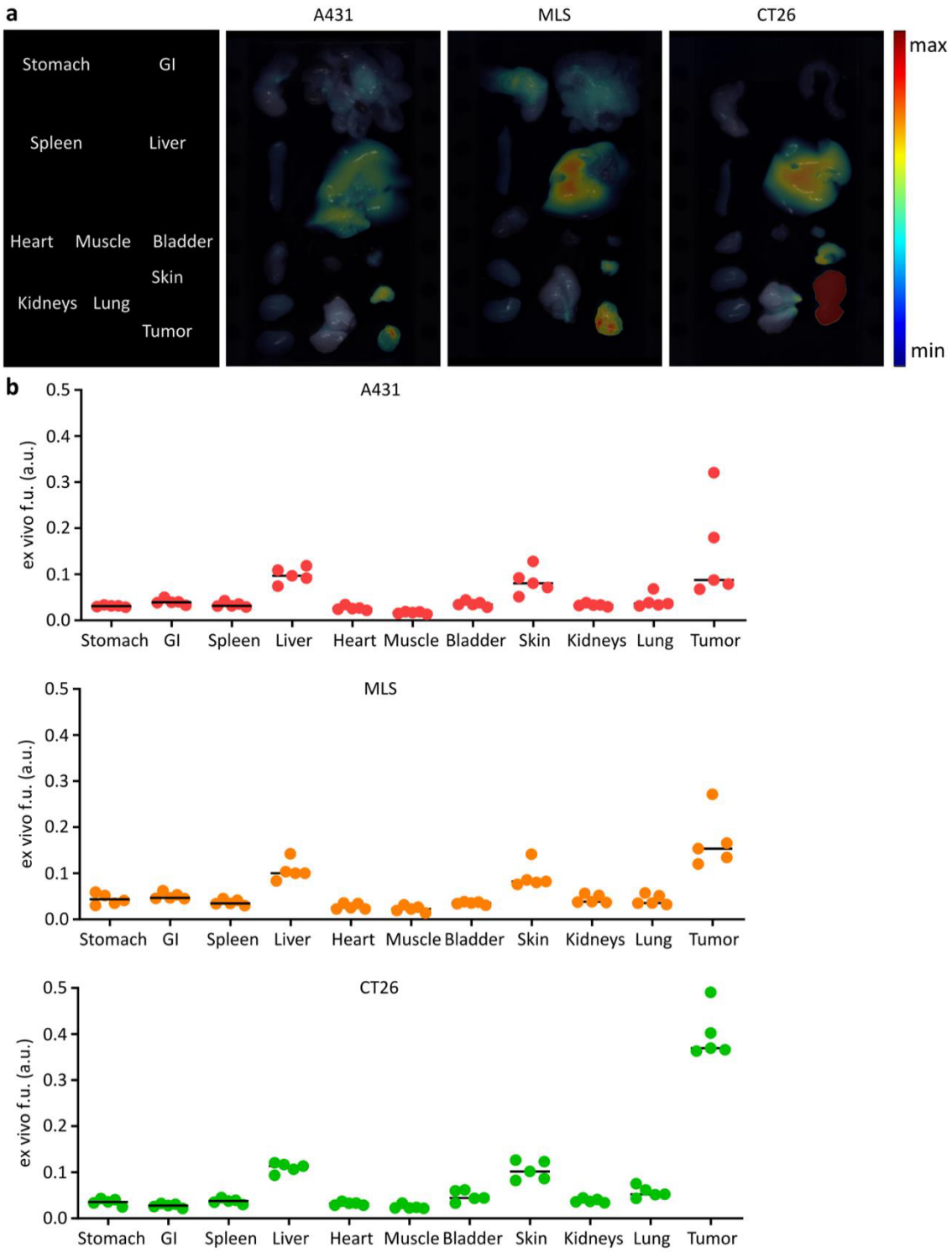

Figure 6: Ex vivo FRI analysis of the biodistribution of PHPMA. Immediately after killing and 72 h post injection, the A431, MLS, or CT26 tumor-bearing animals, organs and tumors were excised and imaged using fluorescence reflectance imaging allowing the assessment of the biodistribution of the DY750-labeled PHPMA **(a)**. For tumors and organs, fluorescence intensity was analysed, with each dot representing one animal **(b)**. Adapted from (May et al., 2024).

Exemplary shown are FRI scans of one mouse per tumor model and time-point (Figure 5 b). In addition, tumors and organs were segmented using Imalytics, allowing a quantification of accumulated PHPMA per organ, tumor, and volume (Figure 5 c, d). Already after 4 h, there was a noticeable difference in tumor accumulation, indicating a higher perfusion of MLS and CT26 tumors compared to A431 tumors. This trend was statistically significant at 72 h, which was directly before killing the animals, as the mean injected dose in % normalized to a volume of 250 mm^3 varied from 5.0 ± 1.7 for A431 to 8.5 ± 1.6 for MLS up to 10.2 ± 1.7 for CT26 (One-way ANOVA: *P*: 0.0024). Furthermore, the variation between and to some extent also within the tumor models illustrates a heterogenous tumor microenvironment, which is thought to be the most contributing factor for the accumulation of nanomedicines in solid tumors. After the mice were killed, the organs were excised and imaged using ex vivo FRI (Figure 6 a). Although ex vivo FRI is rather semi-quantitative as the fluorescent signal mainly relies on the surface of each organ rather than a complete assessment of the whole organ, there were notable differences between different organs and tumors, validating the in vivo CT-FLT results (Figure 6 b). The highest signal was found in livers and tumors (above 0.1 arbitrary units).

Taken together, these results showed the different tumor accumulation levels of fluorophore-labeled PHPMA in A431, MLS, and CT26 tumors, paving the way for further histopathological stainings.

4.1.2 Screening for histopathological biomarkers

Tumor sections of A431, MLS, and CT26 were stained using standard immunofluorescence protocols and imaged via fluorescence microscopy. Among the evaluated biomarkers, in addition to the pre mortem injected rhodamine lectin marking perfused vessels, were CD31 (blood vessels), αSMA (vessel maturity), VEGFR2 (angiogenesis), LYVE-1 (lymphatic vessels), F4/80 (macrophages), Col I (extracellular matrix), Col IV (vessel support), and DAPI (Figure 7 a-f, Figure 8 a, d, g). While these single biomarkers were analyzed by counting or area fraction measurements, double biomarkers were also evaluated, e.g. $lectin^+$, αSMA^+, or Col IV^+ blood vessels (Figure 7 g-l, Figure 8 b, e, h, j-n).

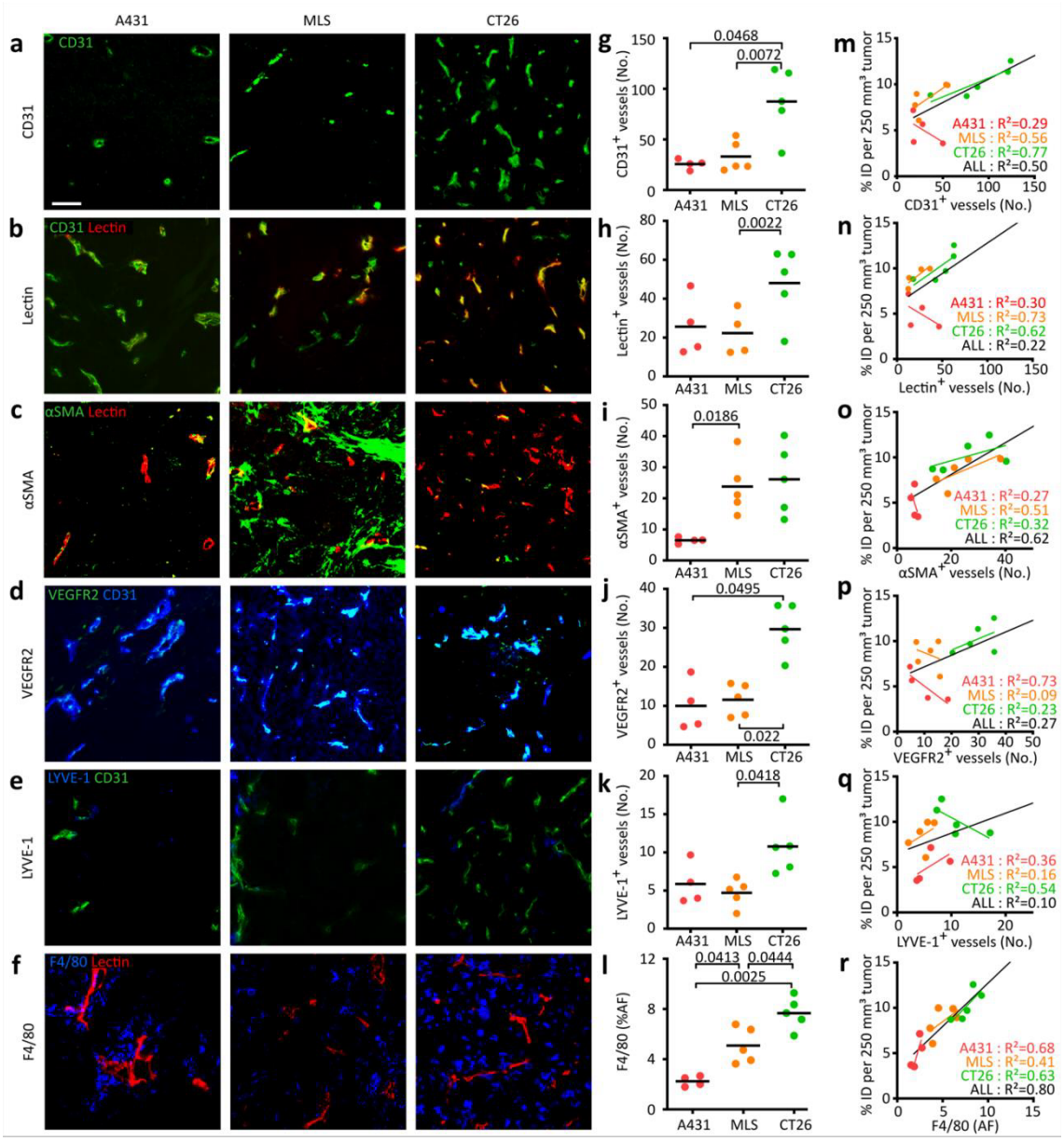

Figure 7: Screening of histopathological biomarkers of the tumor microenvironment to predict the tumor accumulation of nanomedicines (I). A431, MLS, and CT26 tumor sections were cut and stained for CD31 (blood vessels) **(a)**, lectin (perfused and functional vessels) **(b)**, αSMA (mature and pericyte supported vessels) **(c)**, VEGFR2 (angiogenic vessels) **(d)**, LYVE-1 (lymphatic vessels) **(e)**, F4/80 (tumor-associated macrophages) **(f)**; scale bar indicating 50 µm. The number of vessels were counted, either total vessels **(g)**, perfused vessels **(h)**, or mature, angiogenic, or lymphatic vessels **(i-k)**. For macrophages, the area fraction was determined **(l)**. Means are indicated by black bars, each dot represents one animal and statistical significance is based on Student's *t*-test with the respective *P* values shown. The quantified biomarkers **(g-l)** were correlated with the PHPMA tumor accumulation at 72 h, in % ID normalized to 250 mm³ tumor volume **(m-r)**. Trendlines are plotted per tumor model (color) and for all tumor models combined (black), and the R^2 values indicate the coefficient of determination and reflect the goodness of fit. Adapted from (May et al., 2024).

When comparing the tumor models A431, MLS, and CT26, CT26 was the model with the highest number of blood vessels, both total CD31⁺- and lectin⁺ blood vessels (total vessels: 28.5 ± 15.1 for A431 vs. 34.8 ± 18.0 for MLS vs. 89.0 ± 35.9 for CT26, functional vessels: 25.6 ± 15.5 for A431 vs. 22.3 ± 11.5 for MLS vs. 48.0 ± 18.8 for CT26, Figure 7 g,

h). The blood vessel density was also found to correlate better with the amount of accumulated polymer (% ID per 250 mm^3 tumor) than the number of functional vessels (R^2 of 0.50 vs. 0.22 over all three tumor models, Figure 7 m, n). The ratio of perfused vessels was found to be less important for the tumor accumulation of polymers than the total number of perfused vessels – as A431 had the highest percentage of lectin$^+$ blood vessels but also the lowest amount of accumulated PHPMA (ratio: 91.4% ± 6.7 for A431 vs. 62.7 ± 6.6 for MLS vs. 54.9 ± 4.0 for CT26, Figure 7 h and Figure 8 j).

In the case of blood vessel maturity, indicated by αSMA, there was also a discrepancy between the total number of αSMA$^+$ blood vessels and the ratio of αSMA$^+$ blood vessels. The total number of αSMA$^+$ blood vessels was significantly higher in MLS tumors compared to A431 tumors, with CT26 tumors presenting with comparable amounts of αSMA$^+$ blood vessels as MLS tumors, while the ratio of αSMA$^+$ blood vessels was significantly higher in MLS tumors compared to A431 and CT26 tumors (total number: 6.5 ± 0.9 for A431 vs. 23.8 ± 9.1 for MLS vs. 26.1 ± 11.3 for CT26, ratio: 25.9 ± 5.4 for A431 vs. 71.9 ± 12.3 for MLS vs. 32.7 ± 10.8 for CT26, Figure 7 i and Figure 8 k). In line with that finding, the total number of αSMA$^+$ blood vessels was a decent predictor for the tumor accumulation of PHPMA (R^2: 0.62, Figure 7 o). Angiogenic vessels, indicated by VEGFR2 expression, also showed the highest total number in CT26 tumors while A431 and MLS tumor presented with comparably low counts (10.0 ± 6.5 for A431 vs. 11.6 ± 4.1 for MLS vs. 29.7 ± 6.5 for CT26, Figure 7 j). In general, the ratio of VEGFR2$^+$ vessels was high, with more than 70% in all tumor types (85.2 ± 10.0 for A431 vs. 72.3 ± 13.4 for MLS vs. 76.5 ± 4.6 for CT26, Figure 8 l), and neither to total number of angiogenic vessels nor the ratio was predictive for tumor accumulation (R^2: 0.27, Figure 7 p).

Lymphatic vessels are stained by using LYVE-1, and were found in quite low levels in all three tumor models, with CT26 showing significantly more LYVE-1$^+$ vessels than MLS, but not A431 (5.9 ± 2.8 for A431 vs. 4.7 ± 1.8 for MLS vs. 10.8 ± 2.8 for CT26, Figure 7 k). Also due to the low dynamic range of lymphatic vessels, they seem to be at best weakly connected to PHPMA tumor accumulation (R^2: 0.10, Figure 7 q), which might be explainable by their mixed impact on drug delivery processes. On the one hand, no lymphatic vessels can result in tumors with a high interstitial fluid pressure, inhibiting the extravasation of nanomedicines out of blood vessels, while on the other hand, a high

number of lymphatic vessels can enhance the removal out of the tumor. In contrast, the amount of macrophages differed substantially among all models with A431 with the lowest, MLS with an intermediate, and CT26 with the highest amount of macrophages (2.2 ± 0.4 for A431 vs. 5.1 ± 1.4 for MLS vs. 7.7 ± 1.3 for CT26, Figure 7 l). As a result, the tumor accumulation of PHPMA correlated very well with the amount of macrophages (R^2: 0.80, Figure 7 r).

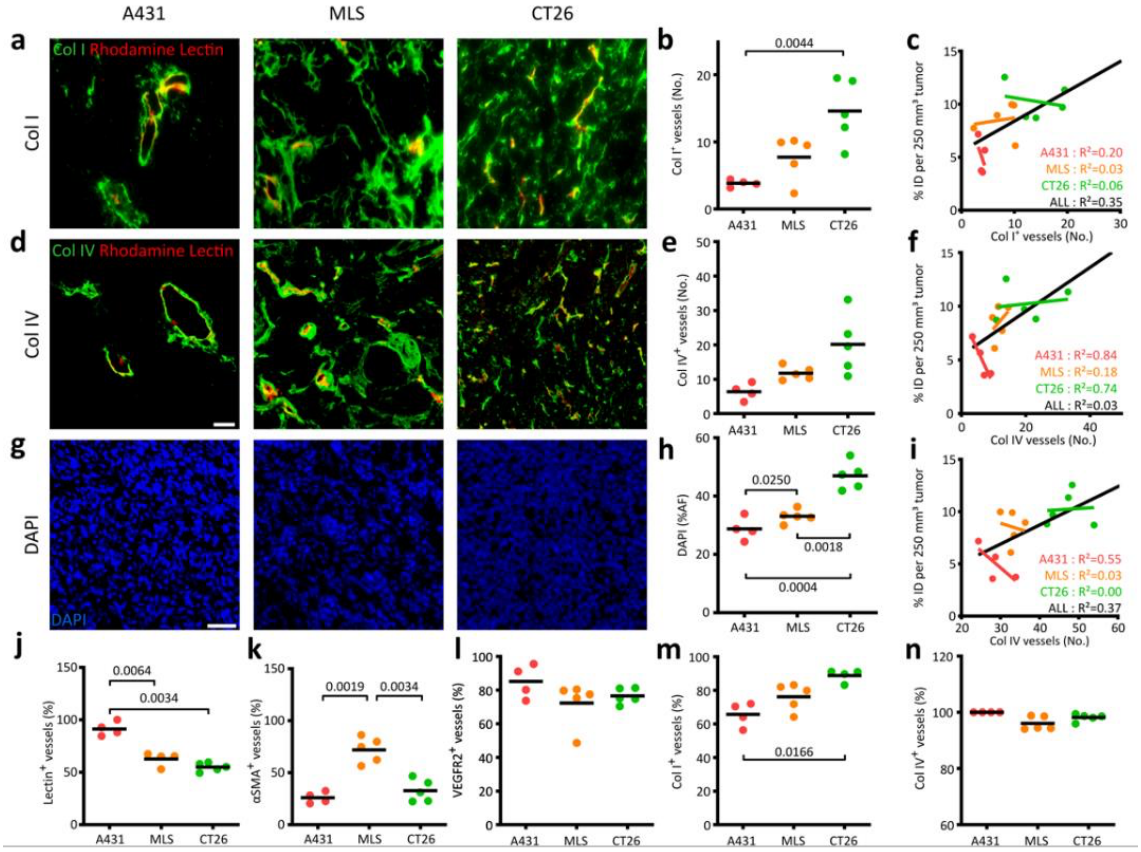

Figure 8: Screening of histopathological biomarkers of the tumor microenvironment to predict the tumor accumulation of nanomedicines (II). A431, MLS, and CT26 tumors were cut and stained for Col I (collagen I) **(a)**, Col IV (collagen IV) **(d)**, and DAPI (nuclei) **(g)**. Scale bar indicates 50 µm. Images were quantified **(b, e, h)** and correlated with the PHPMA tumor accumulation values 72 h post injection (in % of the injected dose, normalized to 250 mm^3 **(c, f, i)**. As an attachment of **Figure 7** the ratio of lectin **(j)**, αSMA **(k)**, VEGFR2 **(l)**, Col I **(m)**, and Col IV **(n)** positive vessels to the total number of blood vessels was plotted. Statistical significance is based on Student's *t*-test with the respective *P* values shown, and trendlines are plotted per tumor model (color) and for all tumor models combined (black), with the R^2 values indicating the coefficient of determination and reflect the goodness of fit. Adapted from (May et al., 2024).

An important component of the extracellular matrix are collagens, here, collagen I (general ECM protein) and collagen IV (blood vessel stability) were stained. The number of Col I and Col IV positive vessels increased from A431 to MLS to CT26 with very high ratios for both collagens (above 60% for Col I, and almost 100% for Col IV, in all three

tumor models) without being very predictive for the tumor accumulation of PHPMA (R^2: 0.35 for Col I and R^2: 0.03 for Col IV, Figure 8 b, e and c, f). The cellularity, indicated by DAPI, seems also to be barely connected with the tumor-targeted drug delivery of nanomedicines, at least in the three here investigated tumor models (R^2: 0.37, Figure 8 h,i).

Taken together, the screening for histopathological biomarkers that are predictive for the tumor accumulation of PHPMA as a representative nanomedicine revealed blood vessels and macrophages as promising candidates.

4.1.3 Identification of histopathological biomarkers using machine learning

The attempts in identifying histopathological biomarkers for nanomedicine tumor accumulation has so far only focused on single biomarkers or combinations (e.g. macrophages, blood vessels, extracellular matrix proteins, or angiogenic or mature blood vessels). As within this study, over 20 different parameters per animal have been evaluated, it seemed reasonable to apply computational power and test, if the tumor accumulation can be predicted based on the information collected in the whole data set. Gradient tree boosting was found to be a suitable method, as it does not require massive data sets and aims to predict one parameter based on a data set of several parameters (Figure 9 a). The acquired data set was not large enough to split training and testing populations, which was tackled by using the leave-one-out method (13 animals were used for training, and one for testing, with five repetitions). Additional settings included the maximum usage of ten decision trees, each with a maximum depth of 8 questions. Eventually, gradient tree boosting predicted the tumor accumulation of PHPMA (in % ID per 250 mm^3), which was plotted against the values measured by hybrid µCT-FLT (from Figure 5 d), and resulted in a coefficient of determination of R^2: 0.70 (Figure 9 b). This prediction was based by using only 6 of the 23 features, which does not indicate that the remaining 17 features were not connected to the tumor accumulation of PHPMA, but rather that they did not provide any additional input that was not covered by the used 6 features (Figure 9 c). All the important features were either linked to the vasculature or to macrophages, validating the findings of the screening for histopathological biomarkers.

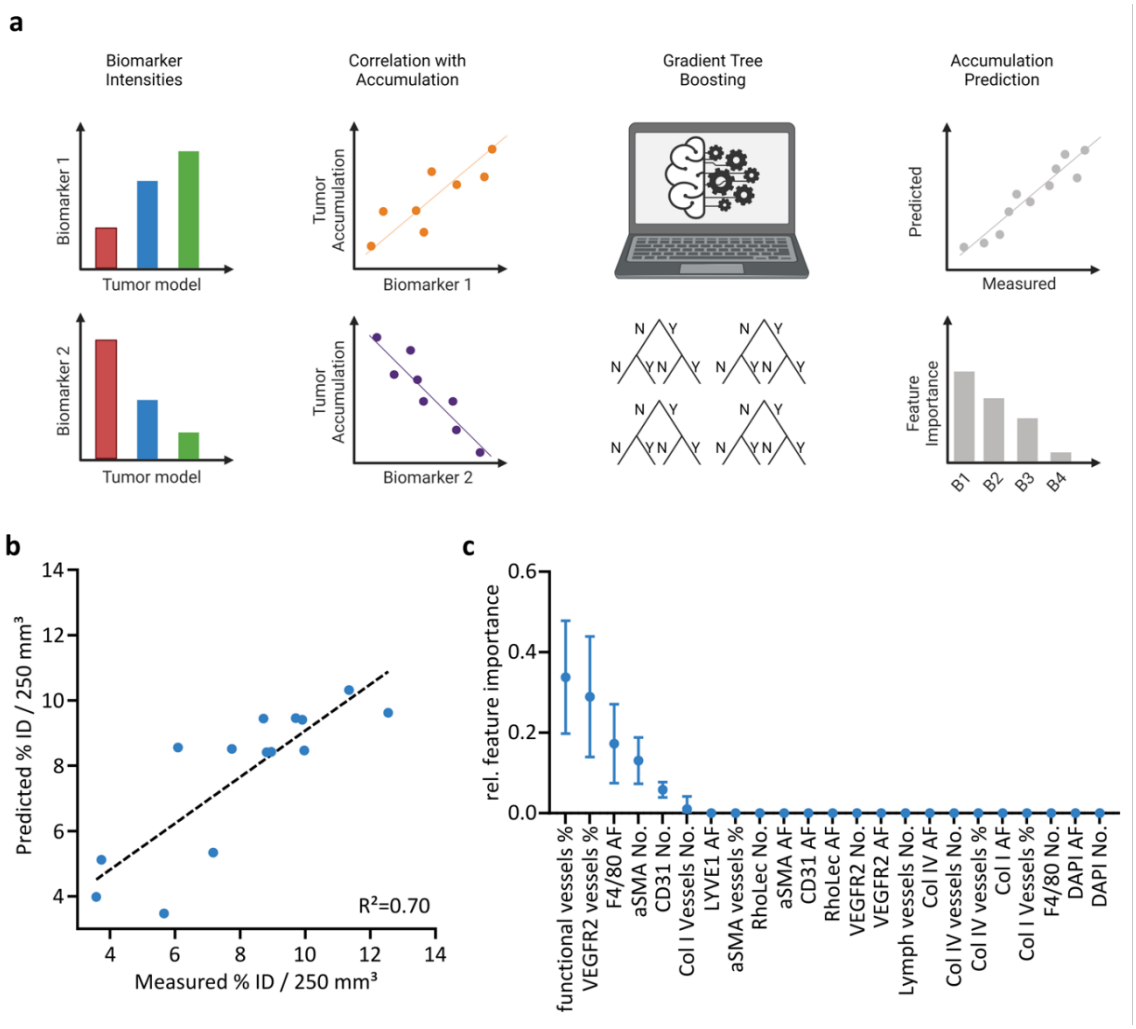

Figure 9: Gradient tree boosting to evaluate the importance of histopathological biomarkers. Upon the quantification of histopathological stainings and their correlation with the tumor accumulation of PHPMA, the acquired data set was fed into a machine learning tool (gradient tree boosting). By using decision trees with simple yes and no answers, the algorithm tries to predict the measured tumor accumulation values based on the acquired biomarker data, also revealing the importance of each feature **(a)**. The tumor accumulation values were predicted quite accurately, using *N*-fold cross validation, with the R^2 value indiating the coefficient of determination and reflecting the goodness of fit **(b)**. All assessed histopathological features are ranked from high to low based on their appearance in the decision trees predicting PHPMA tumor accumulation, with error bars indicating the standard deviation (n=14) **(c)**. Adapted from (May et al., 2024).

4.1.4 Verification of blood vessels and macrophages as biomarkers in ten additional preclinical tumor models

Blood vessels and macrophages were found to be promising candidates to predict the tumor accumulation of nanomedicines, however, that finding was so far based on three preclinical tumor models. Therefore, an extensive validation study was conducted, which included ten additional preclinical tumor models (the four cell line derived models

Calu-3, SW620, A549, and Calu-6; and the six patient-derived xenograft models E35CR, REN, CRC, E77, NSCLC, and OV). These models were chosen to display very different tumor microenvironments and not to tailor the biomarker-based approach to one specific tumor entity. Additionally, the nanomedicine formulation was switched from PHPMA to a PEGylated liposome, either dye-labeled or doxorubicin-loaded and comparable to Doxil®. Using the DiL-labeled liposomes, their tumor distribution was assessed via fluorescence microscopy (Figure 10 a), indicating quite different accumulation profiles. As a follow-up, 20 mice per tumor model were i.v. injected with doxorubicin-loaded liposomes and the drug concentration in the tumor was measured via liquid chromatography-mass spectrometry 2 respectively 6, 24, 72, and 120 h post injection (five mice per timepoint, Figure 10 b). The area under the curve ($AUC_{0\text{-}120}$) was calculated per tumor model (Figure 10 c), with E35CR and Calu-3 as the highest accumulating tumor models and SW620, A549, and Calu-6 as the lowest accumulating tumor models, which was in line with the tumor accumulation levels of the DiL-labeled liposomes (with AUCs of 163.7 ± 27.0 for E35CR vs. 118.9 ± 24.3 for Calu-3 vs. 16.1 ± 2.1 for SW620 vs. 6.6 ± 1.7 for A549 vs. 5.4 ± 1.3 for Calu-6, Figure 10 a, b, c).

To simulate the workflow of the clinic, the switch from immunofluorescent stainings to pathology's standard staining method was made, which is based on secondary antibodies labeled with HRP and stain the antigen using the dye DAB (3, 3'-diaminobenzidine). Tumor sections of E35CR, Calu-3, REN, CRC, E77, NSCLC, OV, SW620, A549, and Calu-6 were stained for both CD31 and F4/80, to mark blood vessels or macrophages, and counterstained using hematoxylin (Figure 10 d). Blood vessels (Figure 10 e) and macrophages (Figure 10 g) were counted per field of view and eventually plotted against the $AUC_{0\text{-}120h}$ (Figure 10 f and h). In general, there was a positive correlation between both the number of blood vessels as well as macrophages and the amount of accumulated doxorubicin, indicating liposome accumulation. The tumor model E35CR was included although it appeared to be most likely an unexplainable outlier, with an almost unrealistic high tumor accumulation of liposomes (see the image in Figure 10 a) while in contrast presenting with comparable low numbers of blood vessels and macrophages.

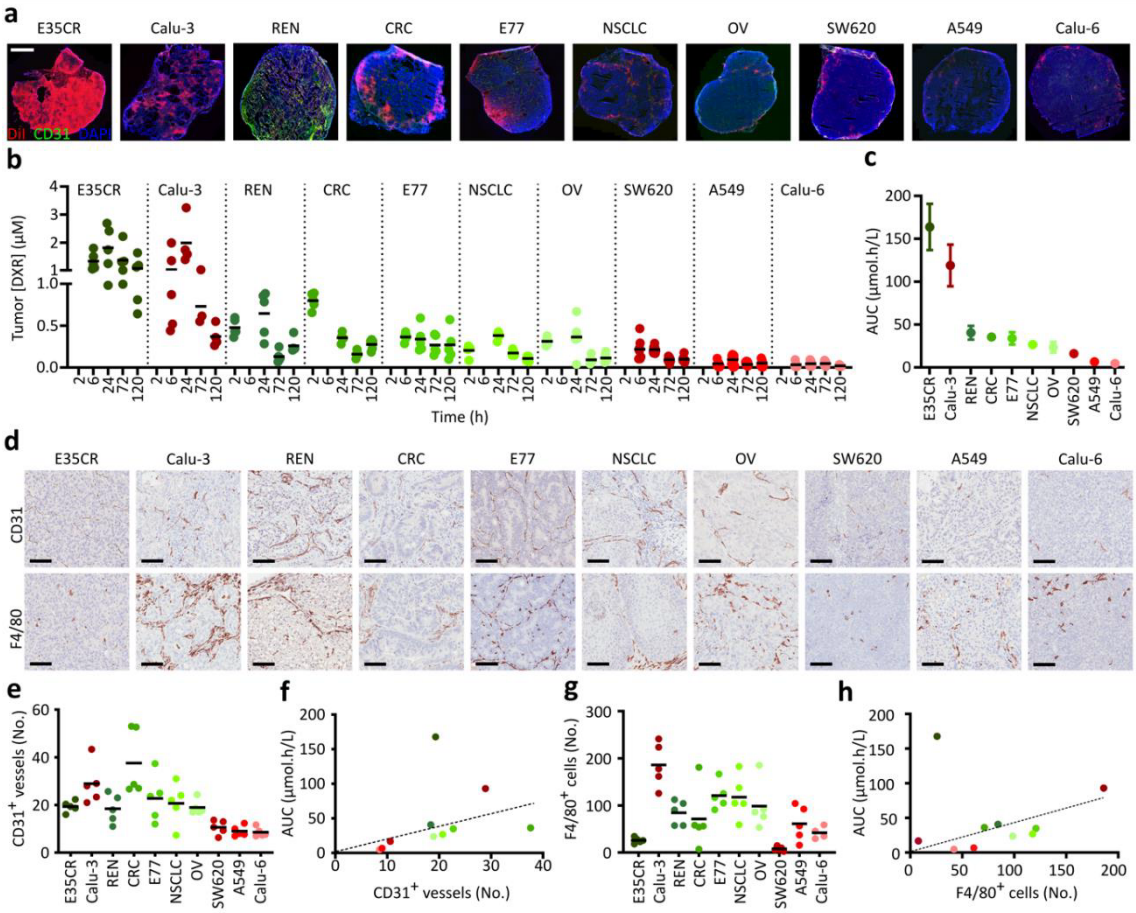

Figure 10: Preclinical validation of blood vessels and macrophages in 10 preclinical tumor models injected with liposomal doxorubicin for the prediction. Tumor bearing animals (E35CR, Calu-3, REN, CRC, E77, NSCLC, OV, SW620, A549, Calu-6) were injected with DiL-labeled PEGylated liposomes**.** Animals were killed 24 h upon injection, tumors excised, cut and stained for CD31 and cell nuclei. Scale bar indicates 200 µm **(a)**. The tumor concentration of liposomal doxorubicin was assessed 2, 6, 24, 72, and 120 h post injection via liquid chromatography-mass spectrometry in five mice per time point and tumor model. Black bars indicate the mean **(b)**. The tumor concentration values from (b) were used to calculate the area under the curve ($AUC_{0\text{-}120h}$), with the dots indicating the mean, and the error bars the standard error of the mean **(c)**. Tumor sections were stained for CD31 or F4/80 using DAB stainings, with the scale bars indicating 100 µm **(d)**. Blood vessels **(e, f)** and macrophages **(g, h)** were counted and plotted with the $AUC_{0\text{-}120h}$, with the black bars indicating the mean and the dashed lines indicating the trendline. Adapted from (May et al., 2024).

Next, blinded pathologists and scientists were asked to score the levels of CD31 and F4/80 expression, aiming for an approach to identify lower and higher accumulating tumor models (Figure 11 a). Therefore, an image collection consisting of pairs of one image of a CD31 staining and one image of an F4/80 staining was sent around (three pairs per tumor model, 60 images in total). Scientists (ten in total, including three board-certified pathologists) were asked to rate the amount of CD31 and F4/80 expression from absent (score of 1), low (score of 2), intermediate (score of 3) to high (score of 4) (Figure 11 b). The resulting scores were multiplied per image pair and plotted in a

heatmap against the tumor accumulation of doxorubicin-loaded liposomes, with a darker blue color indicating more hits per final score and tumor model (Figure 11 c).

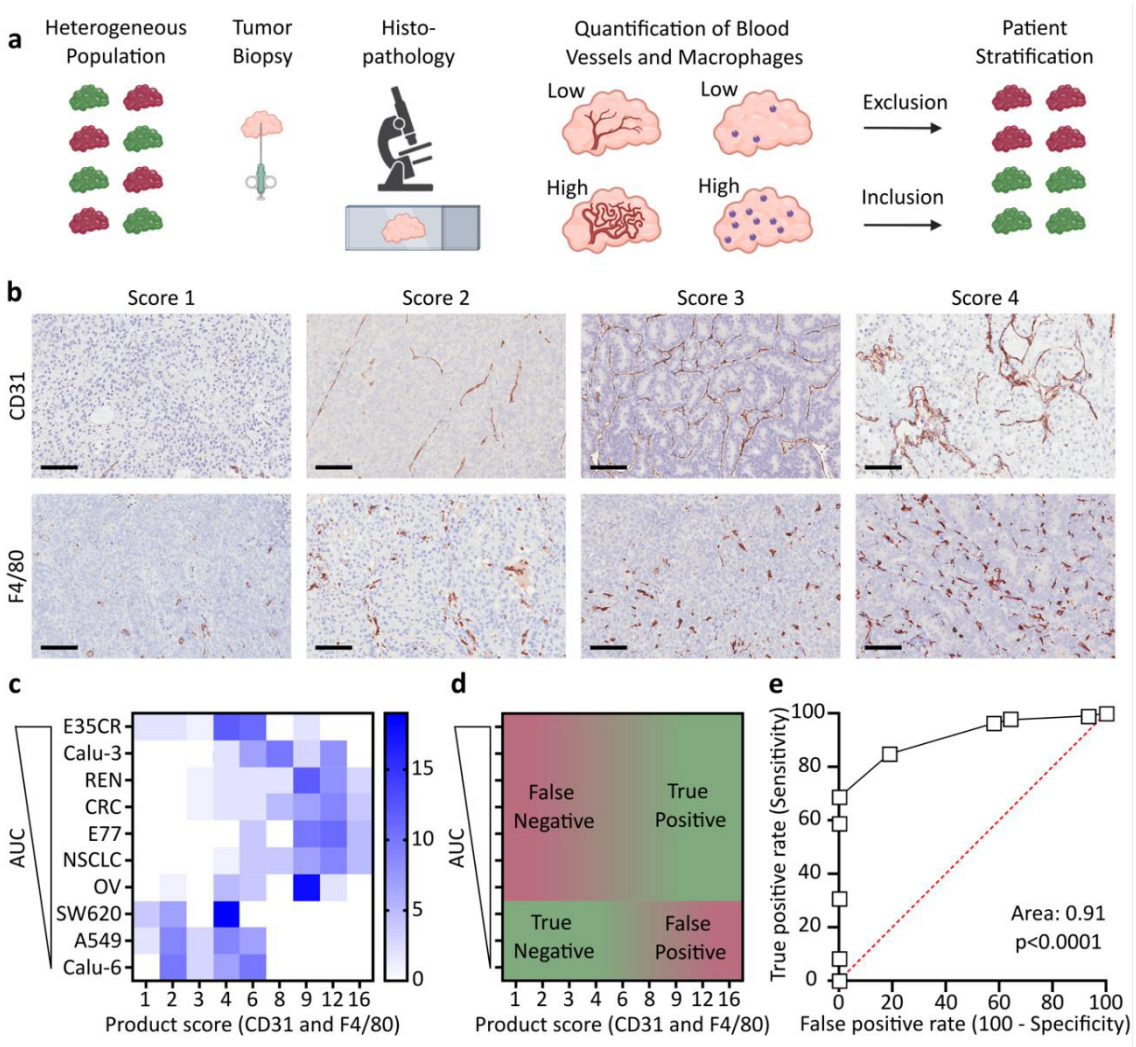

Figure 11: Predicing nanomedicine tumor accumulation with a product score of blood vessels and macrophages. Illustration of the clinical use of histopathological biomarkers for patient stratification in cancer nanomedicine trials **(a)**. Exemplary images of CD31 and F4/80 stainings covering the range of low to high biomarker expression (scores from 1 to 4). 10 blinded scientists were asked to score pairs of both stainings to simulate a clinical workflow, with three pairs sent around per tumor model. Scale bars indicate 100 µm **(b)**. The scores from (b) were plotted in a heatmap against the $AUC_{0\text{-}120h}$ with the tumor models being sorted from the lowest accumulation (bottom) to the highest (top). Color intensity indicates the number of product scores per score and tumor model **(c)**. Heatmap indicating true and false positives and negatives **(d)**. Using the data from (c), a receiver operating characteristic curve (ROC) was calculated showing a very high accuracy of the blood vessels and macrophages prodcut score in discriminating between low and high accumulating tumor models **(e)**. Adapted from (May et al., 2024).

By doing so, especially the low accumulating models SW620, A549, and Calu-6 could be identified in the lower left corner, pointing towards a threshold of 7 to differentiate between low and high accumulating tumor models (Figure 11 c, d). Besides the outlier E35CR, the remaining six models were correctly rated as high accumulating models. In

total, the product score was very accurate in predicting the tumor accumulation which is represented by an AUROC value of 0.91 (Figure 11 e).

Using ten additional preclinical tumor models, and switching from immunofluorescent to immunohistochemistry stainings, the identified biomarkers blood vessels and macrophages were again able to differentiate between low and high accumulating tumor models. Taken together, these findings motivated the further translation of the duo of biomarkers on patient data sets.

4.1.5 Considering differences between preclinical tumor models and human patients

When comparing the biomedical background of the tumor models and especially the host animals with human patients, two main differences have to be considered. First, the used preclinical tumor models have all been inoculated in immune-compromised mice which is on the one hand a requirement for the growth of human cancer cells, but on the other hand neglects a potential influence of the immune system on the tumor microenvironment as well as on the tumor accumulation of nanomedicines. Therefore, the tumor accumulation of both fluorophore-labeled PHPMA and fluorophore-labeled liposomes was evaluated in immune-competent mice (PHPMA in orthotopic 4T1 tumor-bearing BALB/c mice, liposomes in subcutaneous and orthotopic Hep-55.1C tumor-bearing C57BL/6J mice).

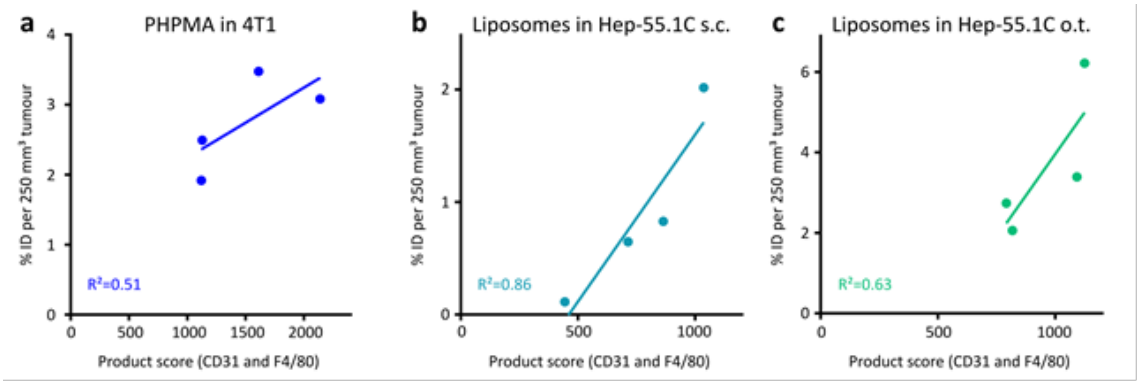

Figure 12: Assessing blood vessels and macrophages as biomarkers for the tumor accumulation of nanomedicines in immuno-competent models. The tumor accumulation of fluorophore-labeled PHPMA polymers was measured using hybrid µCT-FLT and plotted against the product score of blood vessels (CD31) and macrophages (F4/80) in 4T1 tumor-bearing BALB/c mice **(a)**. In C57BL/6J mice, which grew a subcutaneous **(b)** or orthotopic **(c)** Hep-55.1C tumor, the tumor accumulation of fluorophore-labeled liposomes was evaluated via hybrid µCT-FLT and plotted against the product score of blood vessels (CD31) and macrophages (F4/80). Adapted from (May et al., 2024).

In all three models, tumor accumulation of either PHPMA or liposomes correlated well with the product score of CD31 and F4/80 (indicated by R^2 values of 0.51, 0.86, and 0.63; see Figure 12 a-c). These findings indicate that blood vessels and macrophages as biomarkers for the tumor accumulation of nanomedicines also work in mice with an intact immune system.

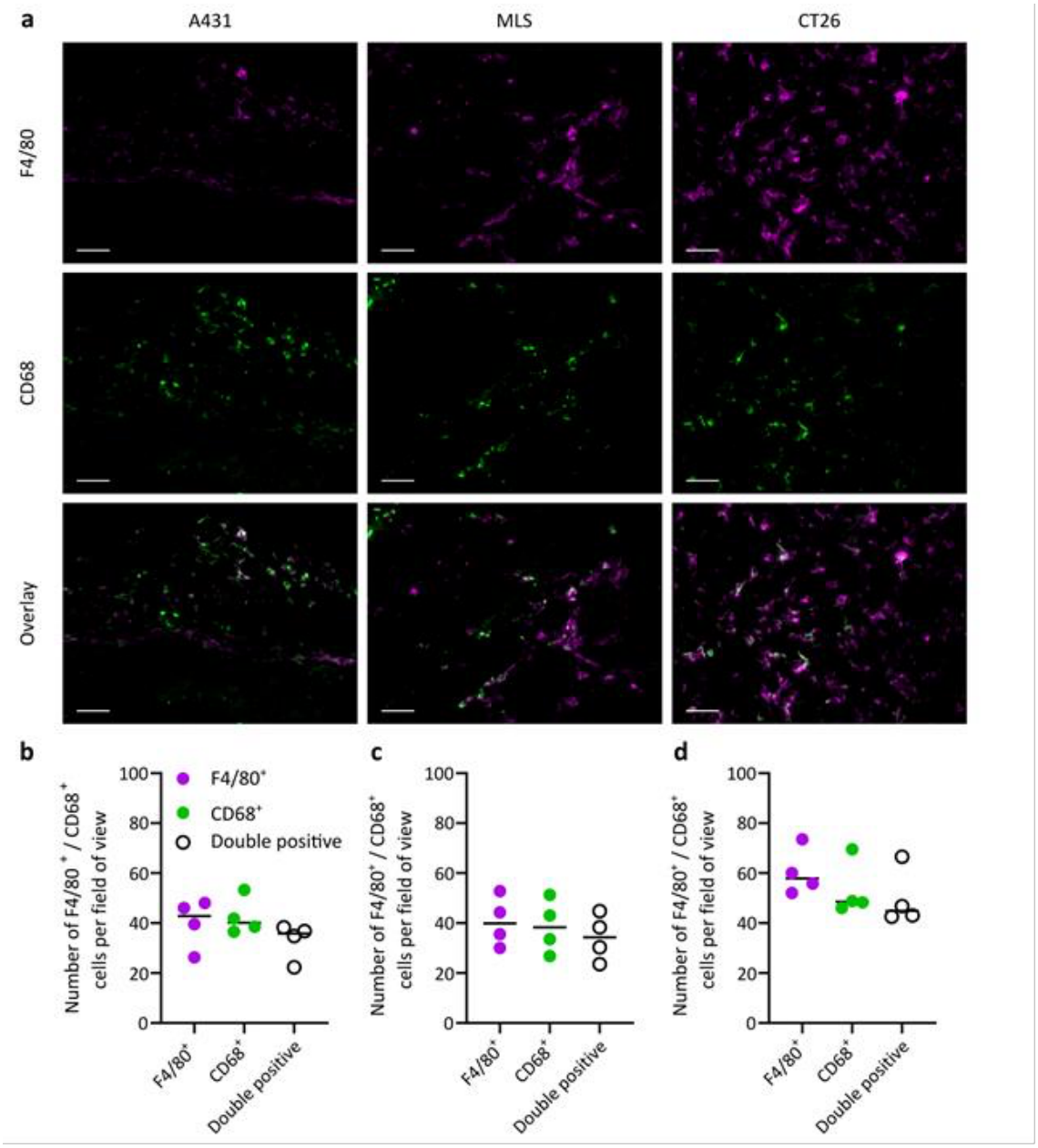

Figure 13: Comparing F4/80 and CD68 stainings of tumor-associated macrophages. Co-stainings of F4/80 and CD68 for tumor-associated macrophages of A431, MLS, and CT26 tumors (scale bar indicates 50 µm) **(a)**. Macrophages positive for F4/80, CD68, or both were counted and plotted for A431 **(b)**, MLS **(c)**, and CT26 **(d)**. Adapted from (May et al., 2024).

Second, for macrophage stainings, different antigens have been used in mice and in humans. In mice, the most common murine macrophage marker F4/80 was stained, while CD68 has been established as the gold standard to stain for macrophages in human samples. However, in an F4/80-CD68 co-staining on murine samples the expression patterns and number of $F4/80^+$ and $CD68^+$ cells was assessed (Figure 13 a, please notice the white color in the overlay indicating double positive pixels). Upon counting the number of F4/80 positive cells as well as the number of CD68 positive cells and double positive cells in A431, MLS, and CT26 tumors (Figure 13 b, c, d), comparable values of macrophages were detected. This indicates that a switch from F4/80 to CD68 should provide a similar predictive biomarker, as both antigens mark the same cell type.

4.1.6 Translating the biomarker product score using patient datasets

As it was not possible to get access on a data set including biopsies or resected material of cancer patients who were treated with e.g. Doxil® or another nanomedicine and whose tumor accumulation was measured (or the therapeutic response was known), we proceeded with an indirect comparison. Using the tumor accumulation values published by Harrington et al. of ^{111}In-labeled PEGylated liposomes, which were imaged and quantified using SPECT imaging, in 17 patients suffering either from ductal breast cancer, squamous cell carcinoma of the lung, or squamous cell head and neck cancer (Harrington et al., 2001), comparable tumor resection samples and the matching biopsies were collected from the archive of the Institute of Pathology of the RWTH Aachen University Hospital. For each of the three tumor types, samples from 10 patients were collected, whose tumors presented comparable characteristics, e.g. entity and stage (Table 3). Using the tumor specimen that were removed during surgery, tumor microarrays were prepared with five to six 2 mm punches per patient, which were stained for either CD31 or CD68 (Figure 14 a, b). The number of blood vessels and macrophages were counted (blood vessels manually, macrophages using QuPath's automated positive cell detection (Bankhead et al., 2017)). Breast cancers were found to have significantly less blood vessels than lung or H&N cancers (40.8 ± 19.2 for breast vs. 77.7 ± 21.2 for lung vs. 95.6 ± 23.2 for H&N cancers, Figure 14 c), and significantly lower numbers of macrophages than lung cancers (267.9 ± 223.8 for breast vs. 798.9 ± 679.1 for lung vs. 488.2 ± 445.7 for H&N cancers, Figure 14 d). When plotting the mean liposome tumor accumulation values of breast, lung, and H&N cancers, which were

taken from Harrington et al. (replotted in Figure 14 e (Harrington et al., 2001)), against the product of CD31 and CD68 counts, the lowest accumulating tumor, breast cancers, could be clearly identified (Figure 14 f). Additionally, the product scores for lung and H&N cancers were mostly substantially higher, which pointed not only towards an identification of most likely not or low accumulating tumors, but also towards the correct prediction of medium to high accumulating tumors.

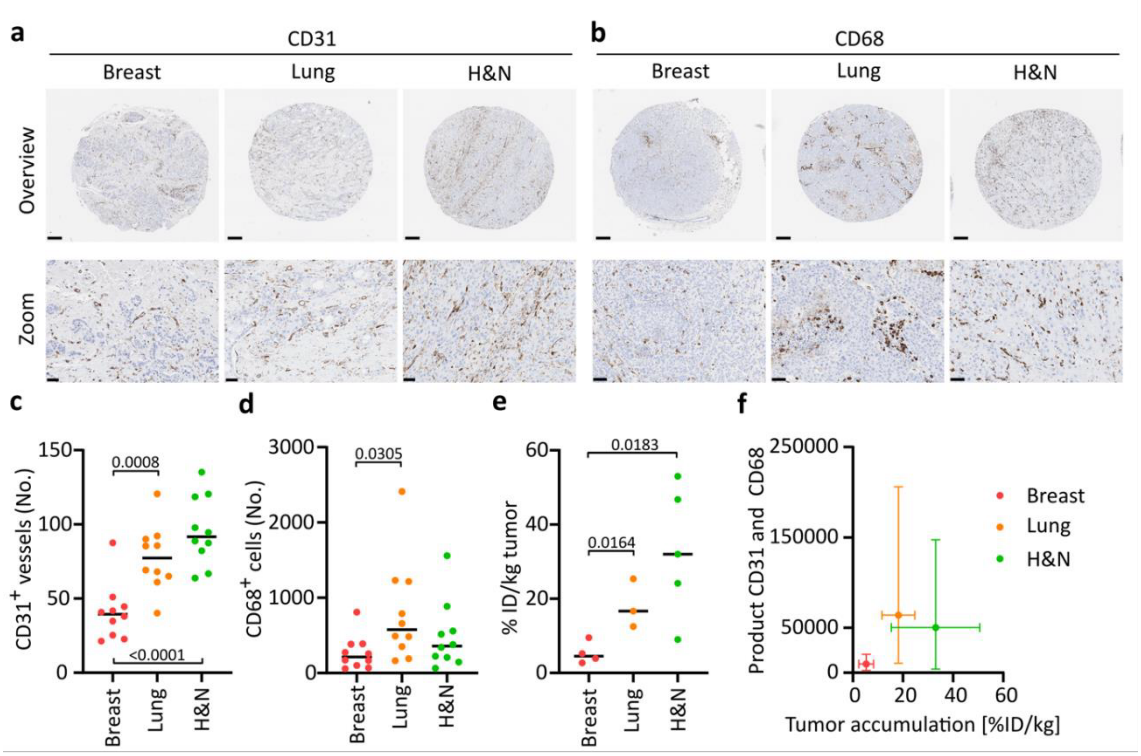

Figure 14: Histopathological biomarkers for the prediction of nanomedicine accumulation using patient samples. Tumor tissues from surgical resections of breast, lung, and head and neck (H&N) cancer patients were used to generate tissue microarrays with 5-6 punches per patient (ten patients per tumor type). Microarrays were stained for CD31 and CD68, representative images and zoom ins are shown **(a,b)**. Blood vessels and macrophages were counted, each dot represents the mean of one patient. Statistical significance is indicated based on Student's *t*-test (*P* values plotted) **(c,d)**. Using already published data from Harrington et al. (Harrington et al., 2001), tumor accumulation values are replotted of ^{111}In-labeled, PEGylated liposomes in breast, lung, and head and neck cancer patients (in % of the injected dose, normalized per kg of tumor tissue, with *P* values based on Student's *t*-test) **(e)**. CD31 and CD68 means were multiplied and plotted against the accumulation values of Harrington et al. (Harrington et al., 2001), with the error bars indicating the range of %ID per kg and the CD31*CD68 product scores (y-axis: minima and maxima, x-axis: standard deviation; n=3-10, as these dots are based on the means of c, d, and e) **(f)**. Adapted from (May et al., 2024).

The above presented validation on human samples was based on tissues collected in tumor resection surgeries. Keeping the underlying principle in mind, a usage of biopsies would have been more interesting but due to ethical reasons, the work was first conducted on resected material, which was available in larger volumes per patient.

Upon the successful validation of blood vessels and macrophages as predictive biomarkers for the tumor accumulation of nanomedicines, the procedure was repeated on biopsy samples, which were available for 28 of the 30 included patients.

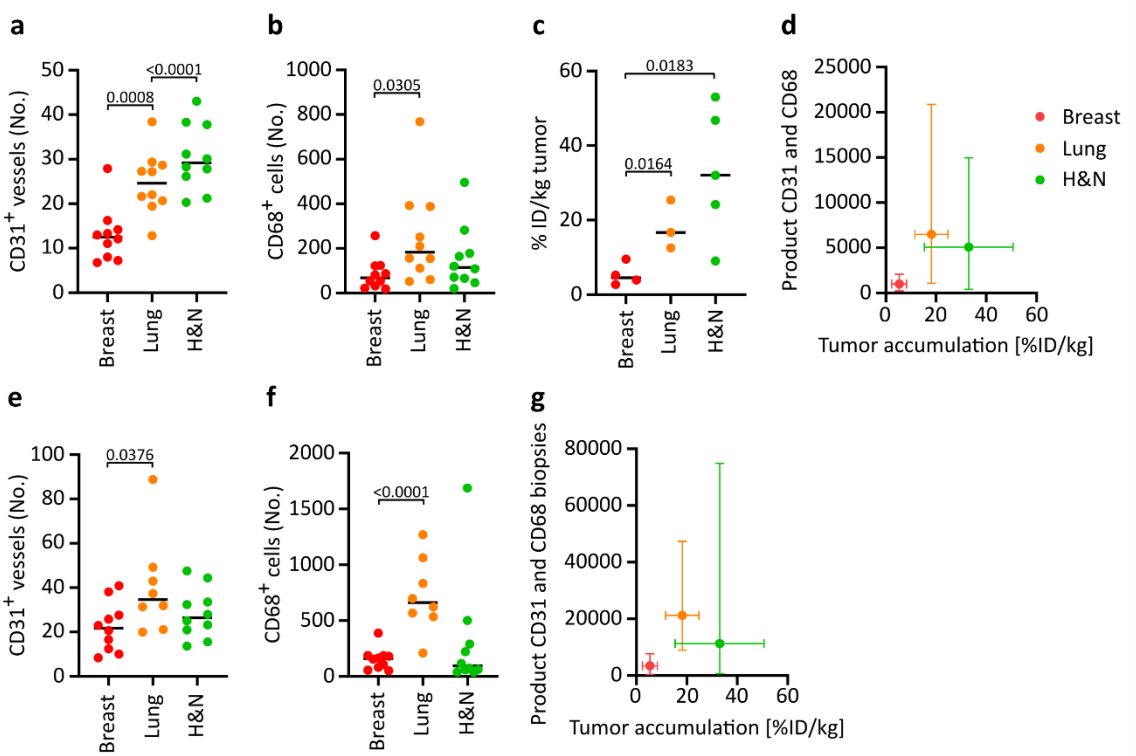

Figure 15: Blood vessels and macrophages as predictive biomarkers for nanomedicine tumor accumulation on biopsy samples and a comparison to the respective tissues from tumor resections. Replotted data of **Figure 14** of the assessment of blood vessels and macrophages in resected tumor tissues, normalized to 1 cm^2, as well as the % ID/kg tumor values of Harrington et al. (Harrington et al., 2001) **(a,b,c)** and the resulting CD31 and CD68 product score vs. the liposome accumulation **(d)**. For the patients of panel a and b, the corresponding biopsies were also cut and stained for CD31 and CD68 (due to the very different sizes of the biopsies, counts were normalized to 1 cm^2 **(e, f)**. CD31 and CD68 values were multiplied and means were plotted against the means of the tumor accumulation from panel c **(g)**. Statistical values are based on Student's *t*-test, and the error bars indicate the range of product scores and tumor accumulation values (y-axis: minima and maxima, x-axis: standard deviations). Adapted from (May et al., 2024).

As the investigated area was normalized on the tumor resection samples (due to five to six 2 mm punches that were stained), and due to the very different dimensions of biopsies (with especially lung, but also breast biopsies having way smaller areas than H&N biopsies, due to their different locations and different conduction methods), the data from Figure 14 c, d, and f were replotted and normalized to the area of 1 cm^2 (Figure 15 a, b, d). The quantification of the numbers of blood vessels and macrophages was comparable to the outcome on resected material, with breast cancers presenting with lower $CD31^+$ and $CD68^+$ counts compared to lung and H&N cancers (Figure 15 e, f). Again, breast cancer could be identified as the lowest liposome accumulating tumor entity

(Figure 15 g), which taken together encourages the application of histopathological biomarkers for patient stratification in chemotherapy-loaded nanomedicine therapies.

4.2 Optical imaging of nanomedicine delivery across the blood-brain barrier upon sonopermeation

Drug delivery to the CNS is challenging, due to the BBB carefully discriminating between molecules and substances that can enter the brain and those that barely leave blood vessels.[2] A targeted and reversible opening of the BBB can be induced by sonopermeation, which combines microbubbles and US, and allows the extravasation of drug molecules and drug delivery systems out of capillaries and their penetration into the brain. So far, it was barely studied if the sonopermeation-induced BBB opening has a size-dependent effect on the brain accumulation of nanomedicines. Using multimodal and multiscale optical imaging, fluorophore-labeled polymers and liposomes were monitored and their brain accumulation and penetration were evaluated.

4.2.1 Macroscopic optical imaging to visualize nanomedicine accumulation in the brain upon sonopermeation

To investigate a potential size-dependent effect of nanomedicines on their accumulation in and penetration into the brain upon sonopermeation-mediated BBB opening, two differently sized nanomedicines and several different optical imaging methods have been applied. Fluorophore-labeled PHPMA polymers (with a size of 10-20 nm, and labeled either with Atto 488 or Alexa-750) or liposomes (with a size of 100 nm, and labeled with Alexa-488 and Alexa-750) have been injected i.v. in healthy CD1 nude mice. After one hour, one half of the mice received both an i.v. infusion of PBCA microbubbles and were treated with ultrasound in parallel over 5 minutes (16 MHz,

[2] The results presented in subchapter 4.2 have been published in (May et al., 2020). Figures of the publication are presented upon adaption within this thesis, which is covered by the Creative Commons Attribution 4.0 International License (http://creativecommons.org/licenses/by/4.0/).

peak negative pressure of 1.8 MPa, mechanical index of 0.45). Longitudinal CT-FLT scans were performed 2, 4, and 24 h after the injection of the polymers or liposomes and after the last scan, the animals received a rhodamine lectin injection and were killed subsequently to mark perfused vessels for the ex vivo microscopy. Excised brains were imaged with FRI, standard fluorescence microscopy, confocal microscopy, and STED nanoscopy (Figure 16).

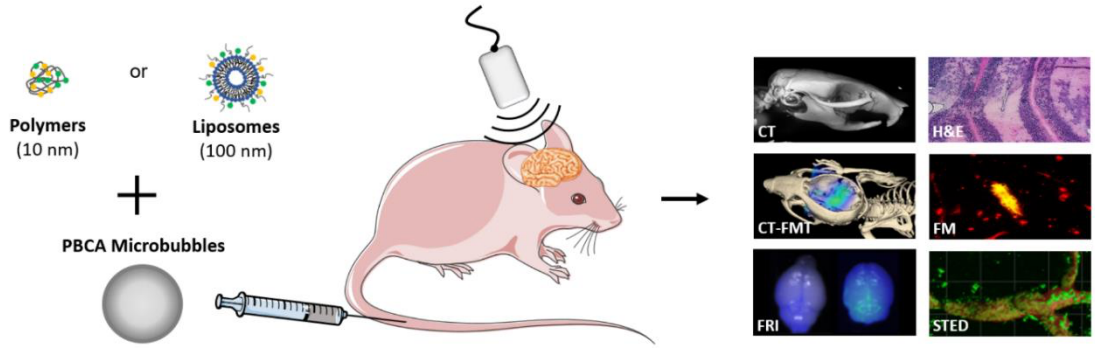

Figure 16: Study overview. The brain accumulation and extravasation of fluorophore-labeled PHPMA polyerms and PEGylated liposomes were evaluated upon PBCA-microbubbles- and ultrasound-induced BBB opening. Different optical imaging techniques covering the range from whole body imaging to individual capillaires were applied. Adapted from (May et al., 2020)

Hybrid CT-FLT was used to image the biodistribution and the total brain accumulation of fluorophore-labeled polymers and liposomes in control and sonopermeation-treated mice. In 3D reconstructed and segmented scans, there was a decent to strong signal of polymers and liposomes in the brains of both treatment groups (Figure 17 a, b). After 24 h, there was a significant difference between control and sonopermeation-treated animals which were injected with polymers (3.1 ± 0.3 vs. 5.1 ± 0.9 % ID per 500 mm^3, $p<0.01$, Figure 17 c). This difference could be confirmed in ex vivo FRI scans as well (Figure 17 d). For liposomes, there was no significant increase between control and sonopermeation-treated animals (2.2 ± 0.6 vs. 2.7 ± 0.8 % ID per 500 mm^3, $p>0.05$, Figure 17 e), comparable to the analysis of ex vivo FRI scans (Figure 17 f). The relatively high fluorescence levels of control brains reflect the long blood half-life of polymers and liposomes, which are still circulating.

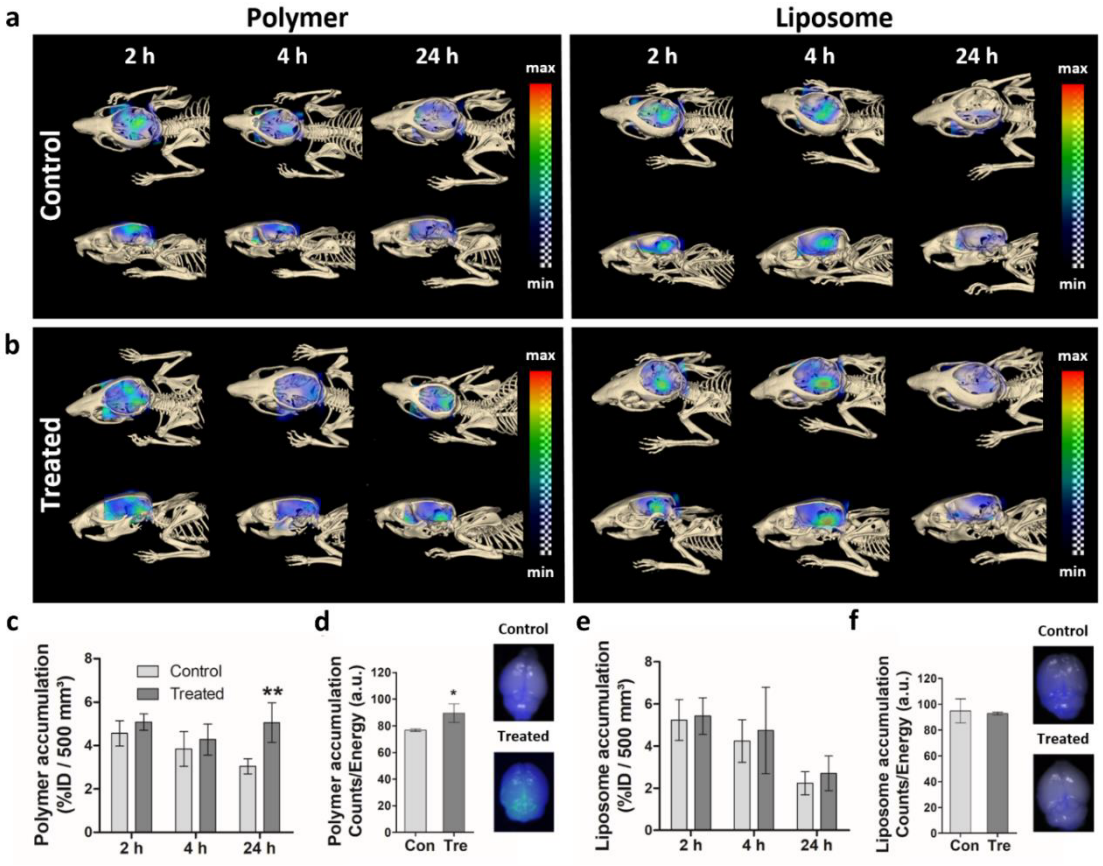

Figure 17: In vivo monitoring of the brain accumulatin of polymers and liposomes using longitudinal hybrid CT-FLT and ex vivo FRI imaging. Reconstructed CT-FLT scans 2, 4, and 24 h post injection of fluorophore-labeled polymers (10 nm) and liposomes (100 nm) in control and sonopermeation-applied animals, with an adaption of the cranial bone enabling a direct view on the brain **(a, b)**. Reconstructed CT-FLT scans were quantified and the polymer and liposome accumulation was plotted as the % ID per 500 mm³ **(c, e)**. Excised brains were analysed using FRI, and the measured fluorescence was plotted as counts/energy **(d, f)**. Statistical values are based on two-way ANOVA, with *p<0.05 and **p<0.01. Adapted from (May et al., 2020).

Based on the CT-FLT scans, it seemed that the sonopermeation-induced BBB opening facilitated an increased delivery of the smaller sized polymers into the brains. Due to the limitations in the resolution of FLT, single vessels can not be analyzed, and a direct proof of the extravasation of polymers or liposomes is hardly possible.

4.2.2 Evaluating safety and efficacy of sonopermeation-mediated BBB opening ex vivo

Depending on the applied settings, ultrasound alone and in combination with microbubbles can be quite destructive, leading to its use to e.g. destroy kidney stones or ablate tissues. Potential side effects of the sonopermeation-mediated BBB opening, such as extravasated erythrocytes, micro-hemorrhages, edema, or necrotic areas, have been therefore evaluated using H&E stainings (Figure 18 a). With the applied settings, there were no side effects or any damage to the brain and its vasculature detectable,

which was reflected in the observed, normal behavior of the mice upon sonopermeation.

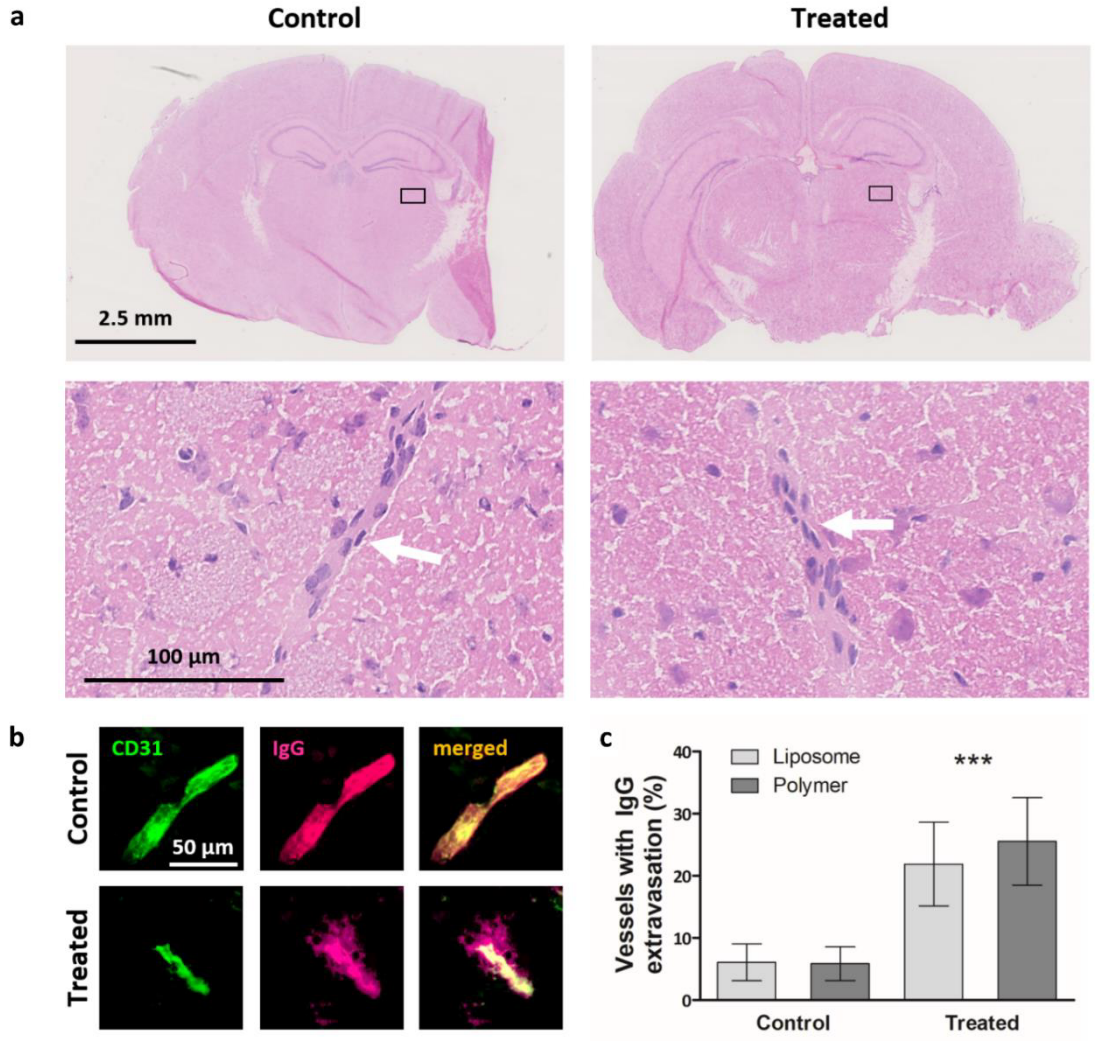

Figure 18: Evaluating the safety and proof of principle of sonopermeation-induced BBB opening. Excised brains were stained via H&E to assess tissue or vessel damage in treated brain slices compared to control. White arrows indicate clear blood vessel delineation, and no treatment-induced damage was detectable **(a)**. Stainings for IgG were conducted, using extravasated IgG as an endogenous nanoparticle indicating a successful opening of the BBB **(b)**. Blood vessels presenting with IgG extravasation were counted and compared between control and sonopermeation-treated animals **(c)**. Statistical significane was tested using Student's *t*-test, with ***<p0.001. Adapted from (May et al., 2020).

Furthermore, the success of the BBB opening was tested using stainings for IgG as an endogenous biomarker. In control mice, there was a significant lower percentage of vessels with extravasated IgG compared to sonopermeation-treated mice (6.0 ± 2.7 % vs. 23.7 ± 6.5 %, p<0.001, Figure 18 c) verifying the opening of the BBB, which was comparable high in the polymer and liposome group. The BBB opening was therefore tolerated well, successful and reproducible.

4.2.3 Two-dimensional quantification of the extravasation and penetration of polymers and liposomes using fluorescence microscopy

To investigate the extravasation and penetration of polymers and liposomes out of blood vessels into the brain, fluorescence microscopy images were acquired. In these images, only the extravasation of polymers upon sonopermeation was visible by eyeballing while extravasated polymers in control animals or extravasated liposomes were barely visible (Figure 19 a). The polymer and liposome signal was measured as the area fraction (in %), detecting significant differences between control and sonopermeation-treated animals in the polymer group, but no significant differences in the liposome group (1.5 ± 0.2 % vs. 2.1 ± 0.1 %, $p<0.05$, Figure 19 c, e). Counting of vessels showing extravasation of polymers or liposomes were in line with the area fraction results, with again no statistically significant difference between mice, that were injected with liposomes and treated either as a control or with sonopermeation - and with a significant difference in the polymer injected animals upon sonopermeation (0.6 ± 0.3 vs. 6.8 ± 0.5 vessels per field-of-view, $p<0.001$, Figure 19 d, f). The penetration depth of polymers and liposomes out of vessels into the brain was analyzed automatically by adapting a Definiens-based script. The script identified the vessel lumen and extended the vessel wall in steps of 5 µm by concentric rings, allowing the quantification of polymer and liposome signal per ring in and around blood vessels. For polymers, there was a significant difference in the signal distribution between control and sonopermeation-treated animals (Figure 19 g). The vast majority (92 ± 5 %) of polymer signal remained in the vessel lumen in control animals, while roughly 50% of the polymer signal was detected outside blood vessels in sonopermeation-treated animals (53 ± 5 %), leading to significant higher polymer levels in the 5, 10, 15, and 20 µm concentric rings. In contrast to polymers, liposomes were mostly located in blood vessels (94 ± 5 % in control animals, 86 ± 13 % for sonopermeation-treated animals, Figure 19 h). Within the concentric rings covering the area surrounding each vessel, there were slightly higher liposome signals detected, without reaching statistical significance (Figure 19 h).

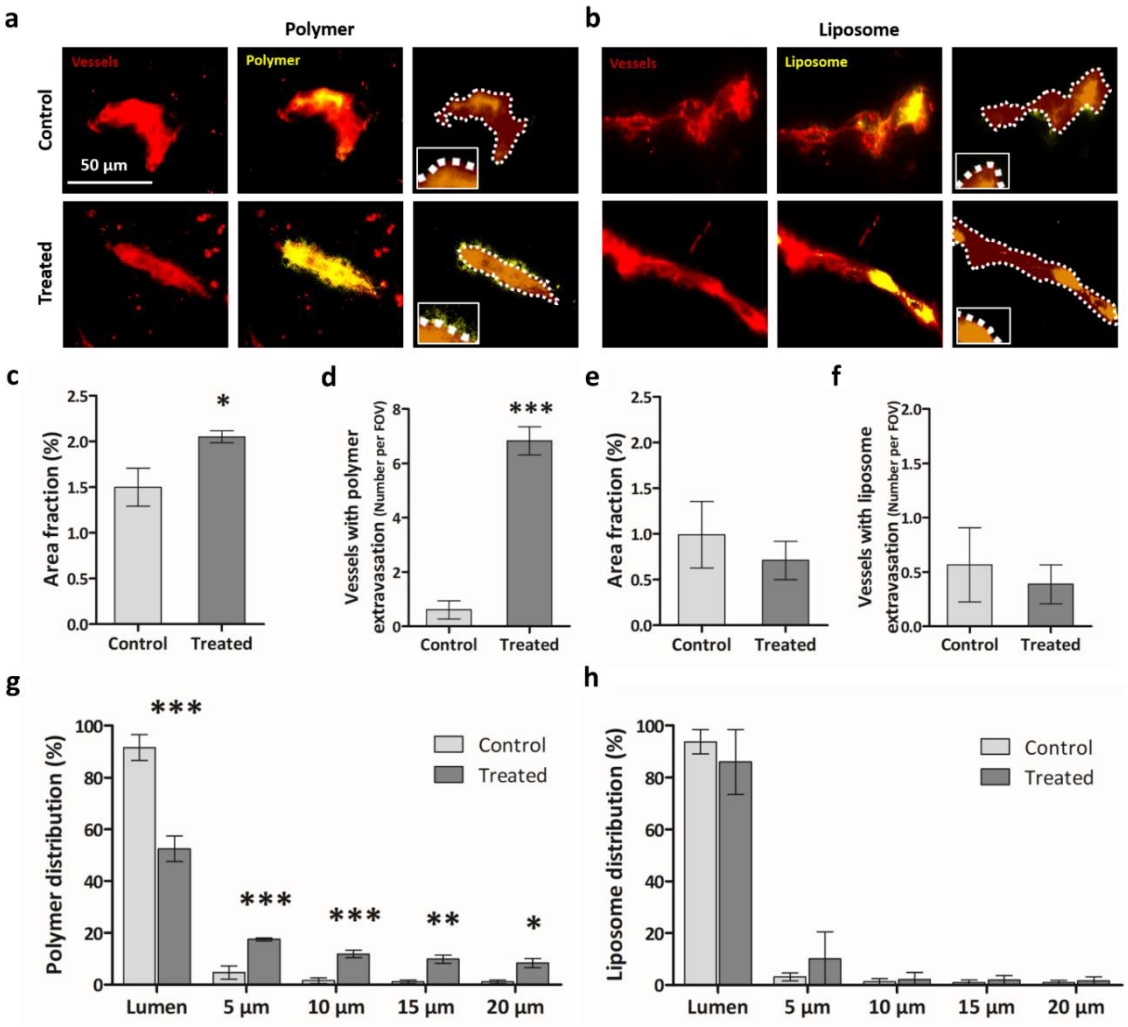

Figure 19: Analyzing brain accumulation, extravasation and penetration depth of polymers and liposomes upon sonopermeation-induced BBB opening with fluorescence microscopy. Rhodamine lectin-marked blood vessels as well as fluorophore-labeled polymers and liposomes were imaged, with white dotted lines delineating the vessels **(a, b)**. The area fraction of polymers and liposomes was analyzed and vessels presenting with polymer or liposome extravasation were counted **(c - f)**. Statistical significance was analyzed using Student's *t*-test, with *p<0.05 and ***p<0.001. Based on the vessel lumen, the distribution and penetration of polymers and liposomes was analyzed using concentric rings **(g, h)**. Statistical significance was tested using two-way ANOVA, with *p<0.05, **p<0.01, ***p<0.001. Adapted from (May et al., 2020).

These findings confirm the impression regarding the extravasation of polymers and liposomes in untreated animals as well as in their counterparts with an opening of the BBB, pointing towards a size-dependent effect of a nanomedicines on its capabilities to extravasate into the brain.

4.2.4 Visualizing the penetration of nanomedicines into the brain via confocal microscopy and STED nanoscopy upon sonopermeation

The two-dimensional evaluation of the distribution of polymers and liposomes based on fluorescence microscopy was extended by using confocal microscopy and STED nanoscopy, further enabling a three-dimensional imaging and analysis. Additionally, both confocal microscopy and especially STED nanoscopy provide a higher spatial resolution, with STED being able to image single liposomes. In line with the findings presented above, extravasated polymers were detected in sonopermeation-treated mice but not in control mice using confocal microscopy (Figure 20 a). For the first time, there were also findings of liposomes, that were able to extravasate out of blood vessels upon a sonopermeation-induced BBB opening (Figure 20 b). The quantification of the distribution of polymers and liposomes in relation to blood vessels was realized using a MATLAB-based script which extended the vessel surface in 5 µm steps, up to 25 µm. Upon sonopermeation, the penetration of polymers and liposomes into the brain was increased compared to control animals. In the case of polymers, the differences were significant, with 63.9 ± 3.1 % vs. 10.7 ± 8.8 % of the polymer signal stuck in the lumen for control vs. sonopermeation-treated animals, and significantly more polymer signal in the 10, 15, and 20 µm ring compared to control animals – with up to 7.0 ± 7.0 % of polymer signal in the 25 µm ring (Figure 20 c). Although there were no statistical significant differences detectable for liposomes upon sonopermeation, there was a noticeable trend of an increased penetration into the brain following the opening of the BBB (Figure 20 d), as e.g. 1.6 ± 2.8 % of the liposome signal was detected 15 – 20 µm deep into the brain. The images acquired by STED nanoscopy verified the presence of both extravasated polymers and liposomes upon the sonopermeation-induced BBB opening, and they confirmed a different pattern of distribution. Polymers were more spread throughout the tissue and penetrated deeper out of the blood vessels, while the liposomes were found in closer proximity to the endothelial vessel wall (Figure 20 e, f).

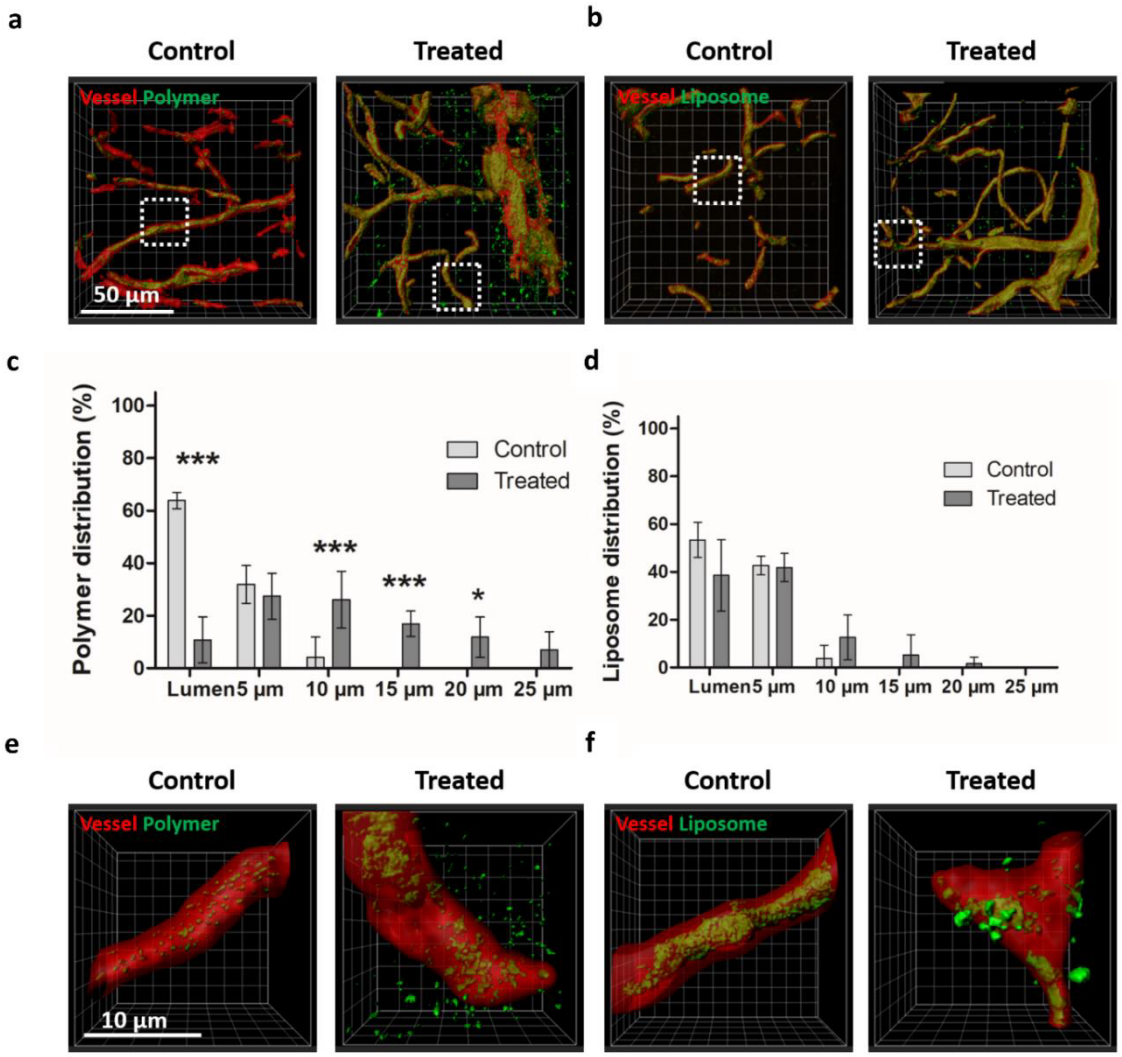

Figure 20: 3D visualization of polymer and liposome penetration into the brain after sonopermeation-induced BBB opening via conocal microscopy and STED nanoscopy. Using 25-40 µm thick brain sections, rhodamine lectin-marked as well as fluorophore-labeled polymers and liposomes were imaged via confocal microscopy, both in control and sonopermeation-treated mice **(a, b)**. The vessel surface was extended using concentric rings and the polymer and liposome signal was evaluated per ring, measuring penetration depth in relation to the vessel **(c, d)**. Statistical significance was tested using Student's *t*-test, with *p<0.05 and ***p<0.001. Via STED nanoscopy, the extravasation of polymers and liposomes was exemplarily visualized, using the optical imaging method with the highest resolution **(e, f)**. Adapted from (May et al., 2020).

The representative images shown in Figure 20 e and f were based on advanced image processing, with the applied steps consisting of a deconvolution, 3D rendering, and 3D smoothing (Figure 21 a-d). Raw data images can contain background noise as well as a shift of the signal, indicated by e.g. the vertical stretched dots in Figure 21 a. Rendering and smoothing the quite dotted signal of rhodamine lectin-marked blood vessels allowed the depiction of tube-like blood vessels.

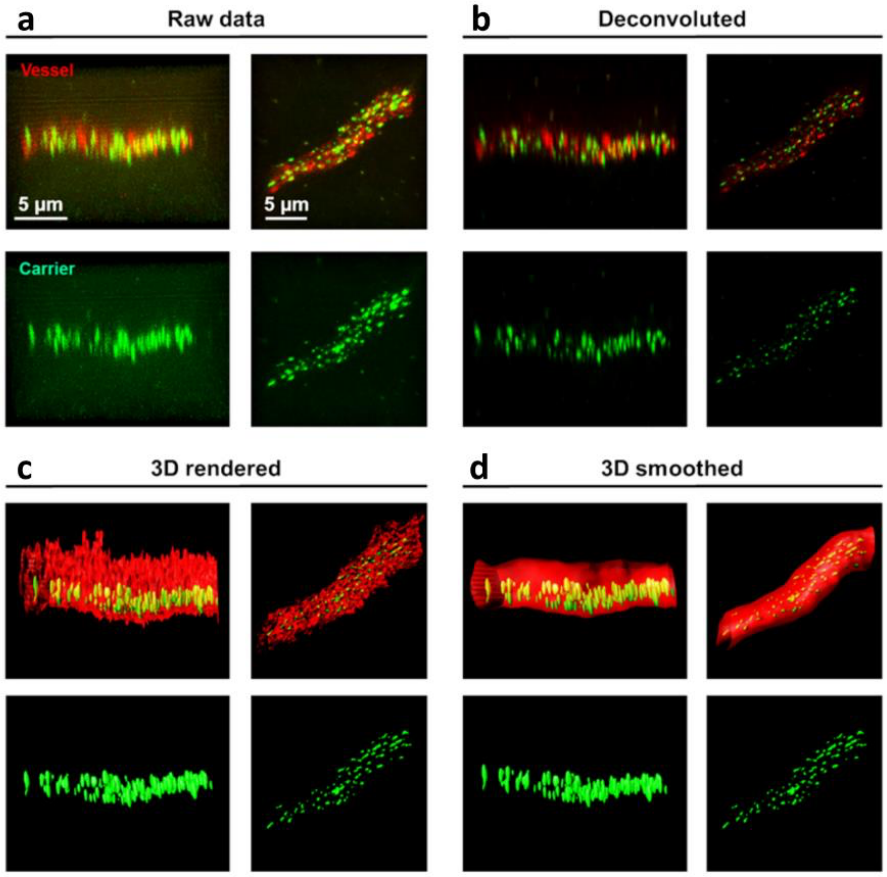

Figure 21: Reconstruction of STED images. Rhodamine-marked blood vessels and fluorophore-labeled polymers and liposomes were also imaged using STED nanoscopy. The workflow of the reconstruction is exemplarily shown here, starting with the raw images, which still contain background noise and shifted signal **(a)**. The background was automatically removed and a potential shift of the signal was automatically corrected using Huygens Professional software **(b)**. The resulting signal was 3D rendered **(c)** and 3D smoothed, resulting in representative blood vessel as well as polymer and liposome shapes **(d)**. Adapted from (May et al., 2020).

Taken together, the accumulation and penetration of fluorophore-labeled polymers and liposomes in the brain was compared between untreated control animals and animals receiving a BBB opening induced by sonopermeation. Employing several optical imaging techniques ranging from macroscopic hybrid µCT-FLT and FRI to the microscopic fluorescence and confocal microscopy and up to the nanoscopic STED revealed a size-dependent effect of nanomedicines on their capabilities to cross the (opened) BBB.

5 Discussion

5.1 Predicting the tumor accumulation of nanomedicines using histopathological biomarkers

Starting in murine tumor models, biomarkers based on histopathological stainings linked to the tumor accumulation of nanomedicines were identified. Validating blood vessels and macrophages as discriminative for low and high accumulating tumors in additional preclinical tumor models and on a historic cohort of patients motivates further research and the translation of easy implementable stratification measures for clinical trials of chemotherapeutic nanomedicines.

The tumor accumulation of fluorophore-labeled PHPMA was assessed in three murine tumor models (A431, MLS, and CT26) using optical hybrid µCT-FLT imaging. Next, the tumor microenvironment was characterized using 23 different features, which were linked to the polymer accumulation values. The whole data set was fed into a machine learning tool (GTB), and the importance of blood vessels and macrophages for the accumulation of nanomedicines was emphasized as being the most used features for the prediction. As blood vessels are required for delivering nutrients and nanomedicines into a tumor and macrophages contribute to the retention of nanomedicines in a tumor, this result is confirmed already by the direct correlations between blood vessels and macrophages with the tumor accumulation. Furthermore, the importance of blood vessels for biodistribution and tumor accumulation of nanomedicines is well known (Theek et al., 2014, Sulheim et al., 2018, Kingston et al., 2019, Moss et al., 2020). Macrophages, which take up nanomedicines, have as well a substantial impact on the retention, distribution, and even drug release of drug delivery systems in tumors (Miller et al., 2015b, Miller et al., 2015a, Lin et al., 2022, Strittmatter et al., 2022, Ngai et al., 2023). Focusing solely on stainings for blood vessels (CD31) and macrophages (F4/80), their capabilities in predicting the accumulation of nanomedicines (PHPMA as well as Doxil®-like liposomes) were validated in three immunocompetent murine tumor models as well as in a set of ten CDX and PDX tumor models. By introducing a product score based on an eyeballing assessment of blood vessels and macrophages in the already mentioned 10 CDX and PDX models, the low accumulating tumor models could be clearly distinguished from the high accumulating tumor models. One false negative,

E35CR, which presented with unexplainable high tumor accumulation while having low blood vessel and macrophage densities, was included, eventually resulting in a very good AUROC score (0.91).

These encouraging preclinical findings could not be verified in human patient samples at a head-to-head comparison, by staining biopsies or resected tumor tissue of patients with a known tumor accumulation of nanomedicines or by linking stainings with therapeutic outcomes such as progression-free survival. Instead, historical tumor accumulation values of a radiolabeled liposome which was injected in breast, lung, and H&N cancer patients were plotted against blood vessel and macrophage counts of patients whose biopsies and resected tumor material is stored in the archive of the Institute of Pathology of Uniklinik RWTH Aachen. Including ten patients per tumor type, the means of blood vessel and macrophage counts were able to differentiate between the lower accumulating breast cancer on the one hand and the higher accumulating lung and H&N cancers. In the future, it will be very interesting to test if the drug delivery of chemotherapy-loaded nanomedicines such as polymers, micelles or liposomes or antibody-drug conjugates into solid tumors can be predicted by the number of blood vessels and macrophages. When a sufficient (i.e. quite large) amount of patient samples is available, an attempt in combining H&E stainings and rather advanced machine learning tools to stratify patients in nanomedicine trials will also be very promising. Upon assessing the tumor microenvironment, suitable co-treatments such as normalizing the tumor vasculature, applying microbubbles and ultrasound to increase perfusion and permeation, or ECM-modulating agents could also be suggested. In addition to these delivery-focused methods, strategies to identify the right set of chemotherapeutic drugs for individual patients would be highly complementary and might increase tumor response rates. As shown in the antibody field, imaging of the tumor accumulation of radiolabeled antibodies is superior to immunochemistry stainings of the antigen expression and predictive for therapeutic responses (Bensch et al., 2018, Mortimer et al., 2022). However, it will be very challenging to offer these imaging interventions in addition to the already rather expensive treatment.

As in clinical trials of nanomedicine formulations a prediction of the tumor accumulation is barely included, the nanomedicine community is encouraged to take patient

stratification more into account, while keeping the balance of enrolling enough patients in a given period of time as well as excluding those patients who are unlikely to respond to the applied therapeutic regimen. Carefully designed clinical trials, with higher chances to succeed than the on-going attempts of rather heterogenous tumor types from patients who received already several different chemotherapeutics, potentially supported by nanomedicine-enhancing co-treatments, can enable the field to keep its momentum, which is now mainly based on the globally known mRNA vaccines COVID-19. On-going clinical trials are extending the application of RNA vaccines to different diseases such as cancer or amyloidosis, e.g. by combining personalized neoantigen vaccines with chemotherapy and immunotherapy for the treatment of pancreatic cancer or with immunotherapy for the treatment of melanoma (Rojas et al., 2023, Weber et al., 2024) – or by knocking down a single gene in hepatocytes for the treatment of transthyretin amyloidosis (Gillmore et al., 2021). Employing stratification approaches such as histopathologic biomarkers in clinical trials can first improve the approval and translation of new nanomedicines in the clinic while it second can at later stages allow a personalized therapy for tumor patients.

5.2 Sonopermeation-induced delivery of nanomedicines across the BBB analyzed via optical imaging

The combination of microbubbles and ultrasound can permeabilize the BBB, facilitating drug delivery into the brain, and enabling the usage of drug molecules and drug delivery systems that otherwise would not reach pathological sites protected by a functional BBB. As introduced above, a size-dependent effect of nanomedicines on their accumulation, penetration, and distribution in the brain upon a sonopermeation-induced BBB opening is more and more understood. Using macroscopic, in vivo hybrid µCT-FLT, the accumulation of fluorophore-labeled polymers (10-20 nm) and liposomes (100 nm) was monitored over 24 h and compared between control animals and sonopermeation-treated animals. Based on the µCT-FLT data, there was a first hint towards an increased accumulation of the smaller sized polymer upon BBB opening, which was not detectable for the larger sized liposomes. Fluorescence microscopy allowed a first characterization of the penetration of polymers and liposomes out of

blood vessels and into the brain, and strengthened the in vivo findings. Only in mice, which were treated with sonopermeation and injected with polymers, there was a significant extravasation of injected nanomedicines detectable. While confocal microscopy further verified the enhanced accumulation and penetration of polymers compared to liposomes, STED nanoscopy could capture liposomes, that clearly extravasated out of blood vessels. Apparently, the reversible opening of the BBB leads to different time windows allowing the extravasation of differently sized nanomedicines, favoring the smaller ones. On the one hand, this study generally highlights the benefit of imaging techniques with higher resolutions, while it on the other hand, also strengthens previous publications, reporting a size-dependent effect of nanomedicines on their tissue penetration.

If one only considers the size of a nanomedicine, the ideal range seems to be between 10 and 20 nm, as these formulations are large enough to avoid renal clearance while they possess ideal tissue penetration and distribution profiles. Accordingly, one of nature's best tissue penetrating proteins has a comparable size, which is IgG (15 nm). The here used PHPMA polymer is from a comparable size, with 10-20 nm in serum - however, it has a rather limited drug loading capacity of 2-5 drug molecules per polymer. In contrast, a single liposome can be loaded with more than 1000 drug molecules, indicating the need of identifying a balance between overcoming the BBB, penetrating into the brain, and delivering sufficient amounts of drug molecules. Another important parameter is the retention of a nanomedicine within the tumor tissue. Although the retention of polymers and liposomes has not been the focus of the here presented study, it is deemed logical that a delayed removal by the glymphatic system extends the therapeutic window of the whole sonopermeation-supported intervention. In this regard, actively targeted nanomedicines might be a measure to further increase the retention of extravasated drug delivery systems.

Advancements in therapeutic approaches can turn so far thought to be untreatable tumors into maybe even curable diseases, which was showcased by two publications of the groups of Michelle Monje and Nick Vitanza reporting the outcomes of two phase I trials. Using GD2-targeted CAR-T cells, the patients presented both with tumor regression and neurological improvement, with one DIPG patient having a complete

response for at least 30 months (Monje et al., 2024). Vitanza et al. reported comparable promising results, with 3 patients with no progression upon treatment with B7-H3 CAR T cells for over 40 months (Vitanza et al., 2025). Within the field of nanomedicine and sonopermeation, comparable outcomes might be achievable as well, if e.g. the ultrasound devices are further optimized (on-going research aims for an MRI-independent setup) or if drug delivery systems are further tailored, with different drugs encapsulated or combined (Dasgupta et al., submitted). In this regard, it should be promising to shift the focus from delivering chemotherapeutic agents to modulating the tumor microenvironment or the immune system, to either prepare the ground for a chemotherapeutic treatment or to enable the body's own weaponry to fight against a tumor.

Taken together, the size-dependent effect of nanomedicines on their capability to cross an opened BBB could be verified. In general, brain-targeted formulations can benefit from a smaller size. However, one still has to keep in mind that in on-going clinical trials focusing on sonopermeation-facilitated drug delivery, standard chemotherapeutic drugs or traditional nanomedicines such as Doxil® are investigated, and not nanomedicines specifically designed for CNS delivery, loaded with tailored drugs or even drug combinations. The community is inducing discussions to improve the preclinical work on nanomedicines as well as the processes underlying clinical translation (Faria et al., 2018, Joyce et al., 2024). Combined with the stratification of patients, and motivated by the success of mRNA vaccines, the future for successful therapies based on nanomedicines has barely been brighter.

6 Summary: Optical imaging and immunohistological biomarkers to overcome obstacles in nanomedicine drug delivery to tumors and to the brain, by Jan-Niklas May

Optical imaging and immunohistological biomarkers to overcome obstacles in nanomedicine drug delivery to tumors and to the brain, by Jan-Niklas May

Within this doctoral thesis, an easy implementable and broadly available method was developed to predict the accumulation of nanomedicines in tumors. By immunohistological staining of biopsies and quantifying blood vessels and macrophages, it is possible to differentiate tumors with regard to their nanomedicine accumulation, which has the potential to be used cost-effectively in clinical trials as an inclusion vs. exclusion criterion. To this end, suitable biomarkers were first investigated in preclinical tumor models and a duo was identified with blood vessels and macrophages, which was subsequently validated both in preclinical tumor models and on patient material - both from resections and biopsies.

Additionally, optical imaging modalities were used to investigate the transport of fluorescently labeled nanocarriers into the brain of healthy mice. The extent to which the opening of the blood-brain barrier with ultrasound and microbubbles enables the extravasation of the drug delivery systems from the blood vessels into the brain was compared. Using micro- and nanoscopy, a size-dependent effect was demonstrated, as the smaller polymeric nanocarrier (10-20 nm) extravasated more frequently and more deeply from the blood vessels than the larger liposomes (100-120 nm). When developing nanomedicines for the treatment of diseases of the central nervous system, the size should therefore also be taken into account, whereby the balance between optimal distribution in the brain tissue and sufficient drug loading should be maintained.

The clinical translation of nanomedicines could be more successful. By implementing pragmatic protocols for stratifying patients or using methods for opening the blood-brain barrier, a higher accumulation of nanomedicinal drug carriers in (brain) tumor tissue can be made possible and therapies improved.

7 Zusammenfassung: Optische Bildgebung und immunhistologische Biomarker zur Überwindung von Hindernissen im Wirkstofftransport von Nanomedizin in Tumoren und in das Gehirn, von Jan-Niklas May

In dieser Doktorarbeit wurde eine einfach anwendbare und allgemein verfügbare Methode entwickelt, mit der die Akkumulation von nanomedizinischen Wirkstoffträgern in Tumoren vorhergesagt werden kann. Durch immunohistologische Färbungen von Biopsien und dem Quantifizieren von Blutgefäßen und Makrophagen ist es möglich, Tumoren hinsichtlich ihrer Nanomedizinakkumulation zu unterscheiden, was das Potential hat, kostengünstig in klinischen Studien als Ein- bzw. Ausschlusskriterium genutzt werden kann. Dazu wurden zuerst in präklinischen Tumormodellen geeignete Biomarker untersucht und mit Blutgefäßen und Makrophagen ein Duo identifiziert, was im weiteren Verlauf sowohl in präklinischen Tumormodellen als auch auf Patientenmaterial - sowohl von Resektionen als auch von Biopsien - validiert wurde.

Zudem wurden optische Bildgebungsmodalitäten genutzt, um den Transport fluoreszent markierter nanomedizinischer Wirkstoffträger in das Gehirn gesunder Mäuse zu untersuchen. Dabei wurde verglichen, in wie weit eine Öffnung der Blut-Hirn-Schranke mit Ultraschall und Mikrobläschen die Extravasation der Wirkstoffträger aus den Blutgefäßen in das Hirn möglich macht. Mittels Mikro- und Nanoskopie konnte ein größenabhängiger Effekt nachgewiesen werden, da kleinere, polymere Wirkstoffträger (10-20 nm) häufiger und tiefer aus den Blutgefäßen extravasierten als die größeren Liposomen (100-120 nm). Bei der Entwicklung nanomedizinischer Wirkstoffträger zur Behandlung von Erkrankungen des zentralen Nervensystems sollte somit auch die Größe berücksichtigt werden, wobei hier die Balance zwischen optimaler Verteilung in das Hirngewebe und ausreichender Wirkstoffbeladung gewahrt werden sollte.

Die klinische Translation nanomedizinischer Wirkstoffträger könnte erfolgreicher verlaufen. Durch das Implementieren pragmatischer Protokolle zur Patientenstratifizierung oder das Anwenden von Methoden zur Öffnung der Blut-Hirn-Schranke kann dabei eine höhere Akkumulation nanomedizinischer Wirkstoffträger in dem (Hirn-)Tumorgewebe ermöglicht und Therapien verbessert werden.

8 References

ABRAHAO, A., MENG, Y., LLINAS, M., HUANG, Y., HAMANI, C., MAINPRIZE, T., AUBERT, I., HEYN, C., BLACK, S. E. & HYNYNEN, K. 2019. First-in-human trial of blood–brain barrier opening in amyotrophic lateral sclerosis using MR-guided focused ultrasound. *Nature communications,* 10**,** 4373.

ANSELMO, A. C. & MITRAGOTRI, S. 2021. Nanoparticles in the clinic: An update post COVID-19 vaccines. *Bioengineering & translational medicine,* 6**,** e10246.

ARAP, W., KOLONIN, M. G., TREPEL, M., LAHDENRANTA, J., CARDÓ-VILA, M., GIORDANO, R. J., MINTZ, P. J., ARDELT, P. U., YAO, V. J. & VIDAL, C. I. 2002. Steps toward mapping the human vasculature by phage display. *Nature medicine,* 8**,** 121-127.

ARCAMONE, F., CASSINELLI, G., FANTINI, G., GREIN, A., OREZZI, P., POL, C. & SPALLA, C. 1969. Adriamycin, 14-hydroxydaimomycin, a new antitumor antibiotic from S. Peucetius var. caesius. *Biotechnology and bioengineering,* 11**,** 1101-1110.

ARYAL, M., ARVANITIS, C. D., ALEXANDER, P. M. & MCDANNOLD, N. 2014. Ultrasound-mediated blood–brain barrier disruption for targeted drug delivery in the central nervous system. *Advanced drug delivery reviews,* 72**,** 94-109.

BAIER, J., RIX, A., DARGUZYTE, M., GIRBIG, R. M., MAY, J.-N., PALME, R., TOLBA, R. & KIESSLING, F. 2023. Repeated contrast-enhanced micro-CT examinations decrease animal welfare and influence tumor physiology. *Investigative Radiology,* 58**,** 327-336.

BAIER, J., RIX, A., DRUDE, N. I., DARGUZYTE, M., BAUES, M., MAY, J.-N., SCHIPPER, S., MÖCKEL, D., PALME, R. & TOLBA, R. 2020. Influence of MRI examinations on animal welfare and study results. *Investigative Radiology,* 55**,** 507-514.

BANKHEAD, P., LOUGHREY, M. B., FERNÁNDEZ, J. A., DOMBROWSKI, Y., MCART, D. G., DUNNE, P. D., MCQUAID, S., GRAY, R. T., MURRAY, L. J. & COLEMAN, H. G. 2017. QuPath: Open source software for digital pathology image analysis. *Scientific reports,* 7**,** 1-7.

BECKER, S., MOMOH, J., BIANCACCI, I., MÖCKEL, D., WANG, Q., MAY, J. N., SU, H., CANDELS, L. S., BERRES, M. L. & KIESSLING, F. 2023. Intermittent Fasting Primes the Tumor Microenvironment And Improves Nanomedicine Delivery In Hepatocellular Carcinoma. *Small,* 19**,** 2208042.

BENSCH, F., VAN DER VEEN, E. L., LUB-DE HOOGE, M. N., JORRITSMA-SMIT, A., BOELLAARD, R., KOK, I. C., OOSTING, S. F., SCHRÖDER, C. P., HILTERMANN, T. J. N. & VAN DER WEKKEN, A. J. 2018. 89Zr-atezolizumab imaging as a non-invasive approach to assess clinical response to PD-L1 blockade in cancer. *Nature medicine,* 24**,** 1852-1858.

BIANCACCI, I., DE LORENZI, F., THEEK, B., BAI, X., MAY, J. N., CONSOLINO, L., BAUES, M., MOECKEL, D., GREMSE, F. & VON STILLFRIED, S. 2022. Monitoring EPR effect dynamics during nanotaxane treatment with theranostic polymeric micelles. *Advanced science,* 9**,** 2103745.

BOIRE, A., BURKE, K., COX, T. R., GUISE, T., JAMAL-HANJANI, M., JANOWITZ, T., KAPLAN, R., LEE, R., SWANTON, C. & VANDER HEIDEN, M. G. 2024. Why do patients with cancer die? *Nature Reviews Cancer***,** 1-12.

BOUCHER, Y., BAXTER, L. T. & JAIN, R. K. 1990. Interstitial pressure gradients in tissue-isolated and subcutaneous tumors: implications for therapy. *Cancer research,* 50**,** 4478-4484.

BYRNE, J. D., BETANCOURT, T. & BRANNON-PEPPAS, L. 2008. Active targeting schemes for nanoparticle systems in cancer therapeutics. *Advanced drug delivery reviews,* 60**,** 1615-1626.

CABRAL, H., MATSUMOTO, Y., MIZUNO, K., CHEN, Q., MURAKAMI, M., KIMURA, M., TERADA, Y., KANO, M. R., MIYAZONO, K., UESAKA, M., NISHIYAMA, N. & KATAOKA, K. 2011. Accumulation of sub-100 nm polymeric micelles in poorly permeable tumours depends on size. *Nature Nanotechnology,* 6**,** 815-823.

CARMELIET, P. & JAIN, R. K. 2000. Angiogenesis in cancer and other diseases. *nature,* 407**,** 249-257.

CARPENTIER, A., CANNEY, M., VIGNOT, A., REINA, V., BECCARIA, K., HORODYCKID, C., KARACHI, C., LECLERCQ, D., LAFON, C. & CHAPELON, J.-Y. 2016. Clinical trial of blood-brain barrier disruption by pulsed ultrasound. *Science translational medicine,* 8**,** 343re2-343re2.

CUCCARESE, M. F., DUBACH, J. M., PFIRSCHKE, C., ENGBLOM, C., GARRIS, C., MILLER, M. A., PITTET, M. J. & WEISSLEDER, R. 2017. Heterogeneity of macrophage infiltration and therapeutic response in lung carcinoma revealed by 3D organ imaging. *Nature communications,* 8**,** 14293.

DANHIER, F. 2016. To exploit the tumor microenvironment: Since the EPR effect fails in the clinic, what is the future of nanomedicine? *Journal of Controlled Release,* 244**,** 108-121.

DEPREZ, J., LAJOINIE, G., ENGELEN, Y., DE SMEDT, S. & LENTACKER, I. 2021. Opening doors with ultrasound and microbubbles: Beating biological barriers to promote drug delivery. *Advanced drug delivery reviews,* 172**,** 9-36.

DILLEKÅS, H., ROGERS, M. S. & STRAUME, O. 2019. Are 90% of deaths from cancer caused by metastases? *Cancer medicine,* 8**,** 5574-5576.

DIMCEVSKI, G., KOTOPOULIS, S., BJÅNES, T., HOEM, D., SCHJØTT, J., GJERTSEN, B. T., BIERMANN, M., MOLVEN, A., SORBYE, H. & MCCORMACK, E. 2016. A human clinical trial using ultrasound and microbubbles to enhance gemcitabine treatment of inoperable pancreatic cancer. *Journal of Controlled Release,* 243**,** 172-181.

DOANE, T. L. & BURDA, C. 2012. The unique role of nanoparticles in nanomedicine: imaging, drug delivery and therapy. *Chemical Society Reviews,* 41**,** 2885-2911.

DOI, T., SHITARA, K., NAITO, Y., SHIMOMURA, A., FUJIWARA, Y., YONEMORI, K., SHIMIZU, C., SHIMOI, T., KUBOKI, Y. & MATSUBARA, N. 2017. Safety, pharmacokinetics, and antitumour activity of trastuzumab deruxtecan (DS-8201), a HER2-targeting antibody–drug conjugate, in patients with advanced breast and gastric or gastro-oesophageal tumours: a phase 1 dose-escalation study. *The Lancet Oncology,* 18**,** 1512-1522.

DRAGO, J. Z., MODI, S. & CHANDARLAPATY, S. 2021. Unlocking the potential of antibody–drug conjugates for cancer therapy. *Nature Reviews Clinical Oncology,* 18**,** 327-344.

DVORAK, H. F., NAGY, J. A., DVORAK, J. & DVORAK, A. 1988. Identification and characterization of the blood vessels of solid tumors that are leaky to circulating macromolecules. *The American journal of pathology,* 133**,** 95.

EHRLICH, P. 1907. THE HARBEN LECTURES, 1907. EXPERIMENTAL RESEARCHES ON SPECIFIC THERAPEUTICS. *Journal of the Royal Institute of Public Health,* 15**,** 321-340.

ERGEN, C., HEYMANN, F., GREMSE, F., BARTNECK, M., PANZER, U., POLA, R., PECHAR, M., STORM, G., MOHR, N. & BARZ, M. 2017. Targeting distinct myeloid cell populations in vivo using polymers, liposomes and microbubbles. *Biomaterials,* 114**,** 106-120.

ERGEN, C., NIEMIETZ, P. M., HEYMANN, F., BAUES, M., GREMSE, F., POLA, R., VAN BLOOIS, L., STORM, G., KIESSLING, F. & TRAUTWEIN, C. 2019. Liver fibrosis affects the targeting properties of drug delivery systems to macrophage subsets in vivo. *Biomaterials,* 206**,** 49-60.

ESPELIN, C. W., LEONARD, S. C., GERETTI, E., WICKHAM, T. J. & HENDRIKS, B. S. 2016. Dual HER2 targeting with trastuzumab and liposomal-encapsulated doxorubicin (MM-302) demonstrates synergistic antitumor activity in breast and gastric cancer. *Cancer research,* 76**,** 1517-1527.

ETRYCH, T., MRKVAN, T., ŘÍHOVÁ, B. & ULBRICH, K. 2007. Star-shaped immunoglobulin-containing HPMA-based conjugates with doxorubicin for cancer therapy. *Journal of controlled release,* 122**,** 31-38.

FARIA, M., BJÖRNMALM, M., THURECHT, K. J., KENT, S. J., PARTON, R. G., KAVALLARIS, M., JOHNSTON, A. P., GOODING, J. J., CORRIE, S. R. & BOYD, B. J. 2018. Minimum information reporting in bio–nano experimental literature. *Nature nanotechnology,* 13**,** 777-785.

FERRARA, K., POLLARD, R. & BORDEN, M. 2007. Ultrasound microbubble contrast agents: fundamentals and application to gene and drug delivery. *Annu. Rev. Biomed. Eng.,* 9**,** 415-447.

FOKONG, S., SIEPMANN, M., LIU, Z., SCHMITZ, G., KIESSLING, F. & GÄTJENS, J. 2011. Advanced characterization and refinement of poly N-butyl cyanoacrylate microbubbles for ultrasound imaging. *Ultrasound in medicine & biology,* 37**,** 1622-1634.

FOLKMAN, J. 1971. Tumor angiogenesis: therapeutic implications. *N Engl j Med,* 285**,** 1182-1186.

GABIZON, A., CATANE, R., UZIELY, B., KAUFMAN, B., SAFRA, T., COHEN, R., MARTIN, F., HUANG, A. & BARENHOLZ, Y. 1994. Prolonged circulation time and enhanced accumulation in malignant exudates of doxorubicin encapsulated in polyethylene-glycol coated liposomes. *Cancer research,* 54**,** 987-992.

GABIZON, A., GOREN, D., HOROWITZ, A. T., TZEMACH, D., LOSSOS, A. & SIEGAL, T. 1997. Long-circulating liposomes for drug delivery in cancer therapy: a review of biodistribution studies in tumor-bearing animals. *Advanced Drug Delivery Reviews,* 24**,** 337-344.

GASCA-SALAS, C., FERNÁNDEZ-RODRÍGUEZ, B., PINEDA-PARDO, J. A., RODRÍGUEZ-ROJAS, R., OBESO, I., HERNÁNDEZ-FERNÁNDEZ, F., DEL ÁLAMO, M., MATA, D., GUIDA, P. & ORDÁS-BANDERA, C. 2021. Blood-brain barrier opening with focused ultrasound in Parkinson's disease dementia. *Nature communications,* 12**,** 779.

GILLMORE, J. D., GANE, E., TAUBEL, J., KAO, J., FONTANA, M., MAITLAND, M. L., SEITZER, J., O'CONNELL, D., WALSH, K. R. & WOOD, K. 2021. CRISPR-Cas9 in vivo gene editing for transthyretin amyloidosis. *New England Journal of Medicine,* 385**,** 493-502.

GIRISH, S., GUPTA, M., WANG, B., LU, D., KROP, I. E., VOGEL, C. L., BURRIS III, H. A., LORUSSO, P. M., YI, J.-H. & SAAD, O. 2012. Clinical pharmacology of trastuzumab emtansine (T-DM1): an antibody–drug conjugate in development for the

treatment of HER2-positive cancer. *Cancer chemotherapy and pharmacology,* 69**,** 1229-1240.

GOLOMBEK, S. K., MAY, J.-N., THEEK, B., APPOLD, L., DRUDE, N., KIESSLING, F. & LAMMERS, T. 2018. Tumor targeting via EPR: Strategies to enhance patient responses. *Advanced drug delivery reviews,* 130**,** 17-38.

GREMSE, F., DOLESCHEL, D., ZAFARNIA, S., BABLER, A., JAHNEN-DECHENT, W., LAMMERS, T., LEDERLE, W. & KIESSLING, F. 2015. Hybrid µCT-FMT imaging and image analysis. *JoVE (Journal of Visualized Experiments)***,** e52770.

GREMSE, F., STÄRK, M., EHLING, J., MENZEL, J. R., LAMMERS, T. & KIESSLING, F. 2016. Imalytics preclinical: interactive analysis of biomedical volume data. *Theranostics,* 6**,** 328.

GRIFFON-ETIENNE, G., BOUCHER, Y., BREKKEN, C., SUIT, H. D. & JAIN, R. K. 1999. Taxane-induced apoptosis decompresses blood vessels and lowers interstitial fluid pressure in solid tumors: clinical implications. *Cancer research,* 59**,** 3776-3782.

GU, X., SONG, Q., ZHANG, Q., HUANG, M., ZHENG, M., CHEN, J., WEI, D., CHEN, J., WEI, X. & CHEN, H. 2020. Clearance of two organic nanoparticles from the brain via the paravascular pathway. *Journal of Controlled Release,* 322**,** 31-41.

HAMILTON, A., BIGANZOLI, L., COLEMAN, R., MAURIAC, L., HENNEBERT, P., AWADA, A., NOOIJ, M., BEEX, L., PICCART, M. & VAN HOOREBEECK, I. 2002. EORTC 10968: a phase I clinical and pharmacokinetic study of polyethylene glycol liposomal doxorubicin (Caelyx®, Doxil®) at a 6-week interval in patients with metastatic breast cancer. *Annals of oncology,* 13**,** 910-918.

HANAHAN, D. & WEINBERG, R. A. 2000. The hallmarks of cancer. *cell,* 100**,** 57-70.

HARK, C., CHEN, J., BLÖCK, J., BUHL, E. M., RADERMACHER, H., POLA, R., PECHAR, M., ETRYCH, T., PEÑA, Q. & RIX, A. 2024. RGD-coated polymeric microbubbles promote ultrasound-mediated drug delivery in an inflamed endothelium-pericyte co-culture model of the blood-brain barrier. *Drug Delivery and Translational Research***,** 1-13.

HARRINGTON, K. J., MOHAMMADTAGHI, S., USTER, P. S., GLASS, D., PETERS, A. M., VILE, R. G. & STEWART, J. S. W. 2001. Effective targeting of solid tumors in patients with locally advanced cancers by radiolabeled pegylated liposomes. *Clinical Cancer Research,* 7**,** 243-254.

HASHIZUME, H., BALUK, P., MORIKAWA, S., MCLEAN, J. W., THURSTON, G., ROBERGE, S., JAIN, R. K. & MCDONALD, D. M. 2000. Openings between defective endothelial cells explain tumor vessel leakiness. *The American journal of pathology,* 156**,** 1363-1380.

HE, H., LIU, L., MORIN, E. E., LIU, M. & SCHWENDEMAN, A. 2019. Survey of clinical translation of cancer nanomedicines—lessons learned from successes and failures. *Accounts of chemical research,* 52**,** 2445-2461.

HRKACH, J., VON HOFF, D., ALI, M. M., ANDRIANOVA, E., AUER, J., CAMPBELL, T., DE WITT, D., FIGA, M., FIGUEIREDO, M. & HORHOTA, A. 2012. Preclinical development and clinical translation of a PSMA-targeted docetaxel nanoparticle with a differentiated pharmacological profile. *Science translational medicine,* 4**,** 128ra39-128ra39.

HURWITZ, H., FEHRENBACHER, L., NOVOTNY, W., CARTWRIGHT, T., HAINSWORTH, J., HEIM, W., BERLIN, J., BARON, A., GRIFFING, S. & HOLMGREN, E. 2004. Bevacizumab plus irinotecan, fluorouracil, and leucovorin for metastatic colorectal cancer. *New England journal of medicine,* 350**,** 2335-2342.

HYNYNEN, K., MCDANNOLD, N., VYKHODTSEVA, N. & JOLESZ, F. A. 2001. Noninvasive MR imaging–guided focal opening of the blood-brain barrier in rabbits. *Radiology,* 220**,** 640-646.

JACOBS, T. W., GOWN, A. M., YAZIJI, H., BARNES, M. J. & SCHNITT, S. J. 1999. Specificity of Hercep Test in determining HER-2/neu status of breast cancers using the United States Food and Drug Administration-approved scoring system. *Journal of Clinical Oncology,* 17**,** 1983-1987.

JAIN, R. K. 2005. Normalization of tumor vasculature: an emerging concept in antiangiogenic therapy. *Science,* 307**,** 58-62.

JOYCE, P., ALLEN, C. J., ALONSO, M. J., ASHFORD, M., BRADBURY, M. S., GERMAIN, M., KAVALLARIS, M., LANGER, R., LAMMERS, T. & PERACCHIA, M. T. 2024. A translational framework to DELIVER nanomedicines to the clinic. *Nature Nanotechnology*, 1-15.

KIESSLING, F., FOKONG, S., KOCZERA, P., LEDERLE, W. & LAMMERS, T. 2012. Ultrasound microbubbles for molecular diagnosis, therapy, and theranostics. *Journal of nuclear medicine,* 53, 345-348.

KINGSTON, B. R., LIN, Z. P., OUYANG, B., MACMILLAN, P., NGAI, J., SYED, A. M., SINDHWANI, S. & CHAN, W. C. 2021. Specific endothelial cells govern nanoparticle entry into solid tumors. *ACS nano,* 15, 14080-14094.

KINGSTON, B. R., SYED, A. M., NGAI, J., SINDHWANI, S. & CHAN, W. C. 2019. Assessing micrometastases as a target for nanoparticles using 3D microscopy and machine learning. *Proceedings of the National Academy of Sciences,* 116, 14937-14946.

KOOIMAN, K., VOS, H. J., VERSLUIS, M. & DE JONG, N. 2014. Acoustic behavior of microbubbles and implications for drug delivery. *Advanced drug delivery reviews,* 72, 28-48.

LAMMERS, T., PESCHKE, P., KÜHNLEIN, R., SUBR, V., ULBRICH, K., DEBUS, J., HUBER, P., HENNINK, W. & STORM, G. 2007. Effect of radiotherapy and hyperthermia on the tumor accumulation of HPMA copolymer-based drug delivery systems. *Journal of controlled release,* 117, 333-341.

LEE, H., GADDY, D., VENTURA, M., BERNARDS, N., DE SOUZA, R., KIRPOTIN, D., WICKHAM, T., FITZGERALD, J., ZHENG, J. & HENDRIKS, B. S. 2018. Companion diagnostic 64Cu-liposome positron emission tomography enables characterization of drug delivery to tumors and predicts response to cancer nanomedicines. *Theranostics,* 8, 2300.

LEE, H., SHIELDS, A. F., SIEGEL, B. A., MILLER, K. D., KROP, I., MA, C. X., LORUSSO, P. M., MUNSTER, P. N., CAMPBELL, K. & GADDY, D. F. 2017. 64Cu-MM-302 positron emission tomography quantifies variability of enhanced permeability and

retention of nanoparticles in relation to treatment response in patients with metastatic breast cancer. *Clinical Cancer Research,* 23**,** 4190-4202.

LEWIS PHILLIPS, G. D., LI, G., DUGGER, D. L., CROCKER, L. M., PARSONS, K. L., MAI, E., BLATTLER, W. A., LAMBERT, J. M., CHARI, R. V. & LUTZ, R. J. 2008. Targeting HER2-positive breast cancer with trastuzumab-DM1, an antibody–cytotoxic drug conjugate. *Cancer research,* 68**,** 9280-9290.

LIN, Z. P., NGUYEN, L. N., OUYANG, B., MACMILLAN, P., NGAI, J., KINGSTON, B. R., MLADJENOVIC, S. M. & CHAN, W. C. 2022. Macrophages actively transport nanoparticles in tumors after extravasation. *ACS nano,* 16**,** 6080-6092.

LIPSMAN, N., MENG, Y., BETHUNE, A. J., HUANG, Y., LAM, B., MASELLIS, M., HERRMANN, N., HEYN, C., AUBERT, I., BOUTET, A., SMITH, G. S., HYNYNEN, K. & BLACK, S. E. 2018. Blood–brain barrier opening in Alzheimer's disease using MR-guided focused ultrasound. *Nature Communications,* 9**,** 2336.

MAEDA, H., WU, J., SAWA, T., MATSUMURA, Y. & HORI, K. 2000. Tumor vascular permeability and the EPR effect in macromolecular therapeutics: a review. *Journal of controlled release,* 65**,** 271-284.

MAINPRIZE, T., LIPSMAN, N., HUANG, Y., MENG, Y., BETHUNE, A., IRONSIDE, S., HEYN, C., ALKINS, R., TRUDEAU, M. & SAHGAL, A. 2019. Blood-brain barrier opening in primary brain tumors with non-invasive MR-guided focused ultrasound: a clinical safety and feasibility study. *Scientific reports,* 9**,** 321.

MATSUMOTO, Y., NICHOLS, J. W., TOH, K., NOMOTO, T., CABRAL, H., MIURA, Y., CHRISTIE, R. J., YAMADA, N., OGURA, T. & KANO, M. R. 2016. Vascular bursts enhance permeability of tumour blood vessels and improve nanoparticle delivery. *Nature nanotechnology,* 11**,** 533-538.

MATSUMURA, Y. & MAEDA, H. 1986. A new concept for macromolecular therapeutics in cancer chemotherapy: mechanism of tumoritropic accumulation of proteins and the antitumor agent smancs. *Cancer research,* 46**,** 6387-6392.

MAY, J.-N., GOLOMBEK, S. K., BAUES, M., DASGUPTA, A., DRUDE, N., RIX, A., ROMMEL, D., VON STILLFRIED, S., APPOLD, L., POLA, R., PECHAR, M., VAN BLOOIS, L., STORM, G., KUEHNE, A. J. C., GREMSE, F., THEEK, B., KIESSLING, F. & LAMMERS, T. 2020. Multimodal and multiscale optical imaging of nanomedicine delivery across the blood-brain barrier upon sonopermeation. *Theranostics,* 10**,** 1948.

MAY, J.-N., MOSS, J. I., MUELLER, F., GOLOMBEK, S. K., BIANCACCI, I., RIZZO, L., ELSHAFEI, A. S., GREMSE, F., POLA, R., PECHAR, M., ETRYCH, T., BECKER, S., TRAUTWEIN, C., BÜLOW, R. D., BOOR, P., KNUECHEL, R., VON STILLFRIED, S., STORM, G., PURI, S., BARRY, S. T., SCHULZ, V., KIESSLING, F., ASHFORD, M. B. & LAMMERS, T. 2024. Histopathological biomarkers for predicting the tumour accumulation of nanomedicines. *Nature Biomedical Engineering***,** 1-13.

MCNEIL, S. E. 2016. Evaluation of nanomedicines: stick to the basics. *Nature reviews materials,* 1**,** 1-2.

MIEDEMA, I. H., ZWEZERIJNEN, G. J., HUISMAN, M. C., DOELEMAN, E., MATHIJSSEN, R. H., LAMMERS, T., HU, Q., VAN DONGEN, G. A., RIJCKEN, C. J. & VUGTS, D. J. 2022. PET-CT Imaging of Polymeric Nanoparticle Tumor Accumulation in Patients. *Advanced Materials,* 34**,** 2201043.

MIHYAR, R., SHALMANI, A. A., WILDT, V., SHEYBANIFARD, M., WANG, A., MAY, J.-N., SHAHZAD, S., BUHL, E. M., RÜTTEN, S. & BEHRENS, D. 2024. Microfluidic formulation, cryoprotection and long-term stability of paclitaxel-loaded π electron-stabilized polymeric micelles. *Journal of Controlled Release,* 375**,** 614-626.

MILLER, K., CORTES, J., HURVITZ, S. A., KROP, I. E., TRIPATHY, D., VERMA, S., RIAHI, K., REYNOLDS, J. G., WICKHAM, T. J. & MOLNAR, I. 2016. HERMIONE: a randomized Phase 2 trial of MM-302 plus trastuzumab versus chemotherapy of physician's choice plus trastuzumab in patients with previously treated, anthracycline-naïve, HER2-positive, locally advanced/metastatic breast cancer. *BMC cancer,* 16**,** 1-11.

MILLER, M. A., CHANDRA, R., CUCCARESE, M. F., PFIRSCHKE, C., ENGBLOM, C., STAPLETON, S., ADHIKARY, U., KOHLER, R. H., MOHAN, J. F. & PITTET, M. J. 2017.

Radiation therapy primes tumors for nanotherapeutic delivery via macrophage-mediated vascular bursts. *Science translational medicine,* 9**,** eaal0225.

MILLER, M. A., GADDE, S., PFIRSCHKE, C., ENGBLOM, C., SPRACHMAN, M. M., KOHLER, R. H., YANG, K. S., LAUGHNEY, A. M., WOJTKIEWICZ, G. & KAMALY, N. 2015a. Predicting therapeutic nanomedicine efficacy using a companion magnetic resonance imaging nanoparticle. *Science translational medicine,* 7**,** 314ra183-314ra183.

MILLER, M. A., ZHENG, Y.-R., GADDE, S., PFIRSCHKE, C., ZOPE, H., ENGBLOM, C., KOHLER, R. H., IWAMOTO, Y., YANG, K. S. & ASKEVOLD, B. 2015b. Tumour-associated macrophages act as a slow-release reservoir of nano-therapeutic Pt (IV) pro-drug. *Nature communications,* 6**,** 8692.

MONJE, M., MAHDI, J., MAJZNER, R., YEOM, K. W., SCHULTZ, L. M., RICHARDS, R. M., BARSAN, V., SONG, K.-W., KAMENS, J. & BAGGOTT, C. 2024. Intravenous and intracranial GD2-CAR T cells for H3K27M+ diffuse midline gliomas. *Nature***,** 1-8.

MORTIMER, J. E., BADING, J. R., FRANKEL, P. H., CARROLL, M. I., YUAN, Y., PARK, J. M., TUMYAN, L., GIDWANEY, N., POKU, E. K. & SHIVELY, J. E. 2022. Use of 64Cu-DOTA-trastuzumab PET to predict response and outcome of patients receiving trastuzumab emtansine for metastatic breast cancer: a pilot study. *Journal of Nuclear Medicine,* 63**,** 1145-1148.

MOSS, J. I., BARJAT, H., EMMAS, S.-A., STRITTMATTER, N., MAYNARD, J., GOODWIN, R. J., STORM, G., LAMMERS, T., PURI, S. & ASHFORD, M. B. 2020. High-resolution 3D visualization of nanomedicine distribution in tumors. *Theranostics,* 10**,** 880.

NGAI, J., MACMILLAN, P., KINGSTON, B. R., LIN, Z. P., OUYANG, B. & CHAN, W. C. 2023. Delineating the tumour microenvironment response to a lipid nanoparticle formulation. *Journal of Controlled Release,* 353**,** 988-1001.

NGUYEN, L. N., LIN, Z. P., SINDHWANI, S., MACMILLAN, P., MLADJENOVIC, S. M., STORDY, B., NGO, W. & CHAN, W. C. 2023. The exit of nanoparticles from solid tumours. *Nature Materials,* 22**,** 1261-1272.

NICHOLS, J. W. & BAE, Y. H. 2014. EPR: Evidence and fallacy. *Journal of Controlled Release,* 190**,** 451-464.

O'BRIEN, M. E., WIGLER, N., INBAR, M., ROSSO, R., GRISCHKE, E., SANTORO, A., CATANE, R., KIEBACK, D., TOMCZAK, P. & ACKLAND, S. 2004. Reduced cardiotoxicity and comparable efficacy in a phase IIItrial of pegylated liposomal doxorubicin HCl (CAELYX™/Doxil®) versus conventional doxorubicin forfirst-line treatment of metastatic breast cancer. *Annals of oncology,* 15**,** 440-449.

OUYANG, B., POON, W., ZHANG, Y.-N., LIN, Z. P., KINGSTON, B. R., TAVARES, A. J., ZHANG, Y., CHEN, J., VALIC, M. S. & SYED, A. M. 2020. The dose threshold for nanoparticle tumour delivery. *Nature materials,* 19**,** 1362-1371.

OWENS III, D. E. & PEPPAS, N. A. 2006. Opsonization, biodistribution, and pharmacokinetics of polymeric nanoparticles. *International journal of pharmaceutics,* 307**,** 93-102.

PADERA, T. P., STOLL, B. R., TOOREDMAN, J. B., CAPEN, D., TOMASO, E. D. & JAIN, R. K. 2004. Cancer cells compress intratumour vessels. *Nature,* 427**,** 695-695.

PARDRIDGE, W. M. 2007. Blood–brain barrier delivery. *Drug discovery today,* 12**,** 54-61.

PARDRIDGE, W. M. 2012. Drug transport across the blood–brain barrier. *Journal of cerebral blood flow & metabolism,* 32**,** 1959-1972.

PEER, D., KARP, J. M., HONG, S., FAROKHZAD, O. C., MARGALIT, R. & LANGER, R. 2007. Nanocarriers as an emerging platform for cancer therapy. *Nature Nanotechnology,* 2**,** 751-760.

PENTZ, R. D., FLAMM, A. L., PASQUALINI, R., LOGOTHETIS, C. J. & ARAP, W. 2003. Revisiting ethical guidelines for research with terminal wean and brain-dead participants. *Hastings Center Report,* 33**,** 20-26.

PÉREZ-MEDINA, C., ABDEL-ATTI, D., TANG, J., ZHAO, Y., FAYAD, Z. A., LEWIS, J. S., MULDER, W. J. & REINER, T. 2016. Nanoreporter PET predicts the efficacy of anti-cancer nanotherapy. *Nature communications,* 7**,** 11838.

PORRETT, P. M., ORANDI, B. J., KUMAR, V., HOUP, J., ANDERSON, D., COZETTE KILLIAN, A., HAUPTFELD-DOLEJSEK, V., MARTIN, D. E., MACEDON, S. & BUDD, N. 2022. First clinical-grade porcine kidney xenotransplant using a human decedent model. *American Journal of Transplantation,* 22**,** 1037-1053.

PRICE, L. S., STERN, S. T., DEAL, A. M., KABANOV, A. V. & ZAMBONI, W. C. 2020. A reanalysis of nanoparticle tumor delivery using classical pharmacokinetic metrics. *Science advances,* 6**,** eaay9249.

RAMANATHAN, R. K., KORN, R. L., RAGHUNAND, N., SACHDEV, J. C., NEWBOLD, R. G., JAMESON, G., FETTERLY, G. J., PREY, J., KLINZ, S. G. & KIM, J. 2017. Correlation between ferumoxytol uptake in tumor lesions by MRI and response to nanoliposomal irinotecan in patients with advanced solid tumors: a pilot study. *Clinical Cancer Research,* 23**,** 3638-3648.

REZAI, A. R., RANJAN, M., HAUT, M. W., CARPENTER, J., D'HAESE, P.-F., MEHTA, R. I., NAJIB, U., WANG, P., CLAASSEN, D. O. & CHAZEN, J. L. 2022. Focused ultrasound–mediated blood-brain barrier opening in Alzheimer's disease: long-term safety, imaging, and cognitive outcomes. *Journal of Neurosurgery,* 139**,** 275-283.

RIHOVA, B., JELINKOVA, M., STROHALM, J., SUBR, V., PLOCOVA, D., HOVORKA, O., NOVAK, M., PLUNDROVA, D., GERMANO, Y. & ULBRICH, K. 2000. Polymeric drugs based on conjugates of synthetic and natural macromolecules. II. Anti-cancer activity of antibody or (Fab')(2)-targeted conjugates and combined therapy with immunomodulators. *J Control Release,* 64**,** 241-61.

RIX, A., PIEPENBROCK, M., FLEGE, B., VON STILLFRIED, S., KOCZERA, P., OPACIC, T., SIMONS, N., BOOR, P., THORÖE-BOVELETH, S. & DECKERS, R. 2021. Effects of contrast-enhanced ultrasound treatment on neoadjuvant chemotherapy in breast cancer. *Theranostics,* 11**,** 9557.

ROJAS, L. A., SETHNA, Z., SOARES, K. C., OLCESE, C., PANG, N., PATTERSON, E., LIHM, J., CEGLIA, N., GUASP, P. & CHU, A. 2023. Personalized RNA neoantigen vaccines stimulate T cells in pancreatic cancer. *Nature,* 618**,** 144-150.

ROOVERS, S., SEGERS, T., LAJOINIE, G., DEPREZ, J., VERSLUIS, M., DE SMEDT, S. C. & LENTACKER, I. 2019. The role of ultrasound-driven microbubble dynamics in drug delivery: from microbubble fundamentals to clinical translation. *Langmuir,* 35**,** 10173-10191.

SAFRA, T., MUGGIA, F., JEFFERS, S., TSAO-WEI, D., GROSHEN, S., LYASS, O., HENDERSON, R., BERRY, G. & GABIZON, A. 2000. Pegylated liposomal doxorubicin (doxil): reduced clinical cardiotoxicity in patients reaching or exceeding cumulative doses of 500 mg/m2. *Annals of Oncology,* 11**,** 1029-1034.

SCHINDELIN, J., ARGANDA-CARRERAS, I., FRISE, E., KAYNIG, V., LONGAIR, M., PIETZSCH, T., PREIBISCH, S., RUEDEN, C., SAALFELD, S. & SCHMID, B. 2012. Fiji: an open-source platform for biological-image analysis. *Nature methods,* 9**,** 676-682.

SHEIKOV, N., MCDANNOLD, N., VYKHODTSEVA, N., JOLESZ, F. & HYNYNEN, K. 2004. Cellular mechanisms of the blood-brain barrier opening induced by ultrasound in presence of microbubbles. *Ultrasound in medicine & biology,* 30**,** 979-989.

SHI, J., KANTOFF, P. W., WOOSTER, R. & FAROKHZAD, O. C. 2017. Cancer nanomedicine: progress, challenges and opportunities. *Nature reviews cancer,* 17**,** 20-37.

SINDHWANI, S., SYED, A. M., NGAI, J., KINGSTON, B. R., MAIORINO, L., ROTHSCHILD, J., MACMILLAN, P., ZHANG, Y., RAJESH, N. U. & HOANG, T. 2020. The entry of nanoparticles into solid tumours. *Nature materials,* 19**,** 566-575.

SLAMON, D., EIERMANN, W., ROBERT, N., PIENKOWSKI, T., MARTIN, M., PRESS, M., MACKEY, J., GLASPY, J., CHAN, A. & PAWLICKI, M. 2011. Adjuvant trastuzumab in HER2-positive breast cancer. *New England journal of medicine,* 365**,** 1273-1283.

SNIPSTAD, S., SULHEIM, E., DE LANGE DAVIES, C., MOONEN, C., STORM, G., KIESSLING, F., SCHMID, R. & LAMMERS, T. 2018. Sonopermeation to improve drug delivery to tumors: from fundamental understanding to clinical translation. *Expert opinion on drug delivery,* 15**,** 1249-1261.

SNIPSTAD, S., VIKEDAL, K., MAARDALEN, M., KURBATSKAYA, A., SULHEIM, E. & DE LANGE DAVIES, C. 2021. Ultrasound and microbubbles to beat barriers in tumors:

Improving delivery of nanomedicine. *Advanced Drug Delivery Reviews,* 177**,** 113847.

STRITTMATTER, N., MOSS, J. I., RACE, A. M., SUTTON, D., CANALES, J. R., LING, S., WONG, E., WILSON, J., SMITH, A. & HOWES, C. 2022. Multi-modal molecular imaging maps the correlation between tumor microenvironments and nanomedicine distribution. *Theranostics,* 12**,** 2162.

SULHEIM, E., KIM, J., VAN WAMEL, A., KIM, E., SNIPSTAD, S., VIDIC, I., GRIMSTAD, I. H., WIDERØE, M., TORP, S. H. & LUNDGREN, S. 2018. Multi-modal characterization of vasculature and nanoparticle accumulation in five tumor xenograft models. *Journal of controlled release,* 279**,** 292-305.

TANG, Y., LIU, B., ZHANG, Y., LIU, Y., HUANG, Y. & FAN, W. 2024. Interactions between nanoparticles and lymphatic systems: Mechanisms and applications in drug delivery. *Advanced Drug Delivery Reviews***,** 115304.

THEEK, B., BAUES, M., GREMSE, F., POLA, R., PECHAR, M., NEGWER, I., KOYNOV, K., WEBER, B., BARZ, M. & JAHNEN-DECHENT, W. 2018. Histidine-rich glycoprotein-induced vascular normalization improves EPR-mediated drug targeting to and into tumors. *Journal of controlled release,* 282**,** 25-34.

THEEK, B., BAUES, M., OJHA, T., MOCKEL, D., VEETTIL, S. K., STEITZ, J., VAN BLOOIS, L., STORM, G., KIESSLING, F. & LAMMERS, T. 2016. Sonoporation enhances liposome accumulation and penetration in tumors with low EPR. *J Control Release,* 231**,** 77-85.

THEEK, B., GREMSE, F., KUNJACHAN, S., FOKONG, S., POLA, R., PECHAR, M., DECKERS, R., STORM, G., EHLING, J. & KIESSLING, F. 2014. Characterizing EPR-mediated passive drug targeting using contrast-enhanced functional ultrasound imaging. *Journal of controlled release,* 182**,** 83-89.

TONG, R. T., BOUCHER, Y., KOZIN, S. V., WINKLER, F., HICKLIN, D. J. & JAIN, R. K. 2004. Vascular normalization by vascular endothelial growth factor receptor 2 blockade induces a pressure gradient across the vasculature and improves drug penetration in tumors. *Cancer research,* 64**,** 3731-3736.

TSVETKOVA, Y., BEZTSINNA, N., BAUES, M., KLEIN, D., RIX, A., GOLOMBEK, S. K., AL RAWASHDEH, W. E., GREMSE, F., BARZ, M. & KOYNOV, K. 2017. Balancing passive and active targeting to different tumor compartments using riboflavin-functionalized polymeric nanocarriers. *Nano letters,* 17**,** 4665-4674.

VAN DER MEEL, R., SULHEIM, E., SHI, Y., KIESSLING, F., MULDER, W. J. & LAMMERS, T. 2019. Smart cancer nanomedicine. *Nature nanotechnology,* 14**,** 1007-1017.

VENDITTO, V. J. & SZOKA JR, F. C. 2013. Cancer nanomedicines: so many papers and so few drugs! *Advanced drug delivery reviews,* 65**,** 80-88.

VITANZA, N. A., RONSLEY, R., CHOE, M., SEIDEL, K., HUANG, W., RAWLINGS-RHEA, S. D., BEAM, M., STEINMETZER, L., WILSON, A. L. & BROWN, C. 2025. Intracerebroventricular B7-H3-targeting CAR T cells for diffuse intrinsic pontine glioma: a phase 1 trial. *Nature Medicine***,** 1-8.

VON HOFF, D. D., MITA, M. M., RAMANATHAN, R. K., WEISS, G. J., MITA, A. C., LORUSSO, P. M., BURRIS III, H. A., HART, L. L., LOW, S. C. & PARSONS, D. M. 2016. Phase I study of PSMA-targeted docetaxel-containing nanoparticle BIND-014 in patients with advanced solid tumors. *Clinical Cancer Research,* 22**,** 3157-3163.

VYKHODTSEVA, N., HYNYNEN, K. & DAMIANOU, C. 1995. Histologic effects of high intensity pulsed ultrasound exposure with subharmonic emission in rabbit brain in vivo. *Ultrasound in medicine & biology,* 21**,** 969-979.

WALL, M. E. & WANI, M. C. 1995. Camptothecin and taxol: discovery to clinic—thirteenth Bruce F. Cain Memorial Award Lecture. *Cancer research,* 55**,** 753-760.

WEBER, J. S., CARLINO, M. S., KHATTAK, A., MENIAWY, T., ANSSTAS, G., TAYLOR, M. H., KIM, K. B., MCKEAN, M., LONG, G. V. & SULLIVAN, R. J. 2024. Individualised neoantigen therapy mRNA-4157 (V940) plus pembrolizumab versus pembrolizumab monotherapy in resected melanoma (KEYNOTE-942): a randomised, phase 2b study. *The Lancet,* 403**,** 632-644.

WILHELM, S., TAVARES, A. J. & CHAN, W. C. 2016a. Reply to "Evaluation of nanomedicines: stick to the basics". *Nature Reviews Materials,* 1**,** 1-2.

WILHELM, S., TAVARES, A. J., DAI, Q., OHTA, S., AUDET, J., DVORAK, H. F. & CHAN, W. C. 2016b. Analysis of nanoparticle delivery to tumours. *Nature reviews materials,* 1**,** 1-12.

WILLIAMS, K. 2009. The introduction of 'chemotherapy'using arsphenamine–the first magic bullet. *Journal of the Royal Society of Medicine,* 102**,** 343-348.

YOKOI, K., KOJIC, M., MILOSEVIC, M., TANEI, T., FERRARI, M. & ZIEMYS, A. 2014a. Capillary-wall collagen as a biophysical marker of nanotherapeutic permeability into the tumor microenvironment. *Cancer research,* 74**,** 4239-4246.

YOKOI, K., TANEI, T., GODIN, B., VAN DE VEN, A. L., HANIBUCHI, M., MATSUNOKI, A., ALEXANDER, J. & FERRARI, M. 2014b. Serum biomarkers for personalization of nanotherapeutics-based therapy in different tumor and organ microenvironments. *Cancer Letters,* 345**,** 48-55.

9 Appendix

List of own publications

Jan-Niklas May*, Susanne K. Golombek*, Maike Baues, Anshuman Dasgupta, Natascha Drude, Anne Rix, Dirk Rommel, Saskia von Stillfried, Lia Appold, Robert Pola, Michal Pechar, Louis van Bloois, Gert Storm, Alexander Kuehne, Felix Gremse, Benjamin Theek, Fabian Kiessling, Twan Lammers; Multimodal and multiscale optical imaging of nanomedicine delivery across the blood-brain barrier upon sonopermeation; **Theranostics**; 2020; 10(4); 1948-1959; *** shared first authors**

Jan-Niklas May*, Jennifer I. Moss*, Florian Mueller, Susanne K. Golombek, Ilaria Biancacci, Larissa Rizzo, Asmaa Said Elshafei, Felix Gremse, Robert Pola, Michal Pechar, Tomas Etrych, Svea Becker, Christian Trautwein, Roman D. Bülow, Peter Boor, Ruth Knuechel, Saskia von Stillfried, Gert Storm, Sanyogitta Puri, Simon T. Barry, Volkmar Schulz, Fabian Kiessling, Marianne B. Ashford, Twan Lammers; Histopathological biomarkers for predicting the tumour accumulation of nanomedicines; **Nature Biomedical Engineering;** 2024; 8; 1366-1378; *** shared first authors**

Additional publications:

Susanne K. Golombek, **Jan-Niklas May**, Benjamin Theek, Lia Appold, Natascha Drude, Fabian Kiessling, Twan Lammers; Tumor targeting via EPR: Strategies to enhance patient responses; **Advanced Drug Delivery Reviews**; 2018; 130; 17-38

Jasmin Baier, Anne Rix, Natascha Drude, Milita Darguzyte, Maike Baues, **Jan-Niklas May**, Sandra Schipper, Diana Möckel, Rupert Palme, René Tolba, Fabian Kiessling; Influence of MRI Examinations on Animal Welfare and Study Results; **Investigative Radiology**; 2020; 55(8); 507-514

Anne Rix, Marion Piepenbrock, Barbara Flege, Saskia von Stillfried, Patrick Koczera, Tatjana Opacic, Nina Simons, Peter Boor, Sven Thoröe-Boveleth, Roel Deckers, **Jan-Niklas May**, Twan Lammers, Georg Schmitz, Elmar Stickeler, Fabian Kiessling; Effects of

contrast-enhanced ultrasound treatment on neoadjuvant chemotherapy in breast cancer; **Theranostics**; 2021; 11(19); 9557-9570

Ilaria Biancacci, Federica De Lorenzi, Benjamin Theek, Xiangyang Bai, **Jan-Niklas May**, Lorena Consolino, Maike Baues, Diana Moeckel, Felix Gremse, Saskia von Stillfried, Asmaa El Shafei, Karina Benderski, Armin Azadkhah Shalmani, Alec Wang, Jeffrey Momoh, Quim Peña, Eva Miriam Buhl, Johannes Buyel, Wim Hennink, Fabian Kiessling, Josbert Metselaar, Yang Shi, Twan Lammers; Monitoring EPR Effect Dynamics during Nanotaxane Treatment with Theranostic Polymeric Micelles; **Advanced Science**; 2022; 9(10); 2103745

Jasmin Baier, Anne Rix, Milita Darguzyte, Renée Michèle Girbig, **Jan-Niklas May**, Rupert Palme, René Tolba, Fabian Kiessling; Repeated contrast-enhanced micro-CT examinations decrease animal welfare and influence tumor physiology; **Investigative Radiology**; 2022; 58(5); 327-336

Elisa F. Brandt, Maike Baues, Theresa H. Wirtz, **Jan-Niklas May**, Petra Fischer, Anika Beckers, Björn-Carsten Schüre, Hacer Sahin, Christian Trautwein, Twan Lammers, Marie-Luise Berres; Chemokine CXCL10 Modulates the Tumor Microenvironment of Fibrosis-Associated Hepatocellular Carcinoma; **International Journal of Molecular Sciences**; 2022; 23(15); 8112

Svea Becker, Jeffrey Momoh, Ilaria Biancacci, Diana Möckel, Qingbi Wang, **Jan-Niklas May**, Huan Su, Lena Susanne Candels, Marie-Luise Berres, Fabian Kiessling, Maximilian Hatting, Twan Lammers, Christian Trautwein; Intermittent Fasting Primes the Tumor Microenvironment And Improves Nanomedicine Delivery In Hepatocellular Carcinoma; **Small;** 2023; 19(43); 2208042

Sonia Vicente-Ruiz, Ana Arminan, Katia Maso, Elena Gallon, Oleksandr Zagorodko, Julie Movellan, Fernanda Rodriguez-Otormin, Maike Baues, **Jan-Niklas May**, Federica De Lorenzi, Twan Lammers, María Vicent; Poly-L-Glutamic acid modification modulates the bio-nano interface of a therapeutic anti-IGF-1R antibody in prostate cancer; **Biomaterials;** 2023; 301; 122280

Christopher Hark, Junlin Chen, Julia Blöck, Eva Miriam Buhl, Harald Radermacher, Robert Pola, Michal Pechar, Tomáš Etrych, Quim Peña, Anne Rix, Natascha Ingrid Drude, Fabian Kiessling, Twan Lammers[#], **Jan-Niklas May[#]**; RGD-coated polymeric microbubbles promote ultrasound-mediated drug delivery in an inflamed endothelium-pericyte co-culture model of the blood-brain barrier; **Drug Delivery and Translational Research;** 2024; 14; 2629-2641; **[#] corresponding authors**

Rahaf Mihyar, Armin Azadkhah Shalmani, Viktor Wildt, Maryam Sheybanifard, Alec Wang, **Jan-Niklas May**, Saba Shahzad, Eva Miriam Buhl, Stephan Rütten, Diana Behrens, Wolfgang Walther, Mattia Tiboni, Luca Casettari, Johannes F. Buyel, Cristianne J.F. Rijcken, Wim E. Hennink, Saskia von Stillfried, Fabian Kiessling, Yang Shi, Josbert M. Metselaar, Twan Lammers, Quim Peña; Microfluidic formulation, cryoprotection and long-term stability of paclitaxel-loaded π electron-stabilized polymeric micelles; **Journal of Controlled Release;** 2024; 375; 614-626

Anshuman Dasgupta, **Jan-Niklas May**, Geir Klinkenberg, Helena C. Besse, Eva Miriam Buhl, Diana Möckel, Rahaf Mihyar, Quim Peña, Armin Azadkhah Shalmani, Christopher Hark, Anne Rix, Susanne Koletnik, Josbert Metselaar, Yang Shi, Wim E. Hennink, Gert Storm, Dannis van Vuurden, Chrit Moonen, Mario Ries, Ruth Schmid, Fabian Kiessling, Twan Lammers; Multidrug Micelles and Sonopermeation for Chemotherapy Co-Delivery to Brain Tumors; **Journal of Controlled Release;** 2025; 380; 818-828

Natascha Drude, Camila Baselly, Malgorzata Anna Gazda, **Jan-Niklas May**, Lena Tienken, Parya Abbasi, Tracey Weissgerber, Steven Burgess; Reporting quality of quantitative polymerase chain reaction (qPCR) methods in scientific publications; submitted

10 Acknowledgement

Completing this doctoral dissertation has been a challenging yet rewarding journey, and I am deeply grateful to those who have travelled some parts or even the whole way with me.

First and foremost, I am deeply thankful to my supervisor Twan Lammers for the opportunity to work at ExMI. I appreciate your honest feedback, usually served with a smirk, barely discouraging and never praising someone to the skies. For your very own mix of flexibility and stubbornness. Over the years, you have given me countless opportunities to learn and grow, by connecting me to so many interesting scientists, by making your network accessible, by allowing to attend numerous conferences and meetings. Thank you for the trust and for putting me in charge of projects, that are close to your heart, and of way more tasks than the average PhD. And thank you for the ":o)" smiley, "that's a stupid answer", forwarding a mail with nothing more than the biceps emoji, and your heterogeneous mix of stubbornness and flexibility. I joined your group as a young intern during my Master and leave as a grown-up man, highly appreciating your contribution to that development.

The committee for the evaluation of this thesis would not have complete able without the second examiner, Jochen Maurer, and the chair, Willi Jahnen-Dechent. Thank you for your time and your interest in my research, and for immediately accepting to join the committee. Furthermore, I highly appreciate Jochen's patience to discuss and prepare the next amendment, your approachability as well as the cooperation within the picelles project. Having Willi Jahnen-Dechent on board is a personal honor, as he joined me on my first steps in Aachen during the first week of my Bachelor's program as well as on my last steps as a chair of the thesis committee – I guess no one could have predicted that during our first meeting.

Next, I have to - but even more want to - thank Fabian Kiessling who provided way more than just a foundation for this thesis. I really enjoyed the time at ExMI, ranging from the packed labs and offices in our beloved, green-carpeted health factory to the transition into the CBMS - it was fascinating to see the institute growing and growing. Thank you for inviting me to join the Climbing Crohn team, which broadened my knowledge and

was a valuable and insightful experience. I am still amazed by the way how successful you and Twan lead the institute, despite being partially completely contradictory. Additionally, I highly appreciate the approachability of both of you, in professional as well as private topics.

Without the contribution of Susi, Marek, Diana, Ramona, Jan, Lea and Birgit M., I would not have been able to write this thesis – as everyone else at ExMI. Thank you for taking care of daily laboratory life, for willingly sharing your knowledge and for your support in many different experiments.

Back in the days when I joined ExMI, I could not have dreamed of better supervisors than Susanne and Maike. I will forever be grateful for your introduction to ExMI, its secrets, the worlds of nanomedicine and imaging, and science in general. With the follow-up by Natascha and Anne, four superwomen ensured that work was as productive as fun (behavioral testing), wining and dining was taken care of – and thank you for Kirche, Kirsche, meschanich, Torte, and turning me into a carnivalist. All of you have been an invaluable inspiration.

With respect to personal development, I want to thank Benjamin, Einar, Patrick and Wa'el for serving as outstanding role models. Although being quite different, all of you broadened my perspectives on science, myself and my role in the world.

In general, I want to thank all colleagues at ExMI. I can barely remember someone whom I did not enjoy working with. Thank you for enriching daily work with your presence, scientific input, dumb mistakes, and the many laughs we shared. In particular, thank you, Zuza, for sharing the office the longest time, the Polish sweets, discussions about movies and music, and for always having a welcoming ear for a sticky song. Helen, for being the best health instructor, serving as a moral compass, and for making vegetarian currywurst palatable. Quim, for your dedication, our joint willingness to push the picelles project while having quite different characters, CRS Bologna, and for the introduction to the Philips app. Chris, for being the best Cape Town guide, your persistence in cultivating BBBs, and for pushing me in my role as a supervisor. Florian, for introducing me to the world of gradient tree boosting and for our stable collaboration despite external input. Ilaria, for the persistence in the AZ meetings as well

as the albumin stainings and our joint connection to Gladbeck. Harald, for your tremendous dedication in turning our focused ultrasound setup into a properly and reliably working device. Nina, for the opportunity to join Climbing Crohn, and teaching me to trust one's gut feeling. Rahaf, for scoring mice. Special thank you to Alec, Alessandro, Alex K., Alex R., Alexandros, Anshu, Armin, Björn, David, Elena, Federica, Jasmin B., Jeffrey, Julia, Junlin, Karl, Karolin, Larissa, Lia, Lisa, Lorena, Lukas, Mengjiao, Milita, Nihan, Okan, Raphael, Renée, Sandra, Sarah S., Stefan, Stephan, Tarun, Vertika, Xiangyang (and many more) for sharing an office, lab, project, or extracurricular activity with me.

Next, I want to thank all collaboration partners from Aachen, namely Alexander Kühne, Alexandru Florea, David Bülow, Dirk Rommel, Eva Miriam Buhl, Felix Gremse, Jochen Maurer, Peter Boor, Ruth Knuechel, Saskia von Stillfried, Svea Becker, Sven Thoröe-Boveleth, Thomas Hansen, Volkmar Schulz, for being easily accessible and for willingly sharing their knowledge, time, and resources. A special thank you to Katja Siegeler, Michaela Moss, René Tolba, and the animal caretakers of the VTK who jointly do an outstanding job in enabling biomedical research.

I highly appreciate the invaluable contribution from AmaZing scientists from AstraZeneca, especially Jennifer Moss, Marianne Ashford, and Simon Barry. Our extensive meetings during COVID times discussing the project, its progression, and its publication will always have a special place in my heart. As well as lovely "HOOOORAAAY!!" mails or bets at conferences. Thank you for providing an outstanding example that science can also be free, fun, and fruitful within industry.

In contrast to on-going trends in politics, several joint projects demonstrated the power of collaborative science, even across borders. In this regard, thank you to Chrit Moonen, Dannis van Vuurden, Diana Behrens, Geir Klinkenberg, Gert Storm, Heiko Manninga, Hendrik Budde, Jaleesa Bresseleers, Lisa Cattenstart, Mario Ries, Mark van Eldijk, Michal Pechar, Rob van der Weegen, Robert Pola, Ruth Schmid, Sofie Snipstad, Sven Borgos, Tomáš Etrych, Wolfgang Walther, for very different collaborations, which all had one parameter in common – they provided lots of knowledge and allowed me to learn a lot.

I want to thank Jens Beckers, Burkhard Dickhöver, Birgit van Marwick, Jasmin Dahmen, Iris Ermer, Ümüt Sarigül, Alexandra Michel, the late Olaf Klein, Anja Junker, Detlev Gerber, Gerd Kügler, Dennis Kluck, Veronika Zimmermann as representatives for all usually unsung heroes, that barely appear on publications but allow an institution to run smoothly.

One of the best decisions during my PhD was to follow Fabian's and Twan's advice to get involved with the ESMI, its child GyMIC, and to organize our very own meetings. Thank you, Doris, Annette, Irene for taking care of the best scientific society. And thank you, Maike, the MoBi in Aachen was a blast, as well as all GyMIC chairs, namely Mario, Barbara, Sophie, Emily, Daniel, Saskia – I really enjoyed working on our very own small community.

I also want to take the chance to acknowledge all patients and their families, whose tumor tissues have been investigated during this thesis. Although science might have failed you in providing a treatment in time, I hope that there will be better therapies available in the future. Furthermore, I want to remember all animals that have been killed for the sake of science and keep my fingers crossed that the on-going efforts result in more advanced in vitro models replacing animal experiments wherever possible.

To conclude the professional part of the acknowledgement, I want to appreciate all funding agencies, mainly DFG, BMBF, and ERC, and the taxpayers that enabled the here presented research by providing resources to pay materials, devices, and salary. Unfortunately, it becomes more and more apparent how valuable, advantageous, and value-adding free and independent science, that is financed by taxpayers' money, can be.

Due the time of this dissertation, I have been very lucky to find new friends among my colleagues. Even more, I could count on the support, the distraction and the mental oases of numerous friends, be it from the days back in school or the handball teams. Thank you for every moment we shared, I highly appreciate it and will always keep you in my heart.

Last but not least, I want to thank my family, including my parents, sister, grandparents, and godparents for all their efforts and investments in raising and educating me. Words

cannot express my gratitude and I will never be able to pay it back. Thank you. Furthermore, I want to thank my whole family-in-law for welcoming me with open arms. Eventually, I want to express my deepest gratitude to my wife and my daughter – you have been, are, and will always be my greatest inspiration and motivation.

This dissertation is dedicated to all of you.

11 Erklärung zur Datenaufbewahrung

Hiermit erkläre ich, Jan-Niklas May, dass die dieser Dissertation zu Grunde liegenden Originaldaten im Institut für Experimentelle Molekulare Bildgebung des Universitätsklinikums RTWH Aachen hinterlegt sind.

12 Erklärung über den Eigenanteil

Muster 4 A

Eidesstattliche Erklärung gemäß § 5 Abs. (1) und § 11 Abs. (3) 12. der Promotionsordnung

Hiermit erkläre ich, **Jan-Niklas May** an Eides statt, dass ich folgende in der von mir selbstständig erstellten Dissertation „**Optical imaging and immunohistological biomarkers to overcome obstacles in nanomedicine drug delivery to tumors and to the brain**“ dargestellten Ergebnisse erhoben habe:

Bei der Durchführung der Arbeit hatte ich folgende Hilfestellungen, die in der Danksagung angegeben sind. **Die Tabelle ist Pflicht! Die Nutzung von KI bzw. ChatGPT muss in der Erklärung zu den Eigenanteilen angegeben werden.**

	Studienkoordination	Studiendesign	Studienüberwachung	Herstellung & Analyse von Materialien	Durchführung & Analyse Tierversuche	Immunohistologische Färbungen	Mikroskopie	Gradient Tree Boosting	Analyse der immunohistochemischen Färbungen	Analyse des Biomarkerdatensatzes	Datenanalyse	Statistik
Jan-Niklas May		20			40	67	70	20	70	65	65	74
Jennifer I. Moss		15		10	20	5	2		4	10	2	5
Florian Mueller		8						70		2	2	5
Susanne K. Golombek		10			20	15	20		10	10	5	
Ilaria Biancacci					5	2			2	2	2	
Larissa Rizzo						2			2	2	2	
Asmaa Said Elshafei					5							
Felix Gremse										2	2	
Robert Pola				20								
Michal Pechar				20								
Tomáš Etrych				10								
Svea Becker		2			5	2			2			
Maike Baues							2				2	2
Anshuman Dasgupta							1					
Natascha Drude											2	
Anne Rix					5							
Dirk Rommel							5					
Lia Appold				10								
Louis van Bloois				10								
Alexander J. C Kuehne			8								2	
Benjamin Theek											2	
Christian Trautwein			2									
Roman D. Bülow						2				2	2	
Peter Boor			5						2			
Ruth Knuechel									2			
Saskia von Stillfried						5			2			
Gert Storm			5	20								
Sanyogitta Puri			5									
Simon T. Barry			10									
Volkmar Schulz			10					10				2
Fabian Kiessling			10									2
Marianne B. Ashford		15	15						2	2	5	
Twan Lammers	100	30	30						2	3	5	10
Summe (%)	100	100	100	100	100	100	100	100	100	100	100	100

_____

Unterschrift des Doktoranden Jan-Niklas May

Als Betreuer der obigen Dissertation bestätige ich die Angaben von Jan-Niklas May.

_____

Unterschrift des Doktorvaters Prof. Twan Lammers

13 Curriculum Vitae

Jan-Niklas May, MSc

Professional Summary

Conducting research for more than seven years, I gained experiences in in vitro, preclinical and clinical studies, with a clear focus on imaging and image analysis. As I am driven to have an impact in patients, working on three different projects aiming for translation of therapeutic drug delivery systems, diagnostic contrast agents, and histopathological biomarkers enriched my professional life. I enjoy working in interdisciplinary teams, to develop solutions based on the expertise of multiple different backgrounds.

Academic career

Doctoral Student, Theoretical medicine | 2017 - Present

RWTH Aachen University, Institute for Experimental Molecular Imaging, Prof. Lammers

Master of Science, Biology | 2014 - 2017

RWTH Aachen University, Institute for Experimental Molecular Imaging, Prof. Lammers

Bachelor of Science, Biology | 2011 - 2014

RWTH Aachen University, Institute for Biology I, Prof. Panstruga

Additional qualifications

FELASA B certificate (Laboratory Animal Science and Methods of Animal Experimentation, in accordance with the recommendation of the Federation of Laboratory Animal Science Associations (FELASA), RWTH Aachen University, Germany, 2017

Publications

13 publications, 1 manuscript under review, all in peer-reviewed journals

Conference contributions

- European Molecular Imaging Meeting (EMIM), Porto, poster presentation, 2024

- Controlled Release Society Local Chapter Meeting (CRS DeChAt LC Meeting), Bad Dürkheim, oral presentation, 2024
- Controlled Release Society Annual Meeting (CRS), Bologna, oral presentation, 2024
- European Molecular Imaging Meeting (EMIM), Salzburg, oral presentation, 2023
- Jahrestagung der Biomedizinischen Technik (BMT, DGBMT), Duisburg, oral presentation, 2023
- Controlled Release Society Annual Meeting (CRS), Montreal, oral presentation, 2022
- Jahrestagung der Biomedizinischen Technik (BMT, DGBMT), Hannover, oral presentation, 2021
- European Molecular Imaging Meeting (EMIM), Göttingen, oral presentation, 2021
- EuroNanoMed Meeting III (ENM III), Bratislava, poster presentation, 2019
- European Molecular Imaging Meeting (EMIM), Glasgow, oral presentation, 2019
- Controlled Release Society Annual Meeting (CRS), Valencia, poster presentation, 2019
- European Molecular Imaging Meeting (EMIM), San Sebastian, oral presentation, 2018
- European and Global Summit for Clinical Nanomedicine, Targeted Delivery and Precision Medicine (CLINAM), Basel, poster presentation, 2018
- Flanders Training Network Life Sciences (f-Tales), Ghent, oral and poster presentation, 2017
- European Molecular Imaging Meeting (EMIM), Cologne, poster presentation, 2017
- In vivo Cellular & Molecular Imaging Workshop (ICMI), Brussels, poster presentation, 2017
- Jahrestagung der Deutschen Gesellschaft für Biomaterialien (DGBM), Aachen, poster presentation, 2016

Awards

- Paper of the Month October (UK RWTH Aachen), Aachen, paper award, 2024
- Best paper of the special issue (Drug Delivery & Translational Research), 2024
- Best oral presentation award, Controlled Release Society Local Chapter Meeting (CRS DeChAt LC Meeting), Bad Dürkheim, 2024
- Poster award, In vivo Cellular & Molecular Imaging Workshop (ICMI), Brussels, 2017

Grant writing & project management

- NSC4DIPG (EuroNanoMed III grant, 5 project partners)
- PP-TNBC (BMBF grant, 7 project partners, including a tendering procedure of a 0.5 Mio € subcontract)
- Climbing Crohn (BMBF grant, 9 project partners)

Extracurricular activities

- TANDEMpeerMED program, RWTH Aachen University (mentee, career planning, coaching, and key competence development), 2019-2020
- German young Molecular Imaging Community (Chair 2018-2023, Treasurer 2017-2018)
- Journal reviewer (Journals of Controlled Release, Advanced Drug Delivery Reviews, Drug Delivery and Translational Research, Journal of Nanobiotechnology, Molecular Imaging and Biology, ACS Applied Nano Materials, Wiley Interdisciplinary Reviews: Nanomedicine and Nanobiotechnology, ACS Applied Bio Materials)
- Grant reviewer (Uniklinik RWTH Aachen, START program)

Scientific societies

- European Society for Molecular Imaging (ESMI)
- Controlled Release Society (CRS)
- German young Molecular Imaging Community (GyMIC)